Title
Programmable, High-Dynamic-Range Receiver Front-Ends Using Periodically Time-Varying Circuits

Author
Bu, Shi

Publication Date
2021

Peer reviewed|Thesis/dissertation

UNIVERSITY OF CALIFORNIA

Los Angeles

Programmable, High-Dynamic-Range Receiver Front-Ends Using Periodically Time-Varying Circuits

A dissertation submitted in partial satisfaction

of the requirements for the degree

Doctor of Philosophy in Electrical and Computer Engineering

by

Shi Bu

2021

ABSTRACT OF THE DISSERTATION

Programmable, High-Dynamic-Range Receiver Front-Ends
Using Periodically Time-Varying Circuits

by

Shi Bu
Doctor of Philosophy in Electrical and Computer Engineering
University of California, Los Angeles, 2021
Professor Sudhakar Pamarti, Chair

Due to the proliferation of frequency bands that need to be supported in wireless standards, such as LTE, GSM, 5G, etc., modern wireless transceiver designs rely on numerous off-chip SAW/BAW filters and many on-chip LC tanks, which are typically not very tunable. On the receiver end, this is because wireless signals typically possess vastly different strengths, and such large signal strength differences necessitate the receiver front-ends to be low-noise and linear, while providing sharp filtering. Hence, conventional approaches resort to passive off- and on-chip band-pass filters. Not only are these filters bulky, but they generally have fixed bandwidths and center frequencies, therefore a number of them are needed, occupying a lot of PCB and chip area to cover multiple bands. Consequently, it has been of significant interest in recent years to explore high-programmability SAW/BAW-less transceivers for emerging software-defined and cognitive radio applications. However, without the pre-filtering provided by SAW/BAW filters, such receivers face great challenges in providing sufficient performance in the aforementioned aspects simultaneously. Some recent approaches include N-path filters (NPFs), mixer-first receivers, and discrete-time (DT) charge-domain signal processing. They have demonstrated some level of programmability, while providing reasonably good performance, yet their overall performance has not reached

that of their counterparts using off-chip SAW/BAW filters and/or on-chip LC filters.

In this work, we explore the newly developed filtering-by-aliasing (FA) technique to build receiver front-ends using periodically time-varying (PTV) circuits. The FA technique essentially realizes sharp baseband analog FIR filtering. In conjunction with a mixer, the FA receivers offer one of the sharpest band-pass filters achieved with CMOS technologies to date and extremely high programmability. However, they also face a few problems, including relatively high noise, moderate linearity, sensitivity to parasitics at RF, and residual aliases that cannot be further filtered. They limit the ultimate dynamic range that FA receivers can achieve, and prevent wider adoption of FA receivers. This research looks into enabling techniques to enhance the dynamic range of FA receiver front-ends in order to make them more practical. A technique based on PTV noise cancellation was proposed to effectively lower the noise figure (NF) of the receiver, while maintaining the FA sharp filtering. Measurement results show an improvement of about 3 dB on NF, while simultaneously achieving 67-dB stopband rejection with a transition bandwidth of 4× the RF bandwidth. In conjunction with an up-front NPF, an out-of-band IIP_3 of +18 dBm and a blocker 1-dB compression point of +9 dBm have been demonstrated. Moreover, an innovative slice-based FA architecture with all switches moved inside the feedback network has been proposed for FA receivers in this work to provide support for carrier aggregation and improve linearity. The fabricated prototype in 28-nm CMOS demonstrated two-channel concurrent reception with filters that achieve 50-dB stopband rejection with a transition bandwidth of 3.2× the RF bandwidth. It has also shown +35-dBm IIP_3 and +12-dBm blocker 1-dB compression point with a supply voltage of only 0.9 V, whereas a low LO leakage of −81 dBm was also demonstrated. Further, a residual alias cancellation technique for FA receivers has been proposed and demonstrated on a dual-channel FA receiver. With measured frequency responses of the receiver, digital baseband filters are designed to cancel the residual aliases. Built in MATLAB, the proposed alias cancellation algorithm achieves about 15-dB alias suppression on measured data in addition to the analog FA filtering.

The dissertation of Shi Bu is approved.

Chih-Kong Ken Yang

Chee Wei Wong

Gregory J. Pottie

Sudhakar Pamarti, Committee Chair

University of California, Los Angeles

2021

To my family...

TABLE OF CONTENTS

1 Introduction **1**

1.1 Background and Motivation 1

1.2 Prior Art 4

1.2.1 Mixer-First Receivers 5

1.2.2 Discrete-Time Receivers 5

1.2.3 Filtering-by-Aliasing Receivers 7

1.2.4 Receivers for Carrier Aggregation 10

1.3 Dissertation Outline 11

2 Periodically Time-Varying Noise Cancellation for Filtering-by-Aliasing Receiver Front-Ends **13**

2.1 Introduction 13

2.2 Noise Cancellation for FA Receiver Front-Ends 17

2.2.1 LTI-NC in FA-Based Receivers 17

2.2.2 Proposed PTV Noise Cancellation 19

2.2.3 Achievable Noise Cancellation 19

2.3 Dynamic Range and Linearity Enhancement 24

2.3.1 Time-Interleaved FA 24

2.3.2 Upfront N-Path Pre-Filtering 25

2.3.3 Upfront NPF plus TI-FA 30

2.3.4 Simplified NF Analysis for the Overall Front-End 30

2.4 Circuit Implementation 32

2.5 Measurement Results 35

3 A Dual-Channel High-Linearity Filtering-by-Aliasing Receiver Front-End Supporting Carrier Aggregation . . . 42

3.1 Introduction . . . 42

3.2 Limitations of Prior FA Receivers . . . 43

3.2.1 FA Receiver in the Presence of RF-Node Reactance . . . 43

3.2.2 Problems with Multi-Channel Operation . . . 45

3.2.3 Linearity Issues . . . 45

3.2.4 Residual Aliases . . . 46

3.2.5 Noise . . . 47

3.3 Slice-Based FA Architecture . . . 47

3.3.1 PTV Operation and Input Impedance . . . 48

3.3.2 Baseband Filter Noise Performance . . . 53

3.3.3 Linearity Improvement . . . 54

3.3.4 LO Leakage Suppression . . . 59

3.4 Dual-Channel Slice-Based FA Receiver . . . 60

3.5 Circuit Implementation . . . 64

3.5.1 Low-Noise Mode . . . 66

3.6 Measurement Results . . . 67

4 Alias Cancellation for Filter-by-Aliasing Receivers . . . 77

4.1 Introduction . . . 77

4.2 Residual Alias Problem of FA Receivers . . . 78

4.3 DSP-Based Alias Cancellation . . . 80

4.3.1 Concept of the Proposed Alias Cancellation Technique . . . 80

4.3.2 Frequency Response Measurement . . . 83

4.3.3 Generation of the Digital Baseband Filters 85
4.4 Results and Discussions 88
4.4.1 Alias Cancellation for All Channels 94
4.4.2 Known Limitations 97

5 Conclusion **98**

A Generalized Noise Analysis for Baseband FA Filters **101**

References **105**

LIST OF FIGURES

1.1 The software radio architecture. 2

1.2 The SAW/BAW-less software-defined radio receiver (omitting LO frequency synthesizers). 3

1.3 Examples of carrier aggregation scenarios (a) intra-band CA and (b) inter-band CA. 4

1.4 Mixer-first receiver architecture. 6

1.5 DT receiver architecture. 6

1.6 FA receiver architecture. 8

1.7 Examples of (a) measured FA receiver filter shape and (b) measured FA receiver output spectrum with a -55-dBm in-band sinusoid at 347.5 MHz and a -5-dBm wideband blocker at 272.5 MHz simultaneously sent to the receiver input ($f_{\mathrm{LO}} =$ 350 MHz, $f_{\mathrm{s}} = 10$ MHz). 9

1.8 Prior art of intra-band carrier aggregation receivers using (a) baseband image rejection and (b) complex current sinks. 11

1.9 Inter-band carrier aggregation receiver. 12

2.1 (a) FA receiver using a PTV resistor for sharp filtering, (b) noise cancellation for mixer-first receiver using an LTI G_{m} cell at RF, and (c) proposed PTV noise cancellation for FA receiver to achieve both sharp filtering and low noise. 14

2.2 (a) Example of $R(t)$ variation and the corresponding normalized baseband filter and (b) zoom-in view showing the filter droop in the passband. 16

2.3 (a) Block diagram of naïve application of LTI-NC to an FA-based receiver, (b) simplified model illustrating perfect NC, and (c) equivalent model for illustration of the destruction of sharp filtering. 18

2.4 (a) Equivalent model of the proposed PTV-NC in an FA receiver, (b) simplified model for noise, and (c) simplified model for signal. 20

2.5 (a) Noise factor with the PTV-NC for different gain ratio, $\lambda = k_1/k_2$, in three different filter configurations, and (b) the corresponding baseband filter frequency responses with $T_s = 200$ ns. Filter 1: transition BW = 1× RF BW, $S_{11} \approx -10$ dB; filter 2: transition BW = 2× RF BW, $S_{11} \approx -20$ dB; filter 3: transition BW = 2× RF BW, $S_{11} \approx -10$ dB (i.e., same as Fig. 2.2). 22

2.6 Time-interleaved FA receiver. 25

2.7 (a) An FA-based receiver with an NPF at the RF node and (b) equivalent circuit for OOB blockers. 26

2.8 Simulated voltage waveform at node V_x of the circuit in Fig. 2.7(a) for a 10-dBm OOB blocker ($\Delta f = 80$ MHz) with and without NPF. 27

2.9 Simulated frequency responses of the receiver in Fig. 2.7(a) without and with NPF at $f_{LO} = 500$ MHz [when with the NPF, $\tilde{R}(t) = R(t)$]. 27

2.10 (a) Simulated frequency response of the receiver with adjusted $\tilde{R}(t)$ values with and without NPF and (b) in-band filter shape comparison between FA without NPF and FA with both NPF and adjusted $\tilde{R}(t)$ values. 29

2.11 (a) Comparison of the calculated $\mathrm{NF}_{\mathrm{baseband}}$ with and without NC and (b) calculated $\mathrm{NF}_{\mathrm{baseband}}$, $\mathrm{NF}_{\mathrm{aliasing}}$, and calculated and simulated overall NF with $f_{LO} = 500$ MHz with both NC and NPF ($\beta = 0.54$). 31

2.12 Complete block diagram of the implemented receiver front-end. 33

2.13 Realization of (a) RDAC and (b) G_mDAC. 34

2.14 Chip micrograph. 36

2.15 (a) Measured in-band NFs with and without NC with $f_{LO} = 500$ MHz and RF bandwidth = 10 MHz (5-MHz baseband bandwidth), and (b) NF across different LO frequencies. 37

2.16 (a) Measured 10-MHz RF bandwidth filter responses, (b) filter responses with bandwidth tuned from 2.5–40 MHz, and (c) filter responses for LO frequency varied from 0.1–1 GHz. 38

2.17 (a) Measured IIP_3 and B_{1dB} with and without NPF for $f_{LO} = 500$ MHz, and (b) OOB IIP_3 at 49-MHz offset for different LO frequencies. 39

2.18 (a) Measured S_{11}, and (b) blocker NF in the presence of a CW blocker at $\Delta f =$ 30 MHz with $f_{LO} = 500$ MHz. 39

2.19 (a) Measured LO leakage power, and (b) worst-case image filter magnitude at different LO frequencies. 40

3.1 (a) Prior FA receiver front-end with a sampling period of T_s in the presence of Z_p, and (b) effect of Z_p on the attainable filter. 44

3.2 Prior FA receiver front-ends in parallel for multi-channel operation. 45

3.3 Linearity limitation of the prior implementation of FA receivers due to nonlinear switches in the signal path. 46

3.4 Proposed slice-based FA architecture, where the G_m cells are integrated with the resistor in each slice, and switches are all moved within the feedback network. . 48

3.5 Operation using the kth slice as an example when (a) the slice is ON, and (b) the slice is OFF, where $R_{in,k} = (R_{unit} + 1/G_{m,unit})/2^{k-1}$ to the first order. 49

3.6 (a) Equivalent model of the proposed slice-based FA receiver with an example of $R_{eff}(t)$ and (b) effect of Z_p on the slice-based FA filter. 51

3.7 Alternative model of the proposed slice-based FA receiver for analyzing parasitics' effect on operation frequency. 52

3.8 Equivalent circuit for noise analysis in the baseband of the receiver. 54

3.9 Equivalent models for analyzing OOB switch nonlinearity in (a) slice-based FA receiver and (b) prior FA receiver. 56

3.10 Behavioral simulation results of input-referred P_{IM3} versus P_{in} for the prior FA approach (limited by RDAC nonlinearity), proposed approach with only switch nonlinearities, and with both switch and G_{m} nonlinearities. 57

3.11 Comparison between the mixer implementations in the prior and proposed FA receivers. 58

3.12 Equivalent models for LO leakage in (a) mixer-first receivers, (b) the slice-based FA receiver, and (c) histograms of 100-run Monte Carlo simulation results of LO leakage powers for a mixer-first receiver and the proposed FA receiver at $f_{\mathrm{LO}} =$ 500 MHz. 60

3.13 Simplistic approach to realizing a two-channel receiver using the slice-based DACs by paralleling two single-channel DACs with scaled input resistances. 61

3.14 Two-channel implementation with shared MSB and scaled down resistances to lower NF. 62

3.15 Example of resistance variations over time for $R_{\mathrm{eff1}}(t)$, $R_{\mathrm{eff2}}(t)$, overall $R_{\mathrm{shunt}}(t)$ due to two channels, and $R_{\mathrm{in}} = R_{\mathrm{eff1}}(t)||R_{\mathrm{eff2}}(t)||R_{\mathrm{shunt}}(t)$. 63

3.16 Calculated NF for the receiver front-end and comparison with the simulated and measured results. 64

3.17 Complete block diagram of the implemented receiver front-end. 65

3.18 (a) Operation principle of the LN mode, and (b) schematic of the G_{m} cell in the MSB slice. 67

3.19 Chip micrograph. 68

3.20 (a) Measured single-channel 10-MHz RF BW filter responses in the HP mode, (b) single-channel filter 3 at $f_{\mathrm{LO}} = 170$ MHz, showing the harmonic responses, and (c) single-channel filter 3 for different LO frequencies. 69

3.21 Measured concurrently receiving filter shapes in the HP mode (a) at $f_{LO1} = 500$ MHz and $f_{LO2} = 520$ MHz, (b) at $f_{LO1} = 500$MHz and $f_{LO2} = 740$MHz, (c) at $f_{LO1} = 330$ MHz and $f_{LO2} = 850$ MHz, and (d) in the LN mode at $f_{LO1} = 500$MHz and $f_{LO2} = 740$MHz. 70

3.22 Measured sideband leakage. 71

3.23 (a) Measured IIP_3 and B_{1dB} of channel 1 at $f_{LO1} = 500$ MHz for different offset frequencies, and (b) IIP_3 of both channels at 82-MHz offset frequency for different LO frequencies, in both modes. 72

3.24 Measured demodulated constellations of the two carriers in (a) HP mode and (b) LN mode. 72

3.25 Measured two-mode (a) S_{11}, (b) LO leakage at different LO frequencies, and (c) blocker NF in the presence of a CW blocker at $\Delta f = 60$ MHz for a 10-MHz RF BW filter with $f_{LO1} = 500$ MHz. 73

3.26 Measured voltage waveform at the RF node of the receiver, $V_{RF}(t)$, when a sinusoidal signal at 380 MHz is injected to its input, in (a) HP mode and (b) LN mode. 74

4.1 Illustration of the residual alias problem faced by the baseband FA filter with an f_s of 5 MHz. 79

4.2 Illustration of the alias cancellation concept for an FA receiver. 80

4.3 System overview of the alias cancellation block in the digital baseband [$(\cdot)^*$ is the complex conjugate operator]. 81

4.4 Measured baseband spectra at $f_{LO} = 270$ MHz, $f_{aux} = 350$ MHz, and $f_s = 10$ MHz with a sinusoid at 267.75 MHz sent to the input of the receiver for (a) the main and (b) auxiliary channels. 82

4.5 Measurement setup for accurately obtaining the effective frequency responses between the two channels (ignoring PCB and on-board buffers). 84

4.6 Measured baseband $\tilde{H}(j\Omega)$ with $f_{\mathrm{LO}} = 270$ MHz, $f_{\mathrm{aux}} = 350$ MHz, and $f_{\mathrm{s}} = 10$ MHz. 87

4.7 Comparison between the measured relative frequency responses between the two channels and those of the equalizing filters (no added artificial delay for easy comparison) in terms of (a) main alias' magnitude, (b) main alias' phase, (c) image alias' magnitude, and (d) image alias' phase. 90

4.8 Measured baseband spectra at the output of the main channel with an input sinusoid at 348.5 MHz with $f_{\mathrm{LO}} = 270$ MHz, $f_{\mathrm{aux}} = 350$ MHz, and $f_{\mathrm{s}} = 10$ MHz before and after alias cancellation. 91

4.9 Measured rejection before and after cancellation using test tones. 91

4.10 Measured spectra for a wideband phase-modulated blocker before and after cancellation. 92

4.11 Comparison between the measured relative frequency responses between the two channels and those of the equalizing filters for $f_{\mathrm{aux}} = 270$ MHz and $f_{\mathrm{LO}} = 350$ MHz in terms of (a) main alias' magnitude, (b) main alias' phase, (c) image alias' magnitude, and (d) image alias' phase. 93

4.12 Measured rejection before and after cancellation using test tones for $f_{\mathrm{aux}} = 270$ MHz and $f_{\mathrm{LO}} = 350$ MHz. 94

4.13 Measured spectra for a wideband phase-modulated blocker accompanied by an in-band signal before and after cancellation. 95

4.14 Simultaneous alias cancellation between the two channels (omitting I/Q calibration). 96

A.1 Model for a general noise source $V_{\mathrm{n}}(t)$. 102

A.2 Simplified model for calculating $D_{\mathrm{n}}(t)$ for PTV-NC with TI (ignoring $G_{\mathrm{m1,2}}(t)$'s noise). 104

LIST OF TABLES

2.1 Performance Summary and Comparison with the State-of-the-Art 41

3.1 Performance Summary and Comparison with State-of-the-Art Single- and Multi-Channel Receivers and Filters 75

ACKNOWLEDGMENTS

My graduate study at UCLA is undoubtedly a lifetime fortune to me, which would be impossible without all the wonderful people I have met here.

First and foremost, I would like to express my sincerest gratitude to my advisor, Professor Sudhakar Pamarti. Not only did he take me into his research group when I knew little about circuits and, especially, signal processing, but has shown great patience teaching me a lot in these two aspects and beyond. It was him who spent countless time discussing with me, pointing out what I have been missing, emphasizing both mathematical rigor and intuition, and directing me to the right path. It is impossible for me to finish my study and work here without his continuous support and guidance. The depth and breadth of his knowledge, the sharpness of his mind, and the academic rigor of his have always surprised me and made me in awe. Over the years, I only hope that I have at least imbibed some of his qualities.

I would like to thank my committee members Professor Chih-Kong Ken Yang, Professor Chee Wei Wong, and Professor Gregory J. Pottie for their time and support throughout my work. They also gave me their invaluable comments during my qualifying exam, oral defense, and thesis review. I genuinely appreciate them. In particular, I had the privilege to participate in part of the T-MUSIC project, which Professor Yang leads. I appreciate his feedback during the team weekly meetings. He also kindly wrote quite some reference letters for me. I am very grateful for his generous help. I also had the fortune to learn from Professor Wong and his students about optical combs.

During my last year of study, I was fortunate to take up a six-month internship with the ADC team at Qualcomm Technologies, Inc. Although due to COVID-19, it was conducted remotely, I nonetheless had an extremely good experience and was able to learn a lot. I certainly owe my many thanks to Dinesh Alladi, Dr. Behnam Sedighi, Elias Dagher, Dr. Honghao Ji, Aram Akhavan, Dr. Liang Dai, Dr. David Lin, Dr. Lei Sun, and the rest of the ADC team. More specifically, I want to thank Dinesh for serving as my Qualcomm Innovation Fellowship (QIF) mentor for a year, and generously offered me his rich technical insights. It was also him who provided me with this exceptional internship opportunity with

me having little experience in ADC designs. He was instrumental during my internship and gave me a lot of feedbacks on my designs. Behnam, my internship mentor, who was not only knowledgeable but always approachable, has taught me a million things. I thank him for countless time he listened to me and gave me insights and suggestions. Elias, Honghao, and Aram attended my weekly meetings and gave me valuable inputs. I thank them all.

I also owe my appreciation to MaxLinear, Inc. Not only did they kindly provide me with chip fabrication opportunity, but granted me access to their lab to perform measurement. Especially, I would like to thank Henry Chen, Dr. Rajasekhar Pullela, Pawan Tiwari, and Dr. Sheng Ye for their help.

My work has benefited tremendously from my interactions with the past and present members of the SPACE group, namely Dr. Sameed Hameed, Jiyue Yang, Dr. Hani Esmaeelzadeh, Dr. Neha Sinha, Dr. Jeffrey Lee, Dr. Nitin Nidhi, Szu-Yao Hung, Haris Suhail, Avantika Singh, and Vinod Kurian Jacob. I am very thankful for the time I had with them. In particular, I would like to thank Sameed for initializing my first research topic and setting me on the path of investigating PTV circuits, and for many technical and non-technical suggestions. I learned a lot from him. I want to thank Jiyue for literally always lending me a hand. We have discussed many things together: technical stuff, career considerations, and so on. I cherish them all. Neha, Hani, Jeffrey, and Szu-Yao have given me a lot of suggestions as senior students when I came here. Jeffrey and Nitin also helped me with various things when I first started at Broadcom, for which I am thankful. Haris took up many of my unfinished work for the T-MUSIC and wafer-scale computing projects, Avantika gave me her test benches for part of the T-MUSIC project I worked on, and Vinod shared his code as a starting point for my project on alias cancellation. I thank them all.

During my stay at UCLA, I felt blessed to have met a number of friends and fellow students. The time we spent together was priceless. My thanks go to Dr. Mahmoud Elhebeary, Dr. Han Yan, Dr. Yan Zhang, Dr. Hamed Rahmani, Dr. Weiyu Leng, Dr. Kejian Shi, Dr. Hariprasad Chandrakumar, Dr. Xuefeng Gu, Dr. Li-Yang Chen, Dr. Jiacheng Pan, Dr. Usama Anwar, Dr. Chenggang Yan, Dr. Liangxiao Tang, Premsagar Kittur, Saptadeep Pal, Yu Zhao, Hao Liu, Jiazhang Song, Sida Li, and Steven Moran. Mahmoud and I had a

lot of discussions both at UCLA and at Qualcomm. He offered a lot of help and suggestions. Han and I worked on our QIF project and I really enjoyed my time working and chatting with him. Yan and I worked on part of a proposal together, and he helped quite a bit me during my last tapeout when I had some trouble with digital synthesis. Prem was my cubicle mate for three years, and I appreciate our chats. Saptadeep showed me his awesome research on wafer-scale computing and I was fortunate to work on designing some of the power-delivery circuits for his chips.

Finally, I thank my parents for always being encouraging and supportive, and I thank my wife, Binyao, for her love and support. Special thanks go to my late grandmother. It was her emphasis on education that led me here. She will always be missed.

VITA

2014	B.Eng. in Electronic Engineering, The Chinese University of Hong Kong, Hong Kong
2016	M.Phil. in Electronic Engineering, The Chinese University of Hong Kong, Hong Kong
2021	Teaching Assistant, Department of Electrical and Computer Engineering, University of California, Los Angeles
2016–2021	Graduate Student Researcher, Department of Electrical and Computer Engineering, University of California, Los Angeles

PUBLICATIONS

S. Bu and S. Pamarti, "A dual-channel high-linearity filtering-by-aliasing receiver front-end supporting carrier aggregation," *IEEE J. Solid-State Circuits*, in press.

S. Pal, J. Liu, I. Alam, N. Cebry, H. Suhail, S. Bu, S. S. Iyer, S. Pamarti, R. Kumar, and P. Gupta, "Designing a 2048-chiplet, 14336-core waferscale processor," in *Proc. ACM/IEEE Design Autom. Conf. (DAC)*, San Francisco, CA, Dec. 2021, pp. 1183–1188.

S. Bu and S. Pamarti, "A 0.9V dual-channel filtering-by-aliasing receiver front-end achieving +35dBm IIP_3 and <-81dBm LO leakage supporting intra- and inter-band carrier aggregation," in *IEEE Int. Solid-State Circuits Conf. (ISSCC) Dig. Tech. Papers*, San Francisco, CA, Feb. 2021, pp. 94–95.

S. Bu, S. Hameed, and S. Pamarti, "Periodically time-varying noise cancellation for filtering-by-aliasing receiver front ends," *IEEE J. Solid-State Circuits*, vol. 56, no. 3, pp. 928–939, Mar. 2021.

S. Bu, S. Hameed, and S. Pamarti, "An LPTV noise cancellation technique for a 0.9-V filtering-by-aliasing receiver front-end with >67-dB stopband rejection," in *Proc. IEEE Custom Integr. Circuits Conf. (CICC)*, Austin, TX, Apr. 2019, pp. 1–4.

CHAPTER 1

Introduction

1.1 Background and Motivation

It is no surprise that over the years, the demand for faster and faster data transmission has only become stronger, both in wireless and wireline industries. However, the wireless industry does face some obstacles that are quite unique. Even though 5G has started employing mm-wave frequencies, the sub-6-GHz spectrum remains congested. Due to the high propagation loss of mm-wave communication, in the foreseeable future, the sub-6-GHz spectrum, which has been increasingly partitioned and allocated for multiple standards [1]–[3], will continue to be highly congested. However, such highly partitioned spectrum also causes problems. Radios need to only pick up signals in the desired band/channel. Conceptually this is an easy task by employing brick-wall filters. Unfortunately, brick-wall filters are non-causal and of course do not exist. Existing commercial radios resort to cascading a number of filters, both on- and off-chip ones, to perform extensive filtering. This is because of the nature of the wireless environment, in which signals and blockers can be orders of magnitude different in terms of power. The problems of the wireless radios do not stop here: although cascading filters can help select the signals of interest, all filters possess inherent nonlinearity, especially the ones based on active devices. Modern radios typically employ off-chip SAW/BAW filters for pre-filtering and on-chip LC tanks for more selectivity at RF. Both types of filters are in general bulky and not programmable, meaning their center frequencies are usually fixed, albeit providing high linearity and good filtering. As a predictable result, in order to pick up tens of bands/channels needed for GPS/GPRS/GSM/LTE/..., tens of off- and on-chip filters, or more, are needed, consuming both PCB and silicon area. The software radio concept has

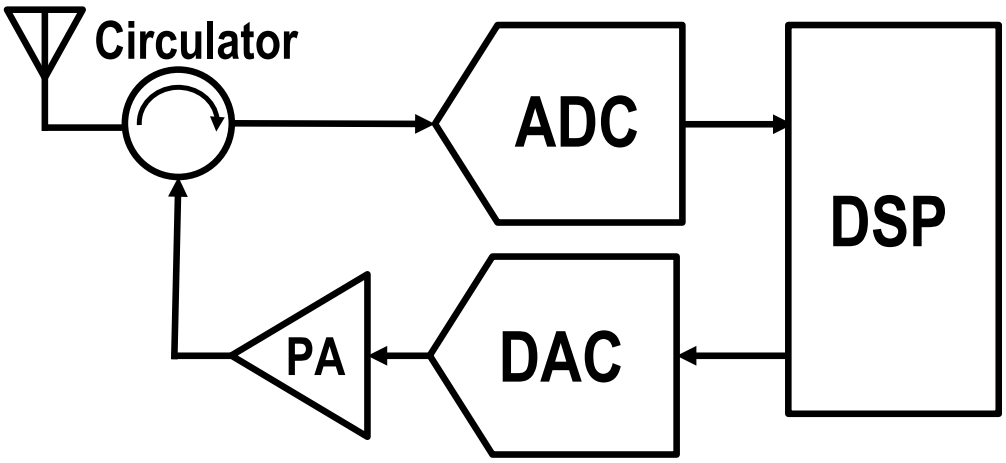

Figure 1.1: The software radio architecture.

hence emerged to overcome this problem [4], as shown in Fig. 1.1. By employing only wideband analog-to-digital converters (ADCs) and digital-to-analog converters (DACs), a single radio in principle can handle the entire transmission and reception functions of signals at arbitrary frequencies and all signal processing is performed in the digital domain.

However, this is unfortunately not realistic due to limited performance of the data converters to date. As aforementioned, unlike wireline communication, unwanted blockers at different frequencies can be orders of magnitude stronger than the desired signals, which can be similar to the thermal noise level. This demands the ADCs, using the receiver side as an example, to have extremely large dynamic range. Otherwise, it will either not be able to sense small desired signals or become saturated by large unwanted blockers. Having a large dynamic range in conjunction with a wide bandwidth means high power. In order to cover the entire sub-6-GHz spectrum (or even just 1 GHz) with a dynamic range of 100 dB, the power consumption of the ADC alone is anticipated to be more than several dozens of Watts projected from state-of-the-art ADCs' performance [5], which is impossible to be used in any commercial mobile devices. Such high power requirement prohibits this concept from being practically used, at least for commercial and civilian applications.

A more practical solution is the software-defined radio [6], where instead of relying on data converters alone, programmable front-ends are used before and after narrowband ADCs and DACs, respectively. By confining the bandwidth to a much lower number than a few

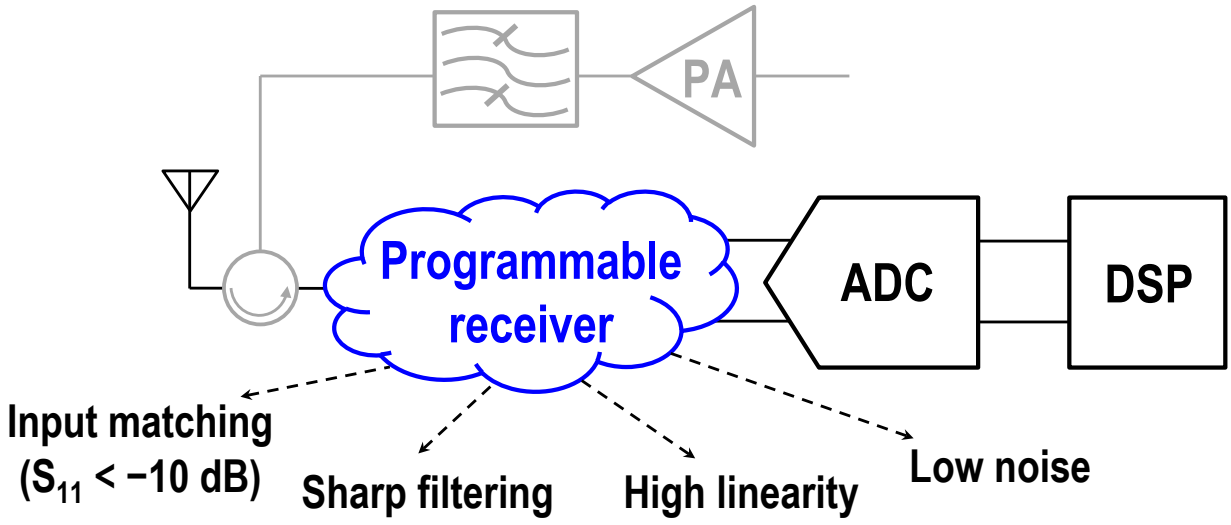

Figure 1.2: The SAW/BAW-less software-defined radio receiver (omitting LO frequency synthesizers).

GHz, the data converters' requirements can be relaxed significantly. However, now the burden falls on the shoulder of the front-ends, which need to be programmable to be able to receive or transmit desired signals across a wide spectrum. This fundamentally suggests that the front-ends cannot use most non-tunable components, such as SAW/BAW filters and LC tanks. As a results, the requirements on the front-ends are very stringent. Using the receiver as an example, shown in Fig. 1.2, it needs to simultaneously fulfill the required input impedance matching, filtering, and dynamic range. The last one can be dissected into requiring low noise from a small-signal perspective to be able to detect desired weak signals and high linearity (IIP_2, IIP_3, B_{1dB}, etc.) from a large-signal perspective to avoid distortions and saturation. The latter, in particular, is becoming more and more challenging as the supply voltage scales lower and lower in finer and finer CMOS nodes. Note that with an upfront SAW/BAW filter with a moderate 15-dB blocker rejection, the IM_3 power will be lowered by 45 dB for the same blocker power level, equivalently increasing the overall receiver chain's IIP_3 by 15 dB. Compared to this, the linearity loss in SAW/BAW-less receivers is one of the most significant costs of programmability. Additionally, in order to suppress noise, active devices, such as low-noise amplifiers (LNAs), are generally needed in receiver front-ends, which further introduce nonlinearity. This is extremely hurtful to the overall linearity

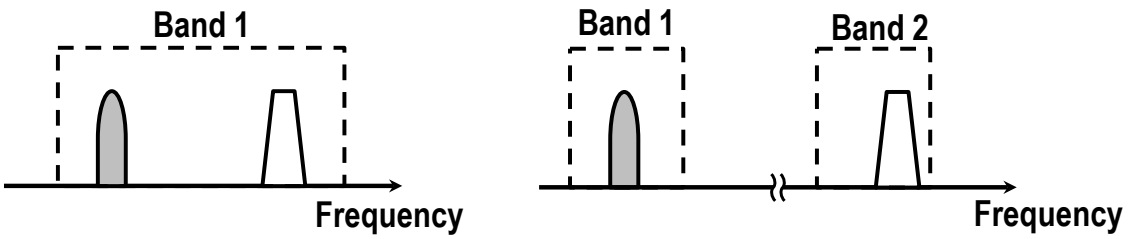

(a) (b)

Figure 1.3: Examples of carrier aggregation scenarios (a) intra-band CA and (b) inter-band CA.

in the absence of pre-filtering.

As aforementioned, the sub-6-GHz spectrum has been partitioned into multiple narrow bands, due to the scarcity of available bands. This obviously contradicts the increasing trend of data throughput, which generally translates to demanding wider bandwidth. Carrier aggregation (CA) therefore has been adopted in LTE and 5G to effectively increase the bandwidth by aggregating two or more adjacent or non-adjacent bands [7], [8]. Charming as it is, enabling CA in programmable receivers poses many other challenges. Simply speaking, in principle, a programmable CA receiver for software-defined radio applications needs to support two or more channels with performance no worse than a single-channel one, while avoiding potential corruptions among signals within channels of interest. Figs. 1.3(a) and 1.3(b) illustrate intra-band CA, in which the desired channels are within the same band, and inter-band CA, where the desired channels are in different bands, respectively, using two channels as an example. The circuit techniques to realize them are also different because of the distance between the two channels.

1.2 Prior Art

In this Section, we briefly review some of the state-of-the-art programmable receiver architectures.

1.2.1 Mixer-First Receivers

Based on the N-path passive mixer, the mixer-first receivers are probably one of the most popular programmable receiver architectures in literature, as shown in Fig. 1.4 [9] with an N of 4. A set of 25% non-overlapping clocks with a fundamental frequency of f_{LO} at the frequency of the local oscillator (LO) drives the switch-based mixer. The RF signal from the antenna is then downconverted to baseband and gets filtered by the baseband filters. This simple approach also upconverts the baseband impedance to RF and hence equivalently achieves in-band impedance matching and out-of-band filtering at RF. Better filtering is possible by constructing the baseband filters with higher orders. Thanks to the relatively simple structure, this architecture can provide good coverage within the sub-6-GHz range. With some modifications, it may even be used for mm-wave applications. However, while achieving wideband programmable receiver with reasonably good linearity due to the absence of voltage gain prior to baseband filtering, the overall noise figure is high due to the lack of an LNA, which can be improved by utilizing either an LNTA or the noise cancellation concept [10]. In addition, it only provides first-order baseband filtering and the out-of-band linearity is limited by the nonlinear switch resistances and baseband amplifiers. The N-path filters are akin to the mixer-first receivers, except some differences regarding how the baseband circuit looks like and where the signal is read. Since relevant literature [11]–[13] is rich, it is omitted here for brevity. Nonetheless, they face similar drawbacks as the mixer-first receivers.

1.2.2 Discrete-Time Receivers

Another popular approach utilizes discrete-time (DT) signal processing, whose concept is visualized in Fig. 1.5 [6], [14], [15]. By sampling the RF signal directly and then processing it through a bank of capacitors that perform charge sharing, due to the memory effects of the capacitors, very high-order filtering can be achieved at baseband, thanks to the high-quality capacitors and switches available in modern CMOS technologies. With in-phase and quadrature (I/Q) channels, it is also possible to realize superheterodyne receivers rather than simple direct conversion, i.e., zero intermediate frequency (IF), in contrast to a standard mixer-first

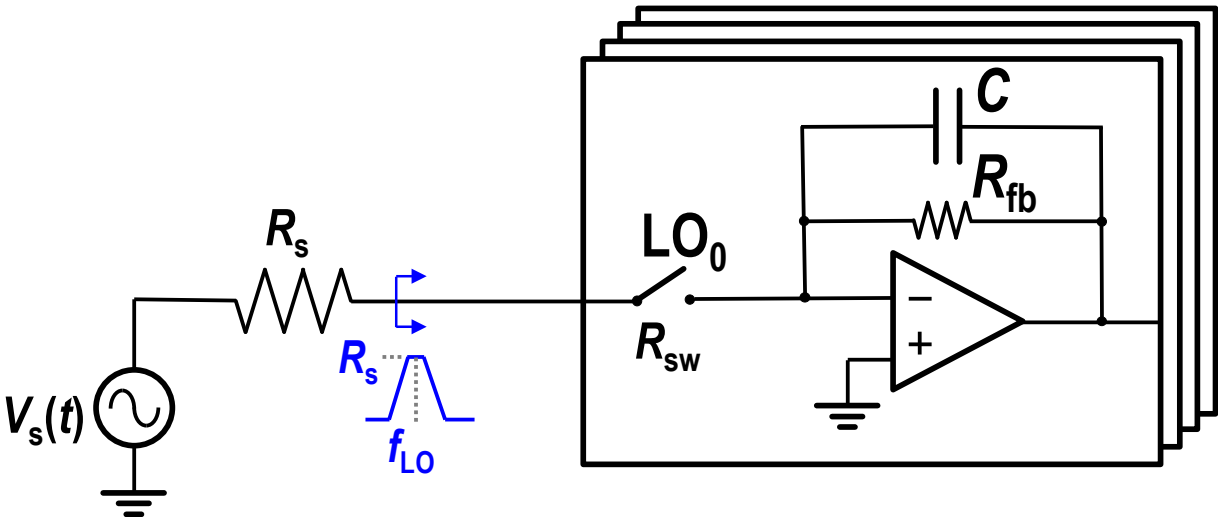

Figure 1.4: Mixer-first receiver architecture.

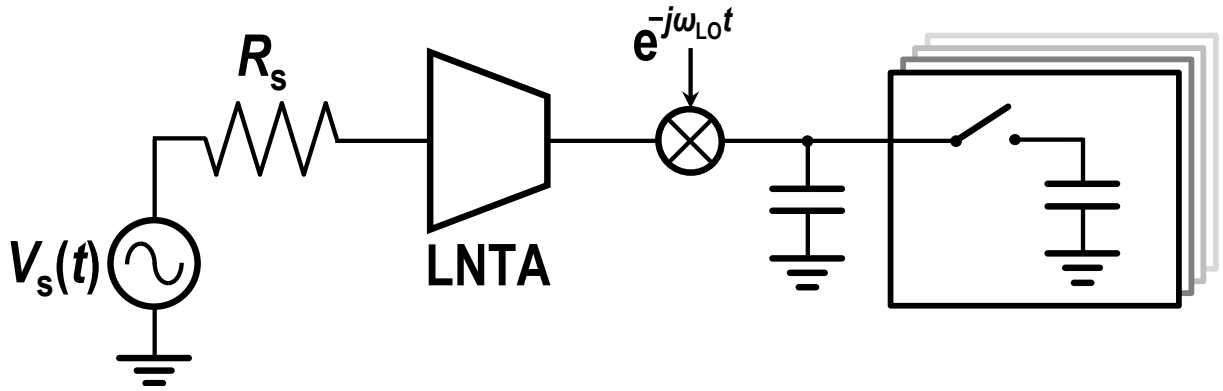

Figure 1.5: DT receiver architecture.

one. However, they typically need an up-front low-noise transconductance amplifier (LNTA) [6], [15], which limits the overall linearity especially in the absence of off-chip SAW/BAW filters, or a switched-capacitor matching network [14], which has limited frequency coverage. Depending on whether an LN(T)A is included, the noise figure could be as low as ∼2–3 dB or as high as up to 10 dB, and the out-of-band IIP_3 can be ranging from ∼10 to ∼30 dBm. Nevertheless, it is a potentially useful technique to achieve receivers with high-order infinite impulse response (IIR) filtering, which can be beneficial for wireless applications, since the stopband rejection can be very high, especially at far-off frequencies where the blockers are potentially the strongest.

1.2.3 Filtering-by-Aliasing Receivers

Recently, the filtering-by-aliasing technique has been developed [16]. Essentially, it achieves analog finite impulse response (FIR) filtering and has been used in a spectrum scanner [17] and receiver front-ends [18], [19]. The former is fully passive and not matched to the antenna, providing no gain either, hence we only talk about the latter here. With a baseband integrator formed by a transconductance (G_{m}) cell and a capacitor under periodical reset in the feedback, a resistor with periodically time-varying (PTV) resistance modulates the signals and sends the currents to the integrator, such that the overall structure forms an analog FIR filter at the sampled output, as shown in Fig. 1.6 [18]. By properly controlling the impulse response, $g(\tau)$, very sharp filtering can be achieved and the filter design process is the same as digital filters, except that $R(t)$ cannot be negative for signal loss considerations and that it may need to provide matching [18]. Note that the mixer is constructed similar to the mixer-first ones, i.e., using passive switches. The programmability is high. Other than LO frequency and bandwidth, the filter shape can be programmed as well just like a standard digital filter, following the fundamental tradeoffs among transition bandwidth, stopband rejection, in-band droop/ripple, etc. Note that the channel bandwidth, unlike mixer-first ones, which is determined by the RC product in the feedback, is determined by the sampling period, T_{s}. The impulse response depends on the source resistance (or impedance, in general), which implies that the receiver is actually processing $V_{\mathrm{s}}(t)$. It will be seen later that this actually could pose some challenges when trying to obtain the optimal performance while the source is not completely 50 Ω, since the ultimately achievable stopband rejection depends on the accuracy of the impulse response [18]. Nevertheless, FA receivers have demonstrated one of the sharpest CMOS band-pass filters, achieving 70-dB stopband rejection with a transition bandwidth (BW) of only 4 times the RF BW. The close-in linearity is also very good.

While providing many benefits, FA receivers also have some limitations, such as relatively high noise level, moderate out-of-band linearity, sensitivity to parasitics, and residual aliases that are no longer separable from the signals, etc. Here we briefly elaborate the attendant

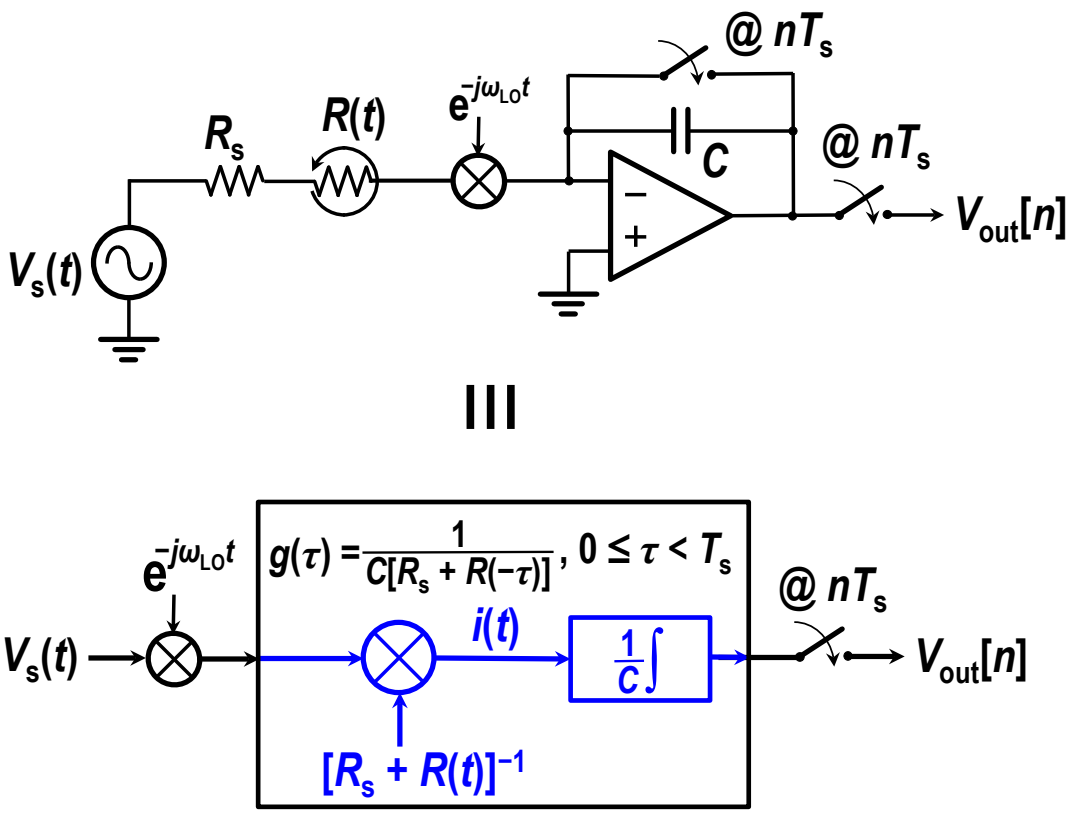

Figure 1.6: FA receiver architecture.

effects. The relatively high noise stems from the time-varying resistor, whose resistance can be large at times, leading to high NF and limiting the smallest detectable signal strength. The moderate out-of-band linearity prevents FA receivers from tolerating extremely strong signals, such as leakage from the output of a power amplifier (PA). While the FA receivers smartly utilize time-varying operations to achieve what time-invariant circuits cannot offer, the interactions between the time-varying circuits in FA filters and other time-invariant and -varying circuit components lead to complicated high-order effects on the filter performance. Note that these other components can be as simple as parasitics. These effects manifest themselves as worsened stopband rejection, widened transition bandwidth, altered filter shape, and so on. Fig. 1.7(a) shows an example of the measured FA receiver filter shape with $f_{\mathrm{LO}} = 740$ MHz and $f_{\mathrm{s}} = 10$ MHz. It is clear that in the transition band, a bump exists, which was not intended during filter design. The residual alias problem originates from the sampling operation, which is a core component in FA filtering. Fig. 1.7(b) shows

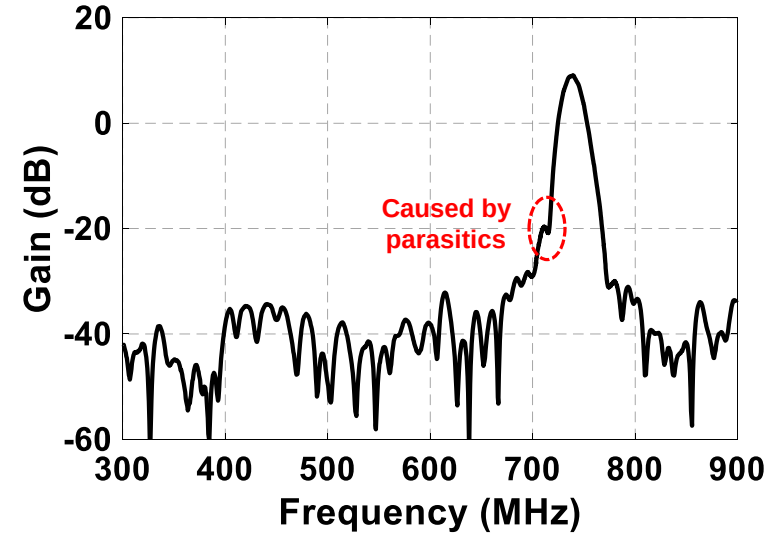

(a)

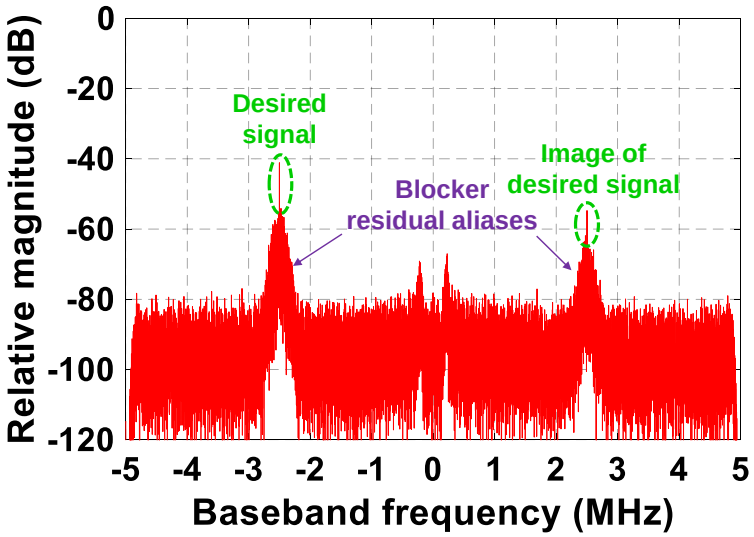

(b)

Figure 1.7: Examples of (a) measured FA receiver filter shape and (b) measured FA receiver output spectrum with a −55-dBm in-band sinusoid at 347.5 MHz and a −5-dBm wideband blocker at 272.5 MHz simultaneously sent to the receiver input (f_{LO} = 350 MHz, f_{s} = 10 MHz).

an example of the measured output spectrum of an FA receiver. Two signals are present, one is a wanted sinusoid, and the other is a wideband blocker. The input powers are −55

and -5 dBm for the wanted signal and blocker, respectively. It can be clearly seen that the blocker residual alias is not completely rejected and falls on top of the tonal signal. In this example, it limits the achievable signal-to-noise ratio. If the blocker is even stronger, or the desired signal smaller, the blocker residual alias will overwhelm the wanted signal. This problem cannot be solved by using filtering stages after the output of the FA receiver since sampling has already taken place. These problems will be detailed in Chapters 2, 3, and 4 together with proposed techniques to tackle some of them.

1.2.4 Receivers for Carrier Aggregation

As described earlier, CA can be classified into intra- and inter-band scenarios. For intra-band CA, the easiest approach is probably to make the receiver maintain a bandwidth that is wide enough to include both channels from the same band and process the signals in the digital domain. This does come at extra power overhead, but for certain applications the band could be relatively narrow, so this could be a viable means. Technology scaling also helps in this regard by reducing the power consumed by the digital circuits. Another approach is to center the LO frequency at the middle of the two desired channels to downconvert the two carriers to low IFs and then separate them through complex signal processing to perform image rejection, as shown in Fig. 1.8(a) [8]. Alternatively, current sinks at different offset frequencies can be generated for directing carriers at different frequencies to different baseband circuitries, depicted in Fig. 1.8(b) [20]. Nevertheless, intra-band carrier aggregation typically has carriers with a relative small frequency distance, often up to several tens of MHz, hence many baseband techniques are possible.

Carriers for inter-band carrier aggregation, on the other hand, are usually separated by hundreds of MHz or more, often requiring multiple receivers in parallel with multiple LOs [21]–[24], because approaches similar to the intra-band ones would require too wide of a bandwidth and hence too much power. However, direct paralleling programmable receivers, such as the mixer-first ones, is not always possible. This is because of the property of the input impedance of a mixer-first receiver being narrowband, as explained in Subsection 1.2.1.

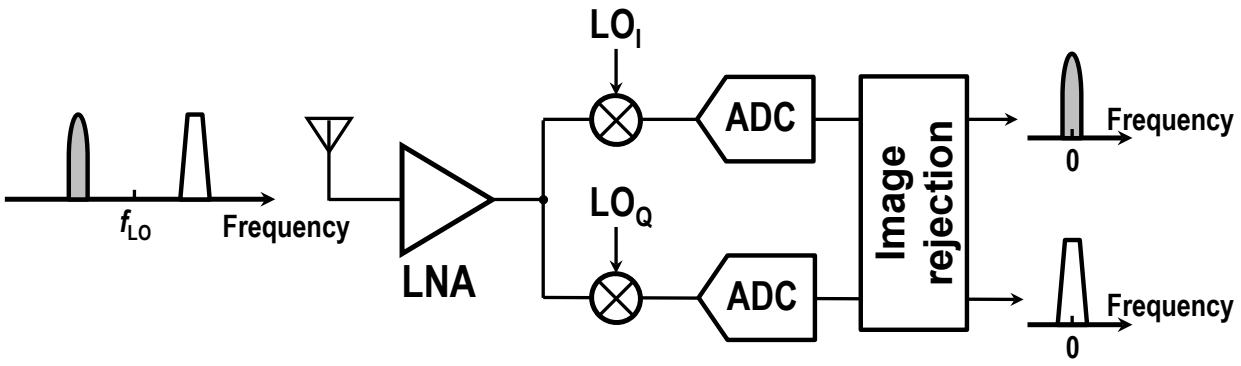

(a)

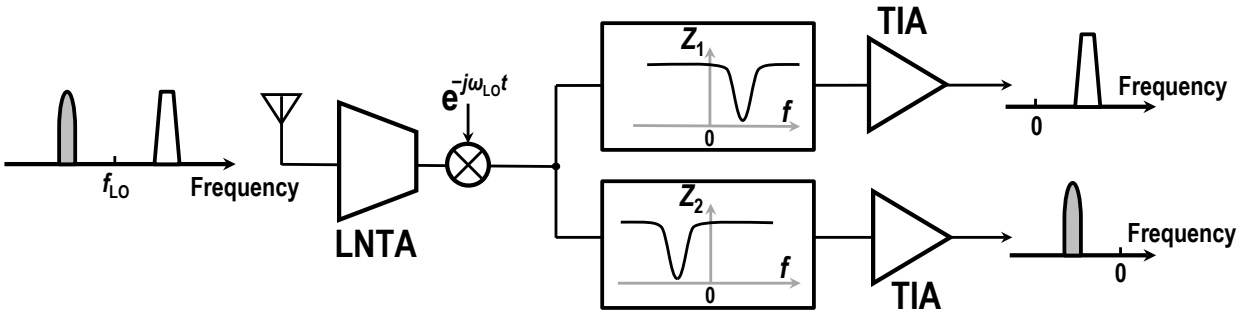

(b)

Figure 1.8: Prior art of intra-band carrier aggregation receivers using (a) baseband image rejection and (b) complex current sinks.

Two or more paralleled mixer-first receivers will lead to an overall low input impedance at all frequencies, which is never matched to the antenna. As a consequence, most state-of-the-art inter-band carrier aggregation receivers utilize LN(T)As to isolate the input impedance from each channel, as illustrated in Fig. 1.9 [24]. Naturally, having active devices at RF without any pre-filtering leads to degraded linearity. As a result, even though many of them achieve relatively good noise performance, their linearity is generally poor.

1.3 Dissertation Outline

This dissertation focuses on developing programmable receiver front-ends using periodically time-varying circuits. More specifically, we have built high-performance receivers by ex-

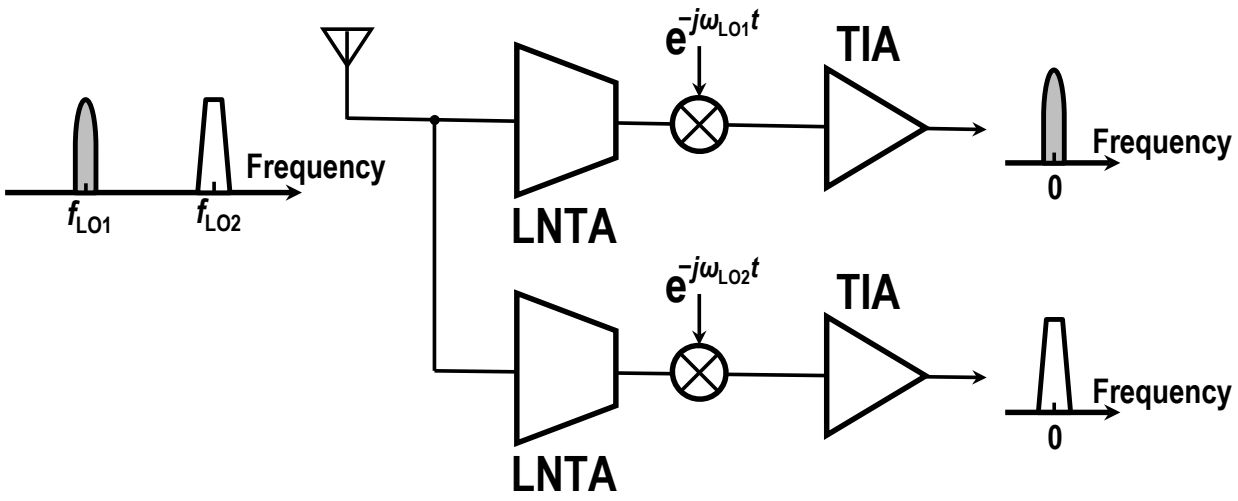

Figure 1.9: Inter-band carrier aggregation receiver.

ploiting the FA technique and concentrated on the development of new techniques for FA receivers to extend their dynamic range while maintaining sharp filtering.

Chapter 2 describes a periodically time-varying noise cancellation technique tailored for FA receivers to lower the noise. Co-design with an up-front N-path filter has been investigated to improve the linearity. This work has been published in part in the *Proceedings of the IEEE Custom Integrated Circuits Conference (CICC)* and in full in the IEEE Journal of Solid-State Circuits.

Chapter 3 details a slice-based FA architecture that provides time-invariant input impedance while maintaining periodically time-varying operation for realizing sharp filtering and enabling carrier aggregation. All switches have been moved within the feedback network to improve the performance, especially in terms of linearity. This work has been published in part in the *IEEE International Solid-State Circuits Conference (ISSCC) Digest of Technical Papers* and accepted for publication in full in the IEEE Journal of Solid-State Circuits.

Chapter 4 develops a digital signal processing technique designed for FA receivers to cancel the undesirable residual aliases at the outputs of FA receivers after sampling.

Finally **Chapter 5** concludes the dissertation by summarizing the key contributions.

CHAPTER 2

Periodically Time-Varying Noise Cancellation for Filtering-by-Aliasing Receiver Front-Ends

2.1 Introduction

As we have briefly discussed in Chapter 1, it has been of significant interest in recent years to explore high-programmability SAW-less transceivers for emerging software-defined and cognitive radios applications [6], [25]. However, without the pre-filtering provided by SAW filters, such receivers face great challenges in simultaneously providing sufficient filtering, linearity, and low noise. Some recent approaches include N-path filters (NPFs) [11], mixer-first receivers [9], [10], and discrete-time (DT) charge-domain signal processing [14]. They have demonstrated moderate filtering (usually equivalent to first- or second-order baseband filters), reasonably high small- and large-signal linearity [approximately +20-dBm out-of-band (OOB) IIP_3 and +10-dBm blocker 1-dB compression point ($\text{B}_{1\text{dB}}$)], good noise performance, and moderate LO and bandwidth (BW) tunability.

The recent filtering-by-aliasing (FA) technique [16]–[19] provides very sharp analog FIR filtering (>70-dB rejection at 4× RF BW offset, i.e., 8× baseband BW offset as RF BW is twice the baseband BW), good linearity (>+20-dBm OOB IIP_3 and +13-dBm $\text{B}_{1\text{dB}}$), and comparable or better programmability. The block diagram of a representative active FA receiver is shown in Fig. 2.1(a), wherein the key component is an input matching resistor that is periodically time-varying (PTV), $R(t) = R(t + T_\text{s})$. Together with a mixer and the baseband integrate-and-dump circuit, equivalently the input signal $V_\text{s}(t)$ is down-converted to baseband and sees an apparent linear time-invariant (LTI) filter at the sampled output, whose impulse response is given by [18]

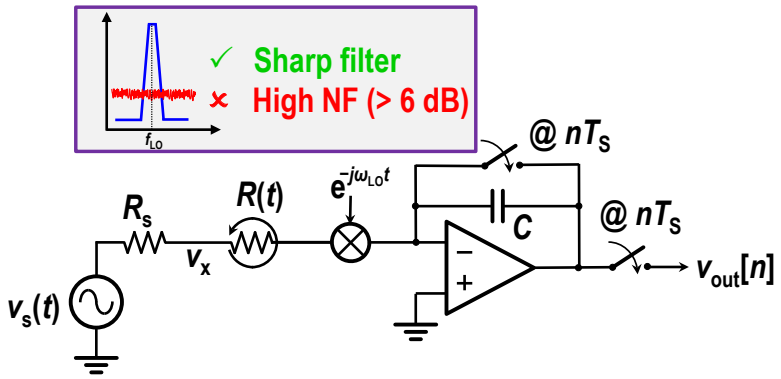

(a)

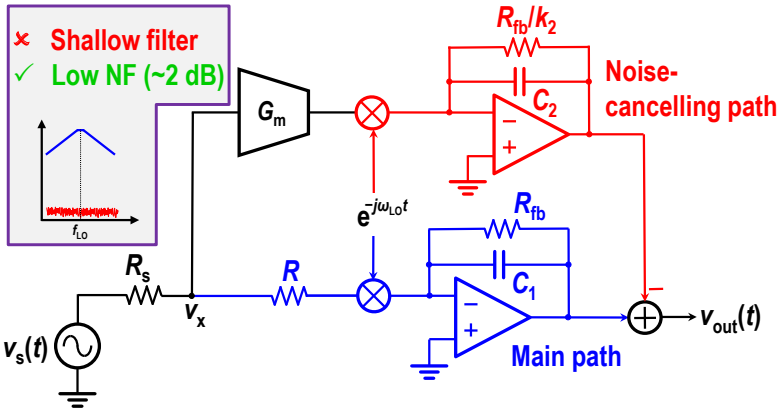

(b)

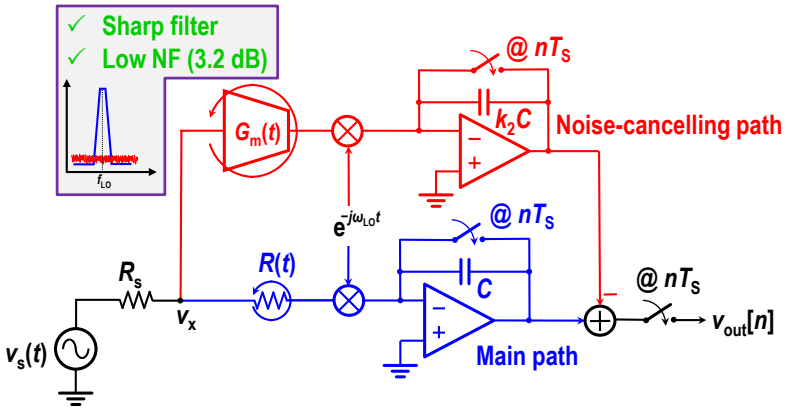

(c)

Figure 2.1: (a) FA receiver using a PTV resistor for sharp filtering, (b) noise cancellation for mixer-first receiver using an LTI G_m cell at RF, and (c) proposed PTV noise cancellation for FA receiver to achieve both sharp filtering and low noise.

$$g(\tau) = \frac{1}{C[R_{\rm s} + R(-\tau)]}, \tag{2.1}$$

where $0 \leq \tau \leq T_{\rm s}$. The FA receiver presents a time-varying impedance to the antenna with an S_{11} given by

$$S_{11} = \text{mean}\left[\frac{R(t) - R_{\rm s}}{R(t) + R_{\rm s}}\right], \tag{2.2}$$

where $R_{\rm s}$ is the antenna impedance (typically 50 Ω). Although the desire for a small S_{11} (typically -10 dB or less) constrains the choice of $R(t)$, fairly arbitrary impulse response shape, $g(\tau)$, and, hence, very sharp analog FIR filtering can be achieved by choosing $R(t)$ appropriately. An example of the $R(t)$ variation and the corresponding baseband filter is shown in Fig. 2.2, which shows that FA is much sharper than a first-order filter. A third-order baseband filter equivalent resulting from a TIA plus biquad combination that is commonly used in traditional mixer-first and N-path designs is also shown for the sake of comparison. Note that the in-band droop, filter transition bandwidth, and stopband attenuation of the FA filter can be traded against each other. Furthermore, sharper filtering was reported using time-interleaving (TI) that also relaxes the S_{11} constraint [19], making it extremely useful for software-defined radio applications. In any case, the overall receiver's noise is fundamentally limited by the noise contribution from $R(t)$. In fact, during part of each period, its value can get very large (>10× the 50-Ω antenna resistance), resulting in an overall high noise figure (NF) of >6 dB after considering the NF degradation due to LO harmonics and filter aliasing [18], [19]. This disadvantage prohibits it from being used in more generic RF environments, where a low NF may be desired.

On the other hand, the noise cancellation (NC) technique has been proven useful to lower the NF of wideband low-noise amplifiers (LNAs) [26]. The frequency-translational NC (FTNC) technique has been successfully extended to mixer-first receivers to cancel the noise contribution of their input matching resistor, and an NF as low as 2 dB was demonstrated in [10]. As shown in Fig. 2.1(b), generic LTI-NC senses the noise voltage from the input matching resistor at the RF node, $V_{\rm x}$, with a transconductance ($G_{\rm m}$) cell and cancels this noise by subtracting the signals at the outputs of the main and NC paths, where a baseband gain factor k_2 is used to control the relative gain between the two paths. In principle, such

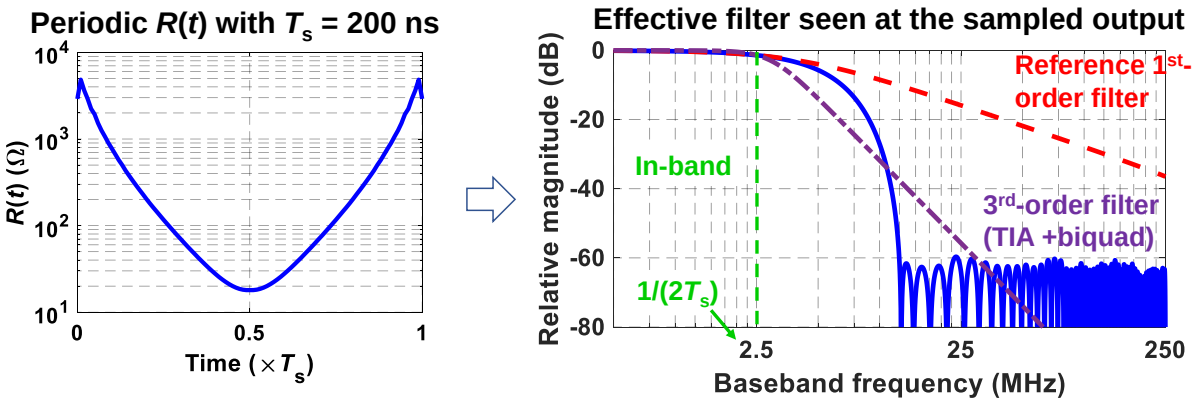

(a)

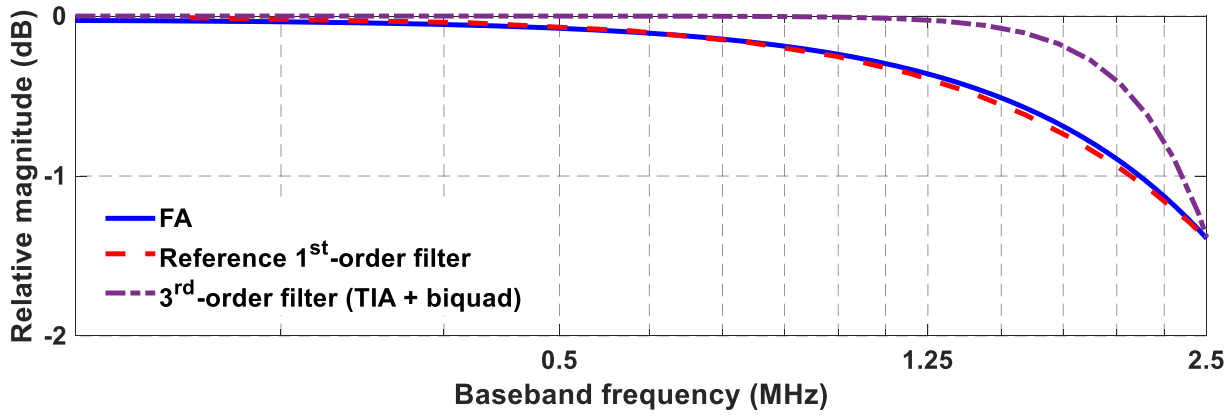

(b)

Figure 2.2: (a) Example of $R(t)$ variation and the corresponding normalized baseband filter and (b) zoom-in view showing the filter droop in the passband.

FTNC can be readily extended to FA receivers as well. However, as will be shown in the next Section, such naïve NC will lower the NF of an FA receiver, but it will negate the sharp filtering of FA.

In this Chapter, a PTV-NC technique tailored for the FA-based receivers is detailed, which improves the average in-band NF ($\text{NF}_{\text{avg,IB}}$) by about 3 dB and achieves a minimum in-band NF ($\text{NF}_{\text{min,IB}}$) of 3.2 dB without noticeable degradation to FA filtering performance, shown in Fig. 2.1(c) [27], [28]. Here, we elaborate the design of the PTV-NC technique [27], [28] together with supporting theoretical analysis on both filtering and noise. In addition, upfront N-path filtering is added to improve the linearity of the front-end. To our best

knowledge, this is the first application of a combination of an upfront N-path filter and an FA receiver. The attendant design considerations are also presented in this Chapter. Section 2.2 details how the naïve application of LTI-NC to FA receivers is not useful and then introduces the proposed PTV-NC technique. Section 2.3 explains the dynamic range (DR) and linearity issue faced by the proposed technique and describes how an upfront N-path filter can be added to the FA receiver to improve DR and linearity without sacrificing the sharp filtering offered by FA. Detailed circuit implementation is presented in Section 2.4, followed by measurement results in Section 2.5.

2.2 Noise Cancellation for FA Receiver Front-Ends

In this Section, we review the LTI noise cancellation technique and detail why it is not suited for FA-based receivers, followed by analysis of the proposed PTV-NC.

2.2.1 LTI-NC in FA-Based Receivers

A naïve application of LTI-NC to FA leads to the implementation of Fig. 2.3(a). In the case where $R(t) = 50\ \Omega$, it is essentially identical to FTNC if one were to ignore the sampling of the final output [10], [26]. The noise voltage of $R(t)$, $V_{\mathrm{nR}}(t)$, leads to two noise currents through the main and auxiliary NC paths, $i_{\mathrm{R}}(t)$ and $i_{\mathrm{Gm}}(t)$, respectively, which are then converted back to voltage at baseband as shown in Fig. 2.3(b), where Z_{bb} is the baseband current-to-voltage conversion gain ($= 1/j\omega C$ in the case of FA). It is straightforward to see that, after voltage subtraction, the noise voltage caused by $R(t)$ is nulled at the output, if G_{m} is selected to be k/R_{s} with $k = k_2$. If R_{s} and $R(t)$ are the only noise sources, this renders a perfect 0-dB NF even though $R(t)$ is a time-varying resistor.

However, unfortunately, the sharp filtering is eliminated: by examining Fig. 2.3(c), which shows how the input signal, $V_{\mathrm{s}}(t)$, is processed, we find that the signal current to be integrated, $i_{\mathrm{s}}(t)$, no longer depends on $R(t)$! This is fundamentally no different from sampling an active-RC integrator.

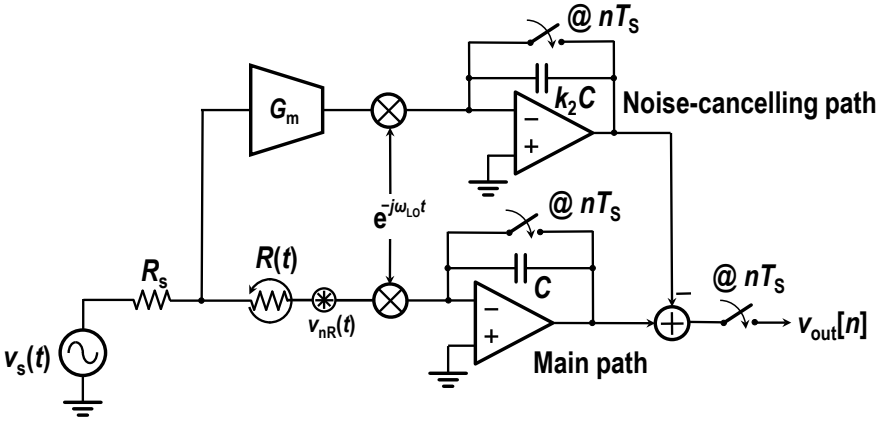

(a)

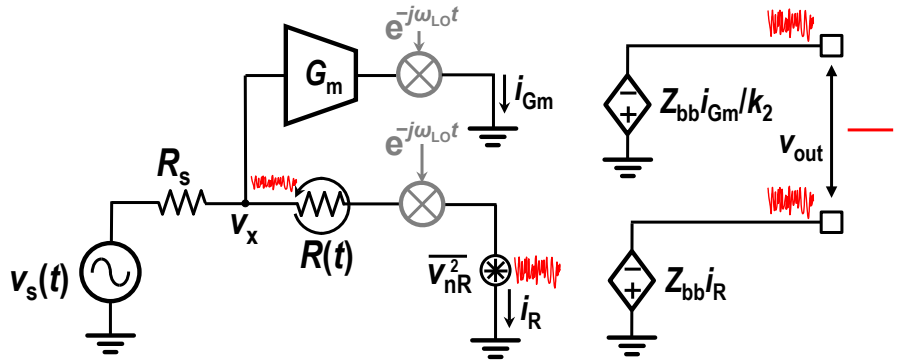

(b)

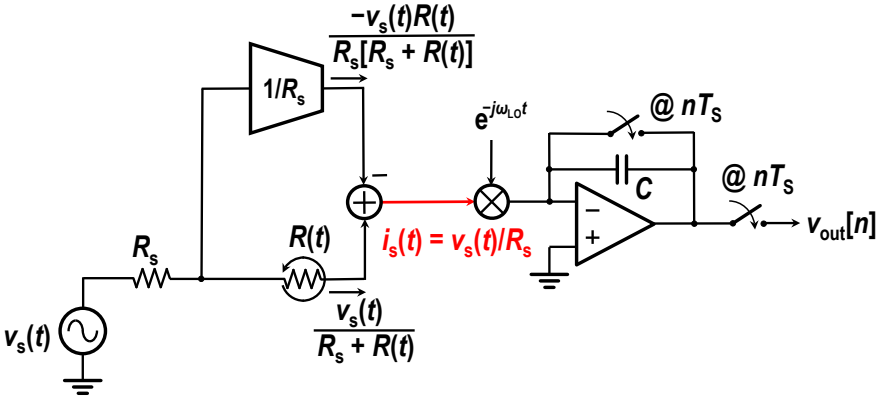

(c)

Figure 2.3: (a) Block diagram of naïve application of LTI-NC to an FA-based receiver, (b) simplified model illustrating perfect NC, and (c) equivalent model for illustration of the destruction of sharp filtering.

2.2.2 Proposed PTV Noise Cancellation

Instead of the usage of an LTI $G_{\rm m}$ cell, we propose to exploit a PTV $G_{\rm m}(t)$ cell to sense $V_{\rm nR}(t)$ at node $V_{\rm x}$ [27], [28], from which the output current is then downconverted, integrated, and sampled to realize the noise-cancelling FA path [see Fig. 2.1(c)]. By replacing the time-invariant $G_{\rm m}$ cell in Fig. 2.3(a) with a time-varying one, the signal and the noise now see different filters. The equivalent signal and noise (due to $R(t)$ only) flows in the front-end are shown in Fig. 2.4(a): $i_{\rm Gm}$ and $i_{\rm R}$ are currents from the $G_{\rm m}$ cell and through $R(t)$ flowing into their respective virtual grounds, which are later integrated. Fig. 2.4(b) shows a simplified model that inspects the signal flow of the noise from $R(t)$ only. In contrast to setting $G_{\rm m}(t) = k/R_{\rm s}$, we select

$$G_{\rm m}(t) = \frac{k_1}{R(t)}.$$

Now $i_{\rm nR}(t)$, which is the effective noise current caused by $R(t)$ after cancellation, is not nulled (i.e., the noise from $R(t)$ is not completely canceled as $i_{\rm nR}(t) = 0$ no longer holds). Instead, it becomes $-V_{\rm nR}(t)\{1-k_1R_{\rm s}/[k_2R(t)]\}/[R_{\rm s}+R(t)]$. However, since the noise currents from the two paths, which have the same polarity, are subtracted, the overall noise after integration is still greatly reduced. On the other hand, as shown in Fig. 2.4(c), the equivalent signal path is almost identical to the FA case. In fact, it is nothing but a scaled version of the original FA filter [due to our choice of $G_{\rm m}(t)$] with a baseband impulse response of

$$g(\tau) = \frac{1 + k_1/k_2}{C[R_{\rm s} + R(-\tau)]}, \tag{2.3}$$

where $0 \le \tau \le T_{\rm s}$. Thus, the FA operation is intact, and sharp filtering is achieved. Note (2.3) is also the effective filter that the source noise sees.

2.2.3 Achievable Noise Cancellation

Since perfect noise cancellation is not feasible with this approach, it is instructive to consider the theoretically maximum achievable cancellation. Consider the noise factor contribution from $R(t)$: it can be calculated by looking at the autocorrelation of the output voltage samples [18], [19]. Here we consider the baseband filter only for brevity. It follows Appendix

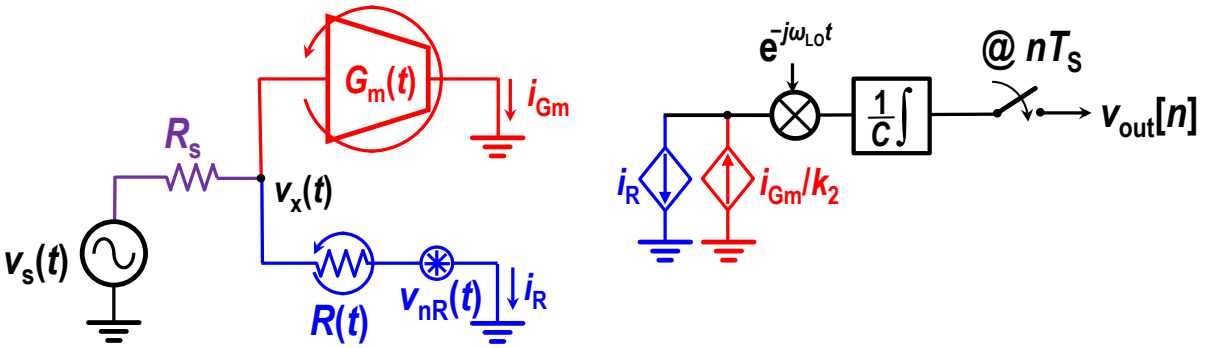

(a)

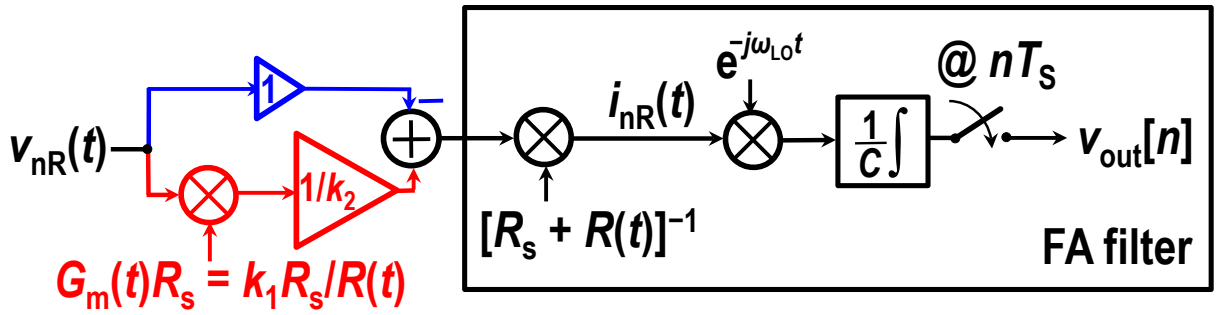

(b)

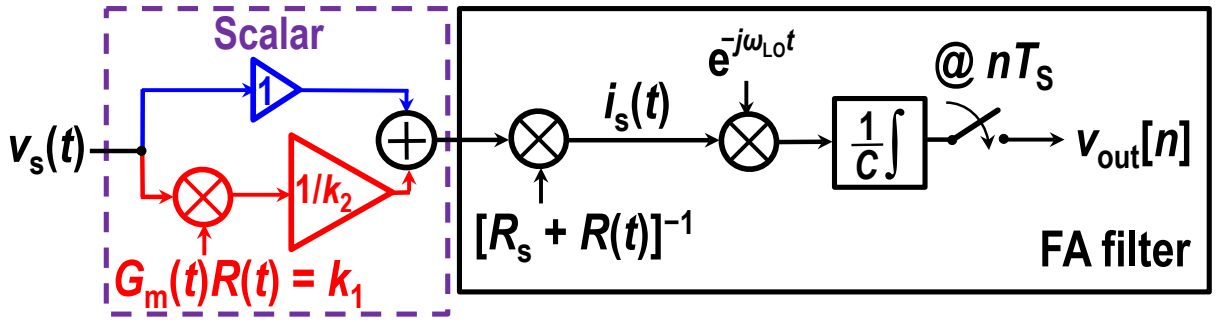

(c)

Figure 2.4: (a) Equivalent model of the proposed PTV-NC in an FA receiver, (b) simplified model for noise, and (c) simplified model for signal.

A that the overall noise factor due to the source and $R(t)$ after cancellation is

$$F_{\mathrm{PTV}} = 1 + F_{\mathrm{R}} = \frac{1 + \lambda^2[\overline{G} - \overline{G_{\mathrm{total}}}]/\overline{G_{\mathrm{total}}}}{(1+\lambda)^2} F_{\mathrm{PTV}}|_{\lambda=0}, \tag{2.4}$$

where F_{R} is the noise factor due to $R(t)$, $\lambda = k_1/k_2$ is effectively the gain ratio between the two paths, $\overline{G} = \mathrm{mean}[1/R(t)]$, $\overline{G_{\mathrm{total}}} = \mathrm{mean}[1/(R_{\mathrm{s}}+R(t))]$, and $F_{\mathrm{PTV}}|_{\lambda=0} = \overline{G_{\mathrm{total}}}/(R_{\mathrm{s}}\overline{G_{\mathrm{total}}^2})$

is the noise factor without any NC, i.e., the noise factor given in Section III-B of [18]. It is unclear, simply by inspecting the expression, what the optimum gain ratio λ ought to be, which can be obtained by setting $\partial F_{\mathrm{PTV}}/\partial\lambda = 0$. After simplification, we find

$$\lambda = \frac{k_1}{k_2} = \frac{\overline{G_{\mathrm{total}}}}{\overline{G} - \overline{G_{\mathrm{total}}}}. \tag{2.5}$$

Substituting (2.5) into (2.4), the minimum achievable noise factor can be found, given by

$$F_{\mathrm{PTV(MIN)}} = \frac{\overline{G} - \overline{G_{\mathrm{total}}}}{\overline{G}} F_{\mathrm{PTV}}|_{\lambda=0}. \tag{2.6}$$

It is straightforward to see that, for LTI-NC, $R(t) = R_{\mathrm{s}}$, $F|_{\lambda=0} = 2$, and (2.5) suggests $\lambda = 1$, plugging which into (2.4) yields $F = 1$, i.e., perfect NC is achieved. For FA, on the other hand, as expected, the optimum gain ratio, achievable amount of noise cancellation, and minimum noise factor depend on $R(t)$. However, (2.6) does provide us with a bound on $F_{\mathrm{PTV(MIN)}}$ due to the minimum value of $R(t)$ in practical implementations. In [18] and [19], it is about 30 Ω. Re-write (2.6), we obtain

$$\begin{aligned} F_{\mathrm{PTV(MIN)}} &= \frac{\int_{t=0}^{T_{\mathrm{s}}} dt/\{R(t)[1 + R(t)/R_{\mathrm{s}}]\}}{\int_{t=0}^{T_{\mathrm{s}}} dt/R(t)} F_{\mathrm{PTV}}|_{\lambda=0} \\ &< F_{\mathrm{PTV}}|_{\lambda=0}/[1 + R(t)_{(\mathrm{MIN})}/R_{\mathrm{s}}] = \frac{5}{8} F_{\mathrm{PTV}}|_{\lambda=0} \end{aligned} \tag{2.7}$$

for $R_{\mathrm{s}} = 50\ \Omega$. Given an assumed noise factor of 2 prior to NC, a noise factor better than 1.25 can be achieved after NC. Here the assumption of noise factor = 2 is a reasonable estimate for $R(t)$ variations that lead to meaningful filter shapes and good impedance matching [18], [19], which can be seen from Fig. 2.5(a) for $k_1/k_2 = 0$, i.e., without NC. More specifically, for the $R(t)$ variation in Fig. 2.2, (2.5) leads to a λ of 0.97, which is very close to that in the LTI case. Fig. 2.5 shows (2.4) for different values of λ in three different filter configurations, where the blue curves correspond to the $R(t)$ variation shown in Fig. 2.2. A couple of things are apparent. First, the optimum gain ratio is close to unity. Second, the optimum is fairly shallow suggesting that achievable noise cancellation is tolerant to relative gain mismatches between the main and NC paths. Third, the optimum noise factor is actually about 1.1, indicating that about 90% of the noise of $R(t)$ is canceled.

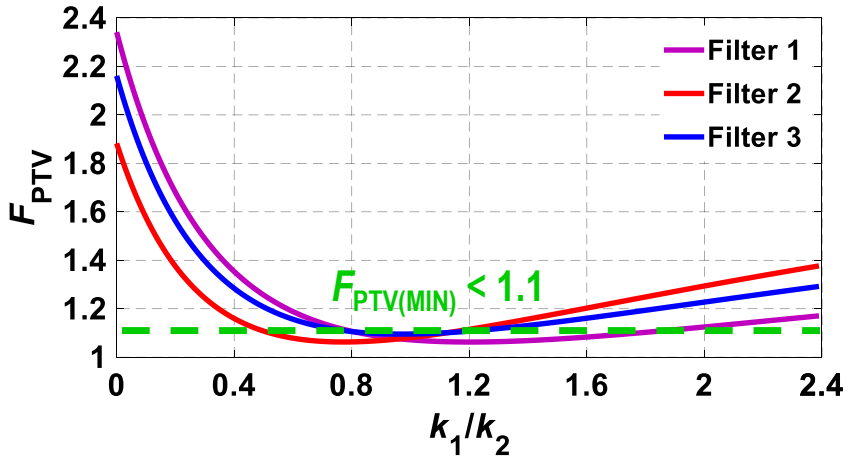

(a)

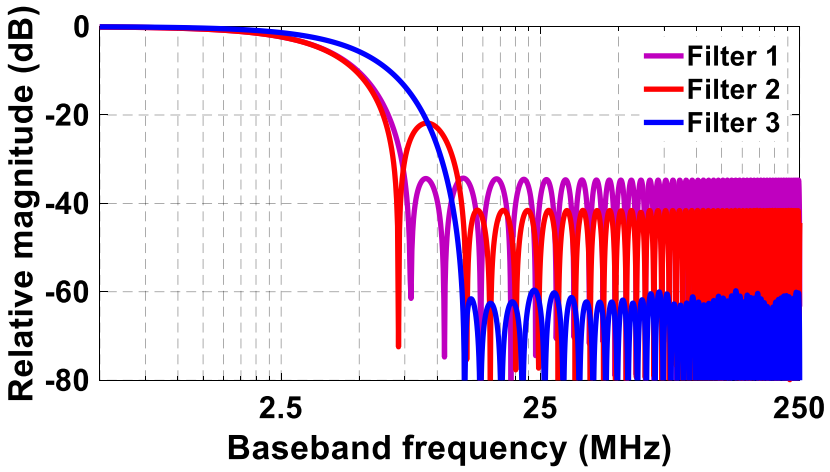

(b)

Figure 2.5: (a) Noise factor with the PTV-NC for different gain ratio, $\lambda = k_1/k_2$, in three different filter configurations, and (b) the corresponding baseband filter frequency responses with $T_s = 200$ ns. Filter 1: transition BW = 1× RF BW, $S_{11} \approx -10$ dB; filter 2: transition BW = 2× RF BW, $S_{11} \approx -20$ dB; filter 3: transition BW = 2× RF BW, $S_{11} \approx -10$ dB (i.e., same as Fig. 2.2).

Note until here the only noise sources are R_s and $R(t)$ for simplicity. In practice, with $R(t)$'s noise mostly canceled, $G_m(t)$'s noise becomes important. To evaluate this, an extra term, derived following Appendix A as well, given by

$$F_{Gm} = \frac{1}{k_1} \frac{\gamma \overline{G(t)}}{R_s(1+1/\lambda)^2 \overline{G^2_{total}(t)}}, \tag{2.8}$$

where γ is the excess noise factor, needs to be added to (2.4) for the overall noise factor. Such summation can be done due to the fact that the noise from $G_{\mathrm{m}}(t)$ is not correlated with that of $R(t)$ and only appears in the NC path. Since λ is a constant for a given $R(t)$ ($\approx$ 1 in most practical cases), in order to minimize F_{Gm}, k_1 needs to be made large according to (2.8). In fact, as $k_1 \to +\infty$, the noise contribution from $G_{\mathrm{m}}(t)$ can be made close to zero. However, this will lead to infinite power consumption and infinite baseband capacitor size. Practical selection of k_1 and k_2 is made by making the contribution of $R(t)$ and $G_{\mathrm{m}}(t)$ to be roughly the same, rendering $k_1 = k_2 = \sim$5 to 6. Here, we only discussed the noises from circuit elements. Other major sources of NF degradation, namely, aliasing and harmonic folding, will be discussed in Subsection 2.3.4.

An alternative, and maybe more intuitive but not completely mathematically precise, approach to looking at how the proposed PTV-NC still effectively cancels the noise is to look at the equivalent filter that $V_{\mathrm{nR}}(t)$ sees. For the baseband FA without NC, i.e., main path only, the baseband filter is the same as (2.1) but with a negative sign. With NC, the baseband filter that $V_{\mathrm{nR}}(t)$ sees becomes

$$h(\tau) = \frac{\lambda R_{\mathrm{s}} - R(-\tau)}{CR(-\tau)[R_{\mathrm{s}} + R(-\tau)]} = g(\tau) - \frac{\lambda R_{\mathrm{s}}}{R(-\tau)} \times g(\tau), \tag{2.9}$$

where $0 \leq \tau \leq T_{\mathrm{s}}$. The frequency response of $h(\tau)$ can be found by taking the Fourier transform, given by

$$H(j\Omega) = G(j\Omega) - \lambda \mathcal{F}\left[\frac{R_{\mathrm{s}}}{R(-\tau)}\right] * G(j\Omega), \tag{2.10}$$

where * is the convolution operator. Note that $G(j\Omega)$ is designed to be a low-pass filter (e.g., Fig. 2.2). $\mathcal{F}[R_{\mathrm{s}}/R(-\tau)]$ is also low-pass, which means the convolution between $\mathcal{F}[\lambda R_{\mathrm{s}}/R(-\tau)]$ and $G(j\Omega)$ is still low-pass, albeit with a larger bandwidth than both filters. There exists a λ such that $H(j\Omega) \approx 0$ in the passband, thus rejecting most of the noise from $R(t)$. Since the source noise is not rejected [seen from (2.3)], while the noise of $R(t)$ is rejected, the noise factor contribution from $R(t)$ becomes slim, i.e., its noise is canceled. Based on the definition of noise figure, the noise figure is lowered.

2.3 Dynamic Range and Linearity Enhancement

It is well known that noise cancellation can degrade the linearity because of the G_{m} stage [10]. Similar effect is expected in PTV-NC as well. However, the effect is worse here because V_{x} sees higher swings. At the RF node, the voltage is

$$V_{\mathrm{x}}(t) = \frac{V_{\mathrm{s}}(t)R(t)}{R_{\mathrm{s}} + R(t)}. \tag{2.11}$$

Recall the fact that $R(t)$ can be very large at times, e.g., Fig. 2.2, such that $R(t) \gg R_{\mathrm{s}}$, and hence $V_{\mathrm{x}}(t) \approx V_{\mathrm{s}}(t)$. If we assume $V_{\mathrm{s}}(t)$ is a simple sinusoid at an arbitrary frequency of interest with an amplitude of A, it is obvious that $V_{\mathrm{x,pk\text{-}pk}} \approx V_{\mathrm{s,pk\text{-}pk}} = 2A$. Note this is the case for both in-band and out-of-band signals since the FA-based receiver has no frequency selectivity at the RF node (as suggested by the ideally frequency-independent S_{11}, which is only somewhat frequency-dependent in practice because of the parasitic capacitance at the RF node) [18], [29]. Consequently, for a big OOB blocker, V_{x} suffers from large voltage swings that may be outside the voltage range of core MOSFET devices in advanced nodes. We address this by employing time-interleaving (TI) and an N-path filter [27], [28], and we analyze their effects and design considerations here.

2.3.1 Time-Interleaved FA

In [19], time-interleaved FA is used to improve both impedance matching and filter performance. By using two interleaved channels, as shown in Fig. 2.6, the length of $g(\tau)$ can be doubled, allowing a stopband rejection (A_{stop}) twice as high in theory. In addition, the overall dynamic range of the input resistance seen by the source is less due to the paralleled operation, which is given by $R_{\mathrm{TI}}(t) = R(t)||R(t - T_{\mathrm{s}})$. In the non-TI case, the highest value of $R(t)$ can be a few thousands of Ohms [18]. When TI is used, $\max[R(t)||R(t-T_{\mathrm{s}})]$ is about 300 Ω. Not only does this makes the input matching easier without having to sacrifice filter shape much for better S_{11} [19], but it slightly reduces $V_{\mathrm{x,pk\text{-}pk}}$ for the same blocker level. Referring to (2.11), the swing at V_{x} is lowered by about 15% (0.5 V for a +10-dBm blocker). Although this only slightly relaxes the DR problem instead of solving it, TI is nonetheless

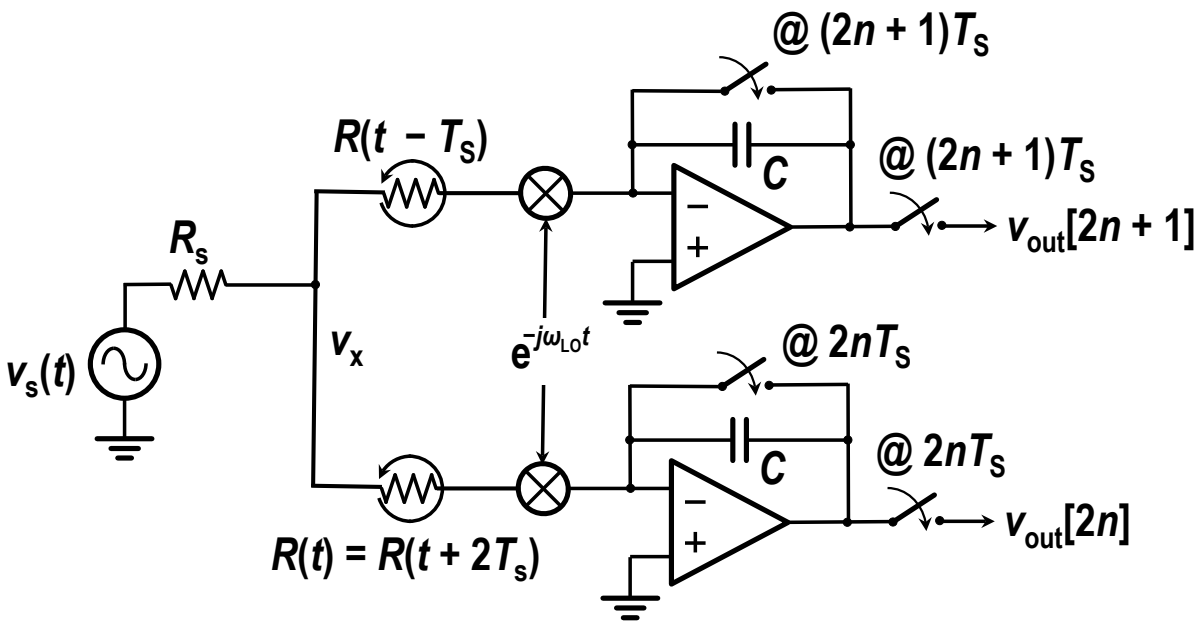

Figure 2.6: Time-interleaved FA receiver.

used in this work to achieve better matching and sharper filter at the cost of higher power and larger chip area for two extra paths (one for the main path and one for the NC path).

2.3.2 Upfront N-Path Pre-Filtering

An upfront NPF will reduce the swing on $V_{\rm x}$ and relax the linearity requirements of the NC path [11], [30]. A block diagram of such a combination of an FA receiver, with a time-varying resistor, $\tilde{R}(t)$, and an upfront NPF is shown in Fig. 2.7(a).

For in-band signals, the NPF presents a high impedance and has minimal effect on $V_{\rm x}$ or the current flowing into the PTV resistor, $\tilde{R}(t)$. In contrast, for signals well beyond the NPF's BW, the NPF presents a low impedance, approximately $R_{\rm sw}$, as shown in Fig. 2.7(b). Since $R_{\rm sw} \ll \tilde{R}(t)$, $V_{\rm x}$ is effectively much smaller than without the NPF:

$$V_{\rm x}(t) \approx V_{\rm s}(t)\frac{R_{\rm sw}}{R_{\rm sw}+R_{\rm s}} = V_{\rm s}A_{\rm NPF}, \tag{2.12}$$

as desired, where $A_{\rm NPF} = R_{\rm sw}/(R_{\rm s}+R_{\rm sw})$ is the rejection provided by the NPF. However, the small $R_{\rm sw}$ siphons away much of the signal current from $\tilde{R}(t)$ in a time-varying manner, greatly degrading the effective FA filter shape.

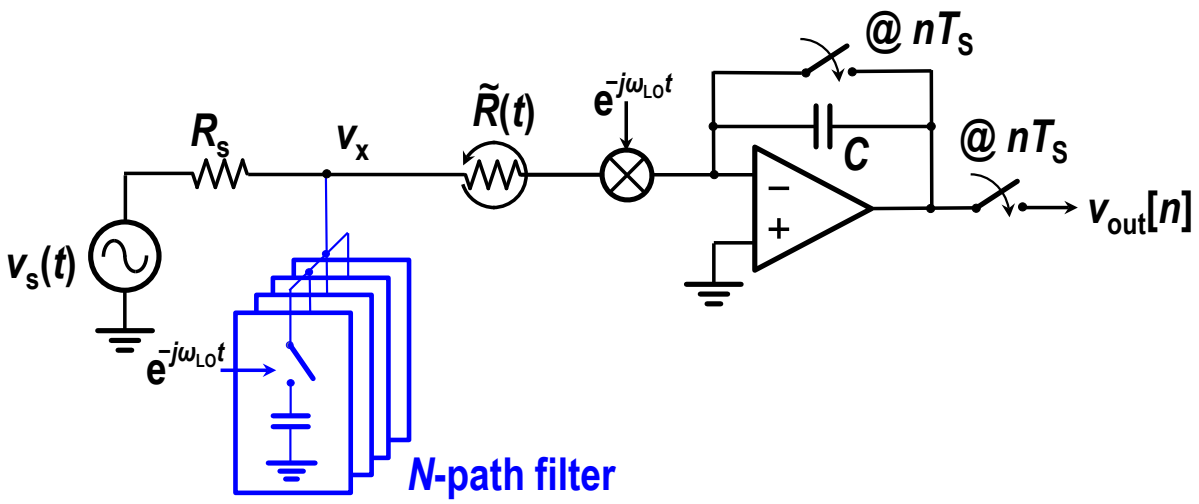

(a)

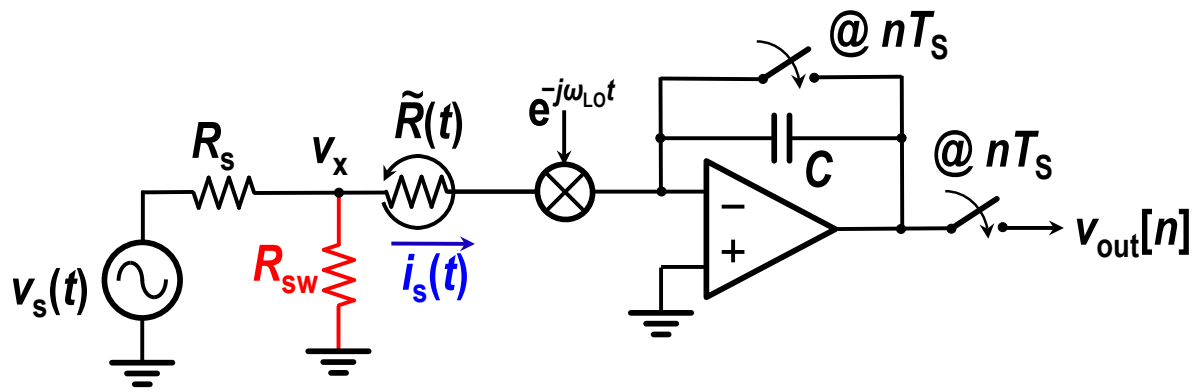

(b)

Figure 2.7: (a) An FA-based receiver with an NPF at the RF node and (b) equivalent circuit for OOB blockers.

Both effects are readily illustrated using an example $\tilde{R}(t) = R(t)$ designed for 60-dB A_{stop}, 10-MHz RF BW, and 20-MHz transition bandwidth with and without an NPF with 30-MHz BW and -15-dB A_{NPF}. As shown in Fig. 2.8, the NPF reduces the swing at V_{x} for a 10-dBm blocker from 4 V to just 0.77 V. However, as is evident from the effective filter responses, without and with the NPF, plotted in Fig. 2.9, the transition bandwidth is almost doubled even as a higher overall A_{stop} is achieved.

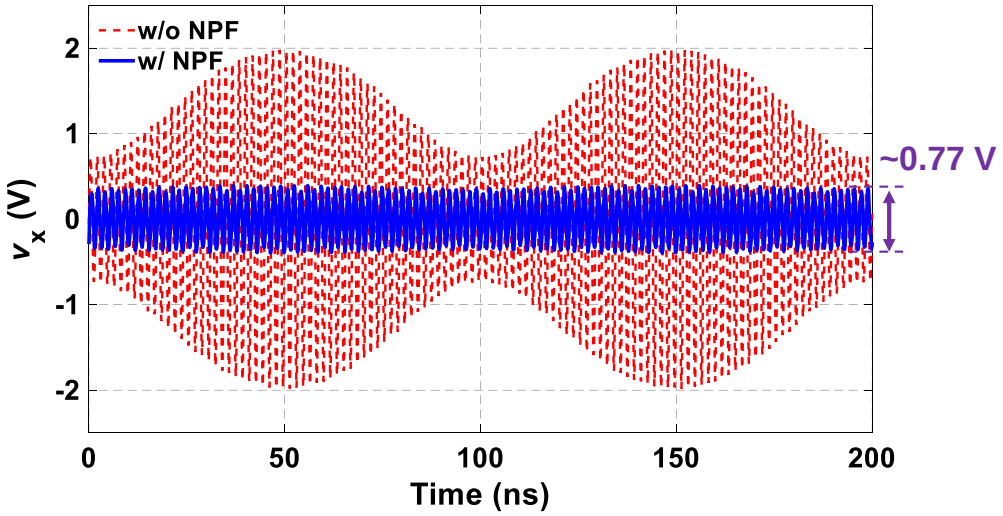

Figure 2.8: Simulated voltage waveform at node V_x of the circuit in Fig. 2.7(a) for a 10-dBm OOB blocker ($\Delta f = 80$ MHz) with and without NPF.

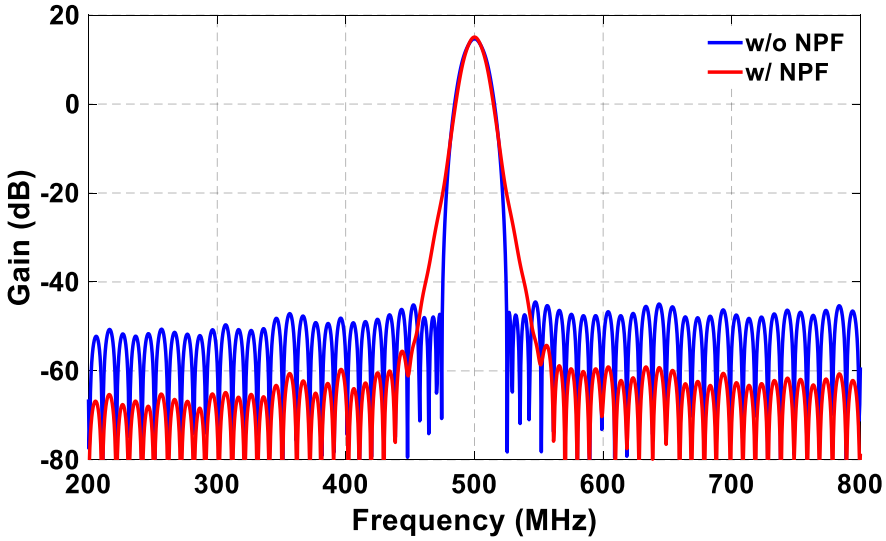

Figure 2.9: Simulated frequency responses of the receiver in Fig. 2.7(a) without and with NPF at $f_{\mathrm{LO}} = 500$ MHz [when with the NPF, $\tilde{R}(t) = R(t)$].

Fortunately, the filter shape degradation can be corrected simply by choosing

$$\tilde{R}(t) = \beta[R_{\mathrm{s}} + R(t)], \tag{2.13}$$

where $R(t)$ is the PTV resistor variation that ensures the desired filter shape for an FA

receiver without the upfront NPF, and β is a constant scaling factor.

Rationale: This choice can be intuitively explained by contrasting Fig. 2.7(b) with Fig. 2.1(a), which represents the desired FA operation without an NPF. It is easy to see that for a signal well beyond the NPF's BW, the current through $\tilde{R}(t)$ in Fig. 2.7(b) is just a scaled version of the current through $R(t)$ in Fig. 2.1(a), given by

$$i_{\mathrm{s}}(t) \approx V_{\mathrm{s}}(t)\frac{R_{\mathrm{sw}}}{R_{\mathrm{sw}}+R_{\mathrm{s}}}\frac{1}{\tilde{R}(t)} = \frac{R_{\mathrm{sw}}}{R_{\mathrm{sw}}+R_{\mathrm{s}}}\frac{V_{\mathrm{s}}(t)}{\beta[R_{\mathrm{s}}+R(t)]}. \tag{2.14}$$

Consequently, the OOB filter shape remains effectively the same as what would be achieved without the NPF.

The simulated overall filter shape with (2.13) is shown in Fig. 2.10(a). As is evident, most of the filter sharpness is restored (transition bandwidth is only extended by ∼6 MHz instead of over 20 MHz while A_{stop} is a few dB higher than the original FA). The filter shape is primarily defined by FA while the NPF adds extra rejection at high offset frequencies. Note that this approach results in a slightly larger in-band filter droop, as seen in Fig. 2.10(b), which is generally acceptable.

Choice of NPF BW and Switch Size: In this work, the NPF BW is chosen to be slightly larger than the desired RF BW of FA. It is however worth noting that the actual NPF BW can be chosen to provide more rejection for close-in blockers by using narrower BW in order to meet certain blocker profiles. This comes at having larger overall filter droop, but it can be remedied by re-designing FA to compensate for the extra signal loss by sacrificing some transition BW or A_{stop}. The NPF switch size choice is driven by the tolerable swing at the RF input node, V_{x}, and the desired OOB IIP_3. Assuming a perfectly linear NPF, which is a fair assumption since the NC path dominates the nonlinearity, with the attenuation of A_{NPF}, the intercept point amplitude is approximately $\sqrt{4|G_{\mathrm{m}}|/3|G_{\mathrm{m3}}|}/A_{\mathrm{NPF}}$, where G_{m3} is the third-order polynomial coefficient of the transconductance. Therefore, the OOB IIP_3 will be roughly improved by $|A_{\mathrm{NPF}}|$. In this work, we chose an equivalent 2.5-Ω switch resistance and a BW of 30 MHz for a 10-MHz RF BW configuration to keep the swing at RF within 0.9 V for a +10-dBm blocker and improve the OOB IIP_3 by about 15 dB at 80-MHz offset.

Note also that the NPF changes the effective S_{11} of the FA receiver slightly. A frequency-

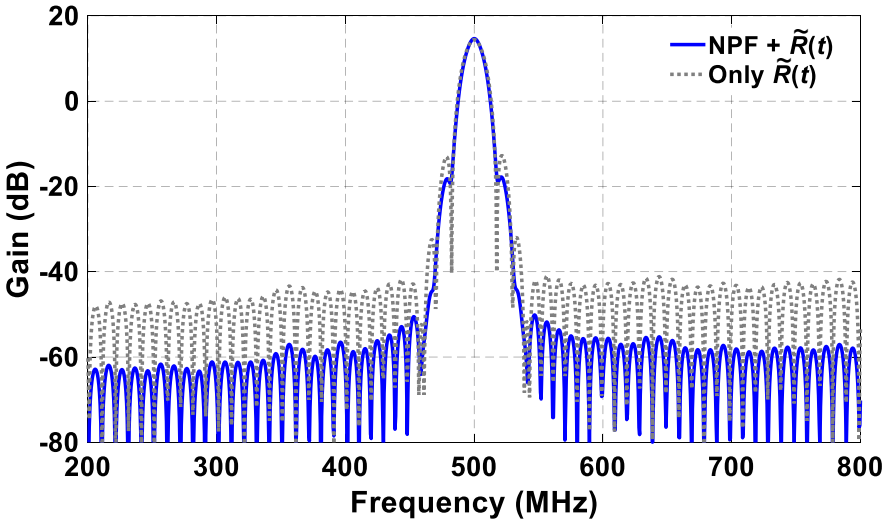

(a)

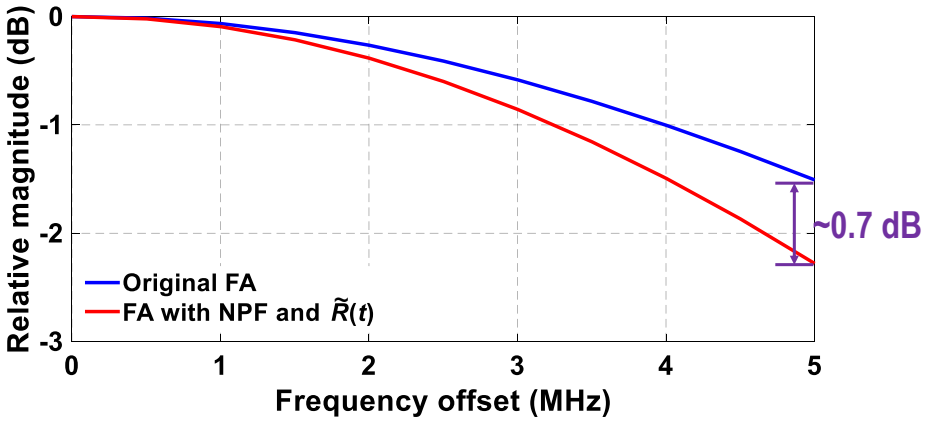

(b)

Figure 2.10: (a) Simulated frequency response of the receiver with adjusted $\tilde{R}(t)$ values with and without NPF and (b) in-band filter shape comparison between FA without NPF and FA with both NPF and adjusted $\tilde{R}(t)$ values.

domain analysis with conversion matrices has been employed before to compute the S_{11} and the effective in-band impedance of an FA receiver [29], [31], [32]. The same approach was extended to the FA + NPF combination described here, after which the scaling factor, β, was chosen to fine-tune the impedance matching.

2.3.3 Upfront NPF plus TI-FA

Extending the design analysis to TI-FA can be achieved in a similar manner. By recognizing the low impedance presented by the NPF, the OOB signal current flowing through each time-varying resistor can be calculated even when two TI resistors are involved [similar to (2.14)], and the resistor variations can therefore be modified to keep the impulse response a scaled version of the original filter for OOB signals as well. Here, we omit the details for the sake of brevity.

2.3.4 Simplified NF Analysis for the Overall Front-End

The noise sources in the NPF (from its switch resistance) are much smaller than other noise sources and can be negligible. Since the overall filter shape is primarily determined by FA [recall Fig. 2.10(a)], the NPF's effect on the noise spectrum can be ignored. Behavioral simulation results suggest that a discrepancy of less than 0.1 dB in the averaged in-band NF is seen by ignoring these effects.

If TI were not employed, the noise analysis presented in Subsection 2.2.3 could be directly used here simply by replacing $R(t)$ in (2.4)–(2.7) with $\tilde{R}(t)$. The effect of TI can be easily approximated by ignoring interactions between the two paths, which is still reasonably viable because the TI channel interaction happens only when $\tilde{R}(t) \approx \tilde{R}(t - T_\mathrm{s})$, which is a short period of time [19], and the correlation between two output samples is small. In this case, the two TI channels contribute independent noise of identical statistics in a TI manner. When combined together, it is as if a single non-TI FA receiver employing a time-varying resistor $\tilde{R}(t)$ [19]. Accordingly, the baseband noise figure can be determined as $\mathrm{NF}_\mathrm{baseband} = 10\log_{10}(F_\mathrm{PTV} + F_\mathrm{Gm})$.

However, the TI channels do interact, resulting in correlation between samples of the output noise. This effect has been described in [19] for a system without NC. Similar calculations can be performed here (see Appendix A) to calculate the precise NF contribution of the input matching resistors and G_m cells. The resultant $\mathrm{NF}_\mathrm{baseband}$ is now a function of the baseband frequency, Δf, where $|\Delta f| \leq 1/(2T_\mathrm{s})$. Fig. 2.11(a) plots the calculated NF

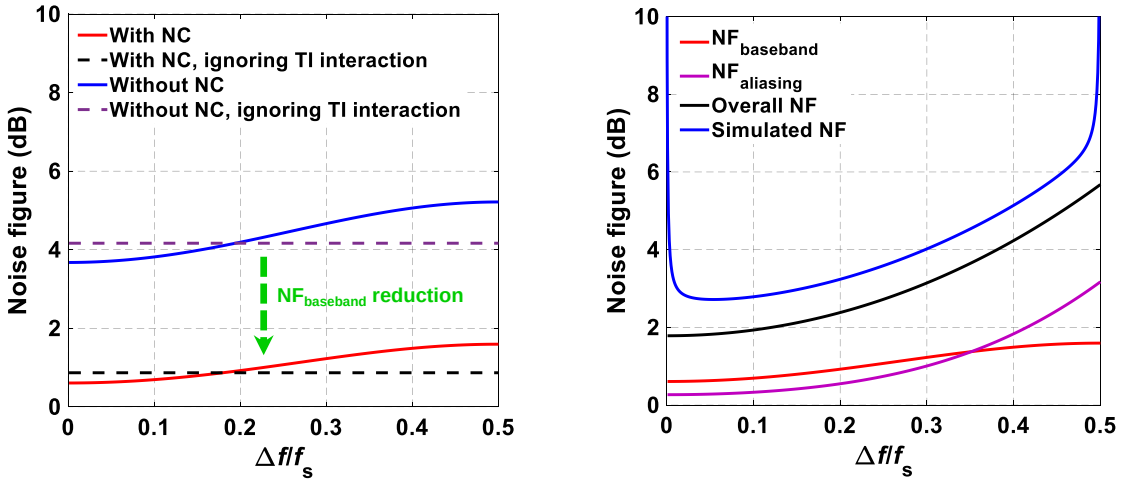

(a) (b)

Figure 2.11: (a) Comparison of the calculated $\mathrm{NF}_{\mathrm{baseband}}$ with and without NC and (b) calculated $\mathrm{NF}_{\mathrm{baseband}}$, $\mathrm{NF}_{\mathrm{aliasing}}$, and calculated and simulated overall NF with $f_{\mathrm{LO}} = 500$ MHz with both NC and NPF ($\beta = 0.54$).

with and without NC for both the cases where the TI channel interaction is considered (solid curves) and ignored (dashed curves). The approximation ignoring the TI interaction only introduces a small error on $\mathrm{NF}_{\mathrm{baseband}}$, albeit making it frequency-independent. The average in-band $\mathrm{NF}_{\mathrm{baseband}}$ error is less than 0.2 dB with approximation. In either case, NC is observed and the average $\mathrm{NF}_{\mathrm{baseband}}$ is lowered by about 3 dB. In our calculation, the baseband amplifiers' noises are taken care of in two means: 1) the amplifiers in the main path present themselves as part of $\tilde{R}(t)$ and $\tilde{R}(t - T_{\mathrm{s}})$ [19], and their noises get mostly canceled; 2) those in the NC path still present their noises but they are suppressed due to the gain of the G_{m} cells just as in [10] (moreover, the baseband amplifiers in this work are designed to have large g_{m}). The passive mixers' switch noises are considered similarly: 1) main-path mixer's switch noise gets mostly canceled; 2) the NC-path mixer contributes little noise.

In addition to $\mathrm{NF}_{\mathrm{baseband}}$, two additional sources also contribute to the overall NF, namely the aliasing of the source noise as a result of sampling at the output and harmonic folding

due to the N-path operation. They are given by [18]

$$\mathrm{NF}_{\mathrm{aliasing}}(\Delta f) = \frac{\mathrm{PSD}_{\mathrm{Rs}}(\Delta f)}{2kTR_{\mathrm{s}}|G(\Delta f)|^2} = \frac{\sum_{n=-\infty}^{+\infty}|G(\Delta f + nf_{\mathrm{s}})|^2}{|G(\Delta f)|^2},$$
$$\mathrm{NF}_{\mathrm{harminocs}} = \frac{1}{\mathrm{sinc}^2(1/N)} \approx 0.91 \text{ dB}, \tag{2.15}$$

where $\mathrm{PSD}_{\mathrm{Rs}}(\Delta f)$ is the power spectral density due to noise from R_{s}, $f_{\mathrm{s}} = 1/T_{\mathrm{s}}$ is the sampling rate at the output, $G(f)$ is the frequency response of the filter, $g(\tau)$, and N is the number of paths in the NPF and mixer, which is 4 in our implementation. Note $\mathrm{PSD}_{\mathrm{Rs}}(\Delta f)$ can also be computed by looking at the autocorrelation of the output sampled voltages [19].

Finally, the overall NF at a certain Δf for the complete system can be derived as

$$\mathrm{NF}_{\mathrm{total}}(\Delta f) = \mathrm{NF}_{\mathrm{baseband}}(\Delta f) + \mathrm{NF}_{\mathrm{aliasing}}(\Delta f) + \mathrm{NF}_{\mathrm{harmonics}}. \tag{2.16}$$

The calculated NF with PTV-NC and NPF is shown in Fig. 2.11(b) in comparison with the simulated results (the simplified analysis model without actually introducing the NPF is used for calculation only, not for simulations). With both NC and NPF, the calculated $\mathrm{NF}_{\mathrm{min,IB}}$ is 1.8 dB and $\mathrm{NF}_{\mathrm{avg,IB}}$ is 3.2 dB. The simulation results agree well with calculation, except for an extra NF degradation of about 0.8 dB mostly due to the loss caused by input parasitic capacitance [19]. The peaking close to dc is due to flicker noise, and as a consequence of the TI operation, half of the flicker noise power being shifted up to $f_{\mathrm{s}}/2$ is observed, similar to that in [19].

2.4 Circuit Implementation

Fig. 2.12 shows the block diagram of the implemented PTV-NC receiver front-end. The values of k_1 and k_2 are programmable but are roughly set to 5–6 by design for best trade-off between $G_{\mathrm{m}}(t)$'s noise contribution and area. The receiver front-end consists of only switches, inverter-based amplifiers, digital circuits, and passive devices (namely, resistors and capacitors).

$R_{1,2}(t)$ are implemented as two 13-bit binary resistor DACs (RDACs) [see Fig. 2.13(a)]. The switches are implemented by transmission gates with equally sized pFETs and nFETs,

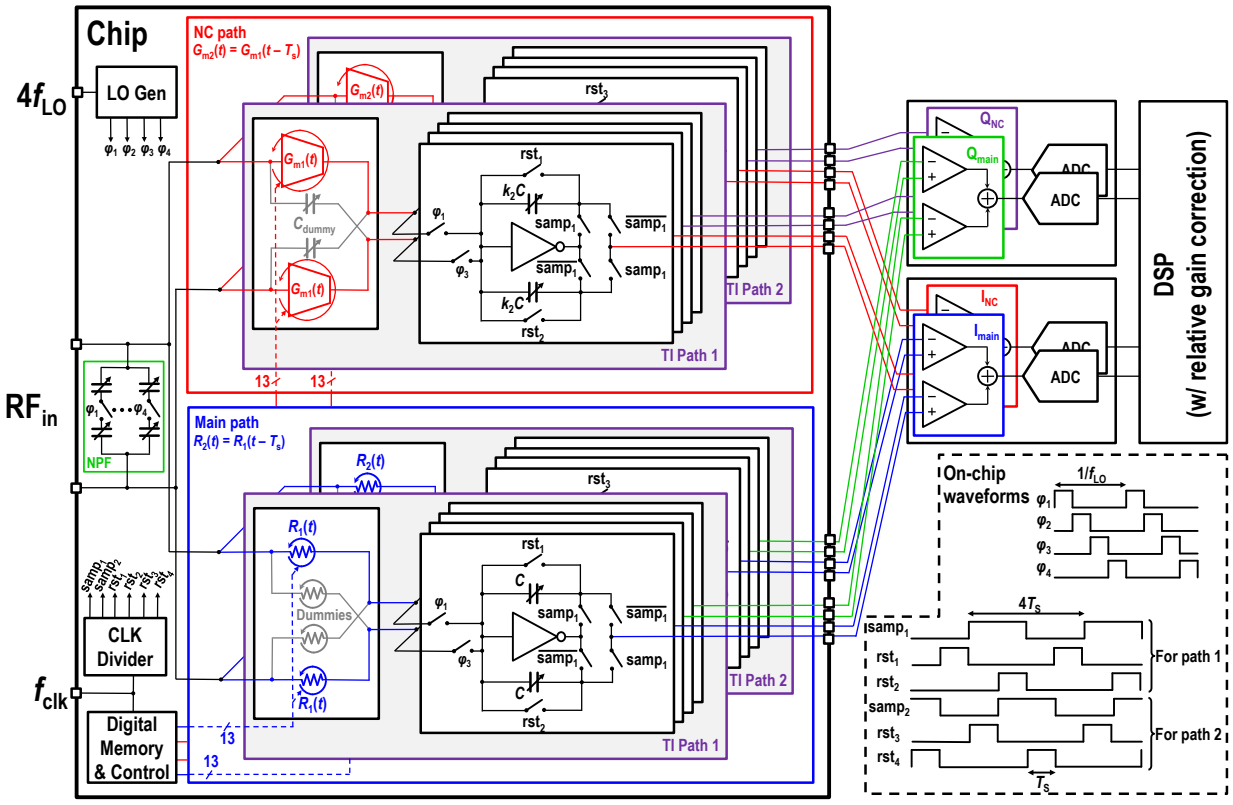

Figure 2.12: Complete block diagram of the implemented receiver front-end.

and the resistors are made of high-resistive polysilicon. Both are binary scaled in the RDACs. In this work, the linearity is primarily limited by the NC path. Therefore, in contrast to prior implementation of FA-based receivers where it is sized such that the resistance ratio between the transmission gate and the polysilicon resistor is 1:4, this work uses a ratio of 1:1, and minimum-sized (both width and length) transmission gates are used, lowering the parasitic capacitance due to the RDACs. The RDACs are designed to have a minimum resistance of 30 Ω. $G_{m1,2}(t)$ are formed by inverter-based G_m cells binarily turned ON/OFF by switches (G_mDACs), shown in Fig. 2.13(b), which is similar to that in [33], albeit being a higher-power one. Switches in the G_mDACs act as source-degeneration resistors to the G_m cells and are therefore designed to contribute less than 10% of the effective g_m in each cell for noise consideration. Non-minimum-length devices are used in the G_m cells (one unit cell has an equivalent W/L of 140 nm/55 nm) for lower γ and higher output resistance at the cost of more degradation on both S_{11} and NF at high frequencies. The finite output resistances of

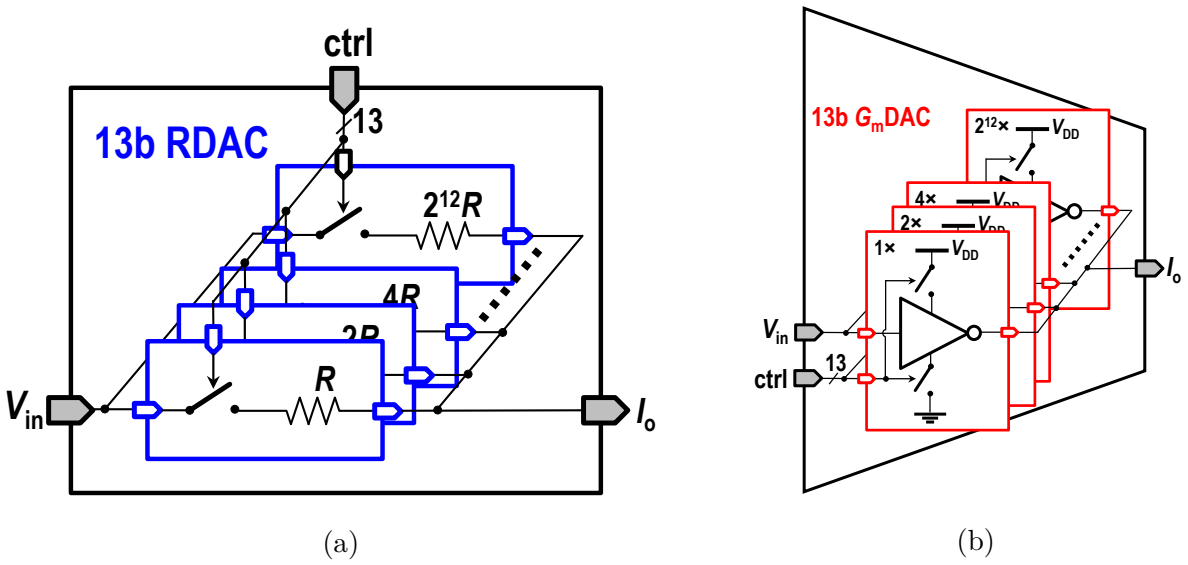

(a) (b)

Figure 2.13: Realization of (a) RDAC and (b) G_{m}DAC.

the G_{m} cells degrade the NF slightly and would be more if minimum-length devices are used. The linearity is primarily limited by the G_{m} cells, and no special techniques were employed to reduce the nonlinearity of the G_{m} cells except to keep both the baseband input impedance and the mixer switch resistance small in order to reduce the effects from g_{ds} non-linearity, similar to [10]. The RDACs and G_{m}DACs all vary at the rate of a clock frequency, f_{clk}, which is also used to generate all sampling and reset control clocks.

The bias of the entire chain is set to about half of the supply voltage, V_{DD}, by resetting baseband amplifiers, which also defines the voltages at the input and the output of the G_{m}DACs via the main and NC paths, respectively. No dedicated biasing circuitry is used. These baseband amplifiers are sized to have 125-mS g_{m} and 35-dB dc gain each with ping-pong capacitor banks around them for sampling. Similar to [18] and [19], the baseband amplifier's g_{m} is in fact part of $R(t)$ and is thus made large. The baseband integrator capacitors are tunable from 10 to 70 pF in the main path and 50 to 350 pF in the NC path.

Switches in the 4-path mixer and NPF are sized for ON-resistances of 2.5 and 5 Ω, respectively. Here, for having better linearity on the NPF and reducing the effective switch resistance, the bottom-plate mixing version of NPF [30] is used in both simulations and implementation of this work at the cost of higher input parasitic capacitance. The effective

switch resistance of the NPF is therefore 2.5 Ω by design. Since both the G_m cells and the NPF add additional capacitance to the input node that limits S_{11} at high carrier frequencies, whereas the former is also observed in the LTI-NC case, the top-plate mixing NPF may be used instead to improve high-frequency performance but worsens the OOB IIP_3 by a couple dBm according to simulations. Nevertheless, it still resolves the OOB DR and linearity issue. Note that in this work, the mixer switches in the main path are large to accommodate the variation of $R(t)$, while in LTI-NC, since the noise from these mixers are canceled, they can be much smaller to save LO power. The NPF and the mixers are driven by the same set of 25% duty-cycle clocks at f_{LO}.

2.5 Measurement Results

The implemented test chip was fabricated in a 28-nm CMOS process. Fig. 2.14 shows the die photo of the chip. The active area is 3.75 mm^2, 90% of which is occupied by baseband capacitors. Note the capacitor area can be significantly reduced when designed for operations with only higher RF bandwidths. The supply voltage of the whole chip is 0.9 V. At f_{LO} = 500 MHz, the entire chip consumes 61-mW power. Each baseband amplifier consumes about 2.7 mA, the LO divider and switch drivers consume about 16 mA, in which the NPF drivers consume about 1 mA, and the digital control circuitry dissipates 5.2 mA at a nominal f_{clk} of 1 GHz. It has been verified to work with an f_{clk} up to 2 GHz. On average, each G_mDAC consumes roughly 2-mA current. The power increases with f_{LO} due to LO divider and switch drivers being more power-hungry at higher frequencies. The sampled outputs are buffered externally, converted to digital signals by off-chip ADCs, and then processed digitally for signal summation and subtraction, with relative gain correction similar to that in [34]. The filter responses are generated by providing tonal inputs and then measuring the downconverted and aliased signals at baseband after sampling, similar to other FA works [17]–[19] (see Section V of [17] for more details). The RDACs and G_mDACs are dc calibrated at startup [9].

Figs. 2.15(a) and 2.15(b) show the measured in-band NF at 500-MHz f_{LO} and the

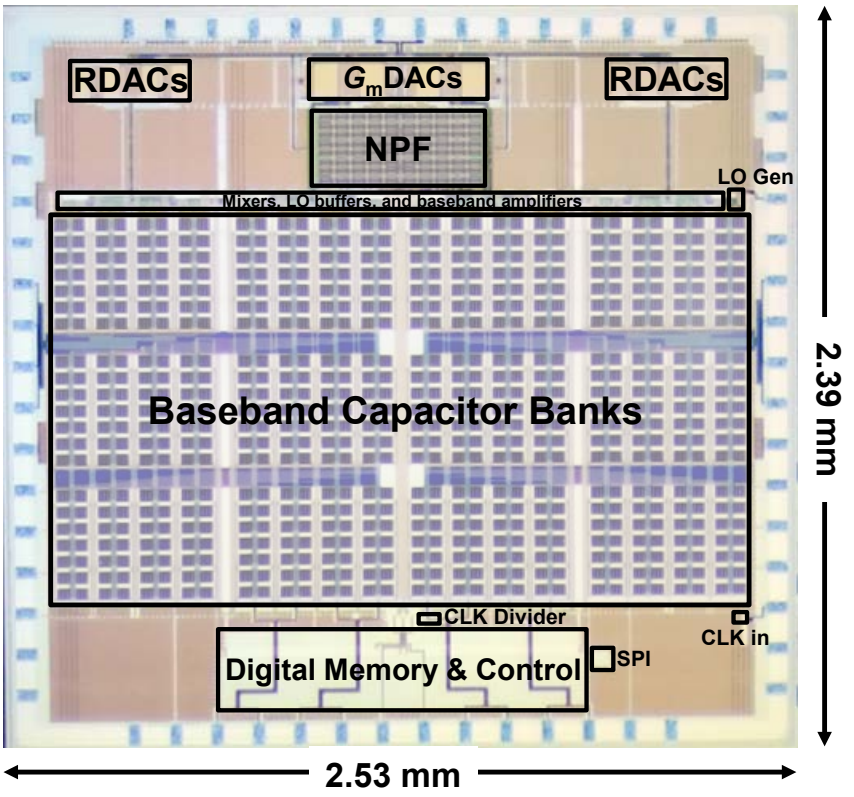

Figure 2.14: Chip micrograph.

measured NF with and without NC at different LO frequencies, respectively. With both NPF and NC, the $\mathrm{NF}_{\mathrm{min,IB}}$ is 3.2 dB and the averaged NF over [0, $f_s/2$), $\mathrm{NF}_{\mathrm{avg,IB}}$, is 4.2 dB. The increase of in-band NF at higher offset frequencies is due to filter droop, as seen in Fig. 2.11. It is also observed that the NPF does have minimal impact on the NF. Without the NPF, $\mathrm{NF}_{\mathrm{avg,IB}}$ is about 0.15 dB better. In contrast, both $\mathrm{NF}_{\mathrm{min,IB}}$ and $\mathrm{NF}_{\mathrm{avg,IB}}$ are about 3-dB worse without NC.

The measured A_{stop} for the overall filter is greater than 67 dB for a transition bandwidth of 40 MHz with a gain of ∼30 dB, as shown in Fig. 2.16(a) for 10-MHz RF BW. The achieved A_{stop} and transition BW are similar to [19] with 46- and 58-dB rejection at 22- and 30-MHz offset (using the same 67-dB A_{stop} configuration). This indicates that filter performance is preserved well with PTV-NC and NPF. The filter can be programmed to have 5–40-MHz RF BW, shown in Fig. 2.16(b). Fig. 2.16(c) shows the filter responses with f_{LO} varied from 100 MHz to 1 GHz.

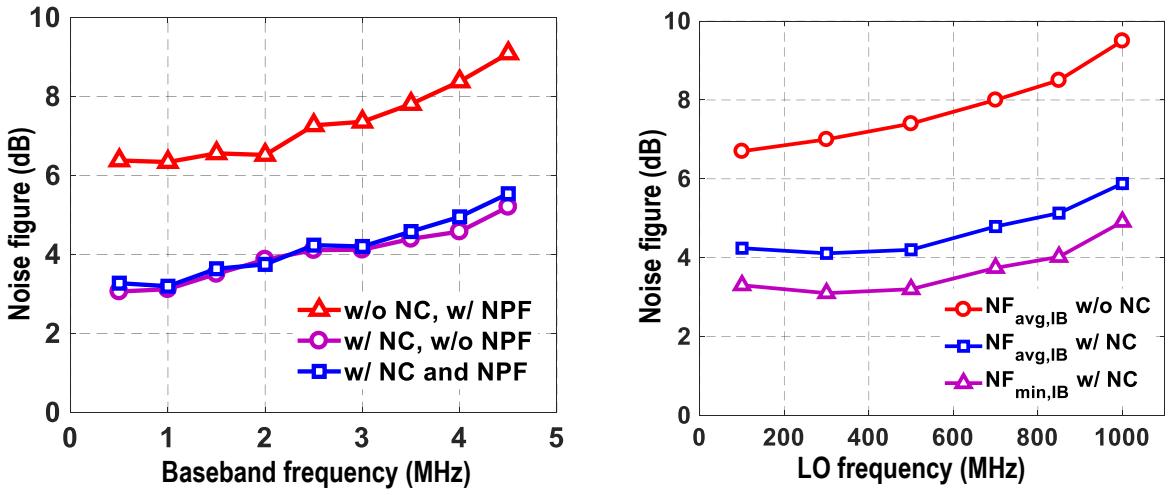

(a) (b)

Figure 2.15: (a) Measured in-band NFs with and without NC with f_{LO} = 500 MHz and RF bandwidth = 10 MHz (5-MHz baseband bandwidth), and (b) NF across different LO frequencies.

The linearity performance, i.e., $\mathrm{B_{1dB}}$ and $\mathrm{IIP_3}$, against different frequency offset and f_{LO} of the receiver in the 10-MHz RF BW configuration is depicted in Fig. 2.17. An OOB $\mathrm{IIP_3}$ of +18 dBm and an OOB $\mathrm{B_{1dB}}$ of +9 dBm are achieved even with upfront G_{m}DACs and a 0.9-V supply thanks to the NPF. Without the NPF, both OOB $\mathrm{B_{1dB}}$ and $\mathrm{IIP_3}$ evidently degrade by about 9 dB. The measured $\mathrm{S_{11}}$ and blocker NF are given in Fig. 2.18. The $\mathrm{NF_{avg,IB}}$ is 12 dB with a 0-dBm continuous-wave (CW) blocker placed at 30-MHz offset. It is primarily limited by the phase noise of the LO divider, which has a simulated phase noise of −164 dBc/Hz at 30-MHz offset. Better blocker NF should be achievable by burning more power in the LO divider.

Fig. 2.19 shows the measured LO leakage power and worst-case image filter (normalized to the peak of the corresponding desired filter frequency responses) at different LO frequencies. Due to the N-path operation of the NPF and the mixers plus the lack of an isolating LNA after the antenna, the LO leakage power is about −65 to −70 dBm, which is similar to other N-path-based or mixer-first architectures [35]. The image filter is caused by the

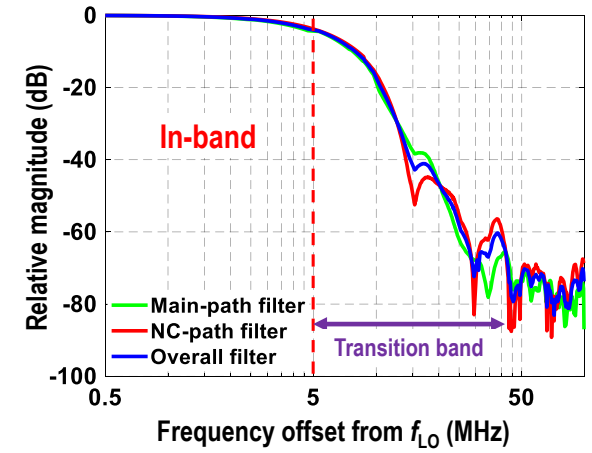

(a)

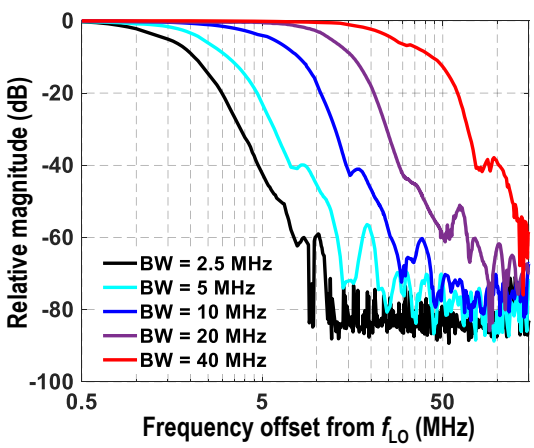

(b)

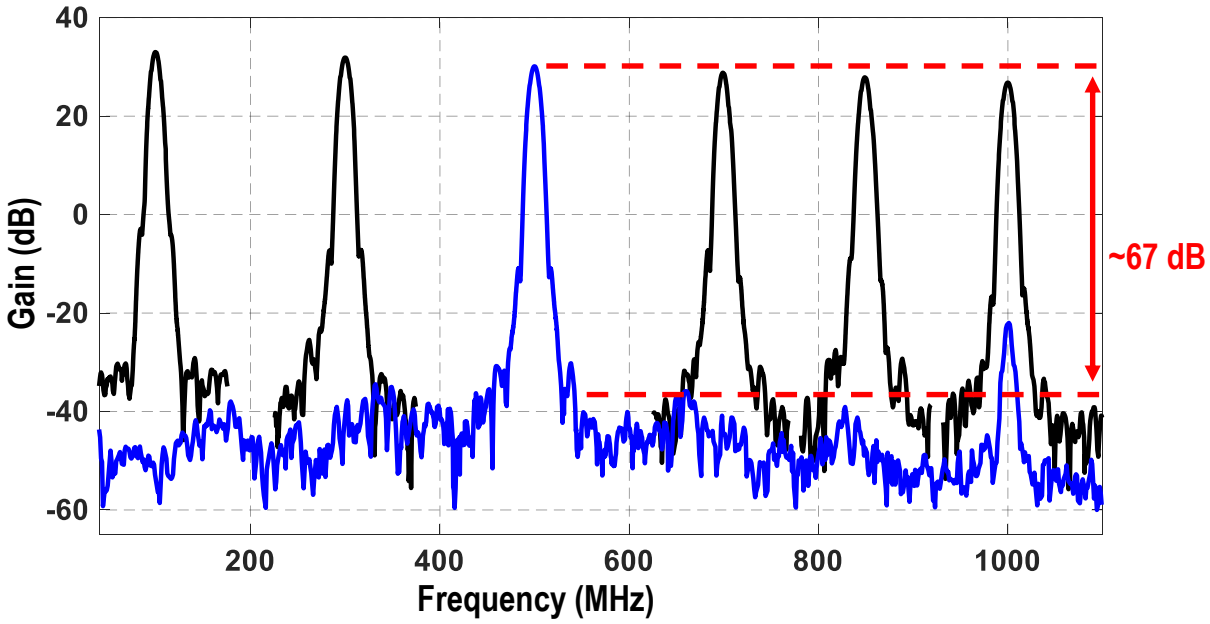

(c)

Figure 2.16: (a) Measured 10-MHz RF bandwidth filter responses, (b) filter responses with bandwidth tuned from 2.5–40 MHz, and (c) filter responses for LO frequency varied from 0.1–1 GHz.

TI path mismatches and degrades at higher LO frequencies due to LO clock skews [19]. The worst-case image rejection is better than 30 dB, sufficient for the requirements on the signal-to-noise ratio (SNR) for most applications. Other than filter shapes, other metrics do

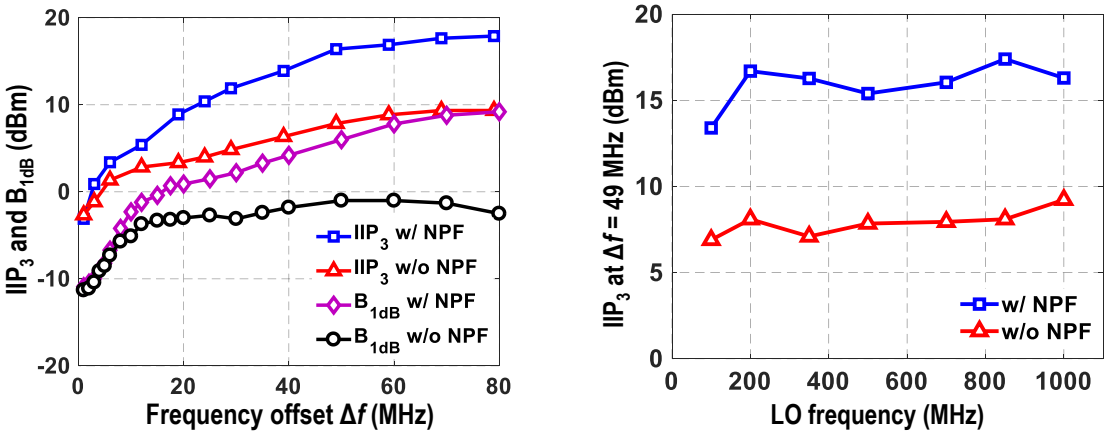

(a) (b)

Figure 2.17: (a) Measured $\mathrm{IIP_3}$ and $\mathrm{B_{1dB}}$ with and without NPF for $f_{\mathrm{LO}} = 500$ MHz, and (b) OOB $\mathrm{IIP_3}$ at 49-MHz offset for different LO frequencies.

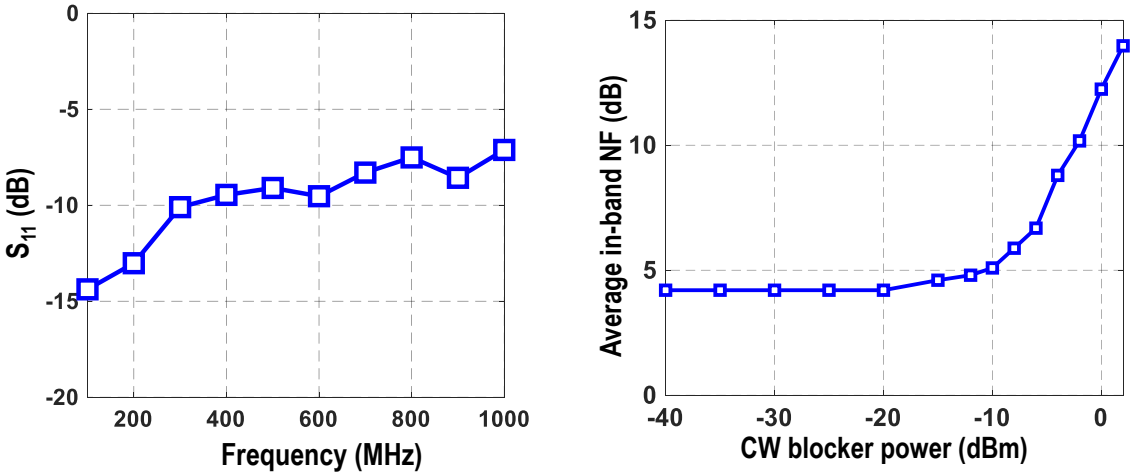

(a) (b)

Figure 2.18: (a) Measured $\mathrm{S_{11}}$, and (b) blocker NF in the presence of a CW blocker at $\Delta f = 30$ MHz with $f_{\mathrm{LO}} = 500$ MHz.

not vary appreciably for different configurations.

Table 2.1 compares this work with the state-of-the-art. While it maintains very sharp filtering with narrow transition band and high A_{stop} of FA [19], the NF compares more favorably against other works compared to [19]. Good OOB linearity is demonstrated with a

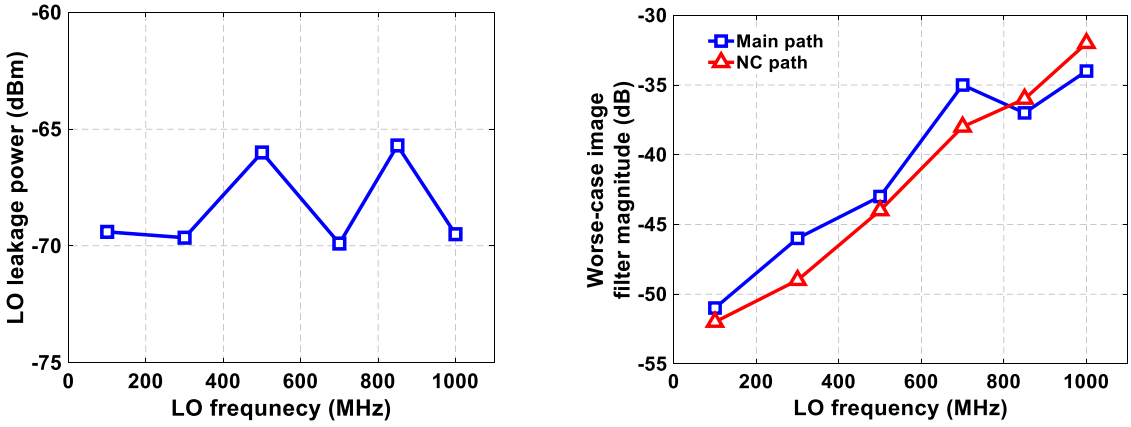

(a) (b)

Figure 2.19: (a) Measured LO leakage power, and (b) worst-case image filter magnitude at different LO frequencies.

0.9-V supply while all other works use higher supply voltages, mostly in the range of 1.2–1.6 V. Since this work relies on NPF to improve the linearity rather than linear resistors, close-in linearity is worse than [19]. It may be noted that unlike traditional architectures [10], [30], [36]–[38], where further filtering can be done on adjacent channels, the FA system as presented here allows folding of transition band signals into passband without full suppression, which is detrimental in a congested spectrum. To prevent such folding, the FA filter can be designed to have a lower BW while maintaining the sampling rate to ensure that the passband is free of folding artifacts, but this places an upper limit on the allowable transition bandwidth (and hence A_{stop}). To increase the allowable transition bandwidth and therefore higher rejection while maintaining signal bandwidth, the effective output sampling rate needs to be increased. This generally requires more time-interleaving to obtain some over-sampling ratio (OSR) for post-processing.

Although by exploiting PTV noise cancellation, the noise figure of the FA receiver can be lowered by ∼3 dB, it is worth noting that in addition to the linearity penalty due to the presence of active devices at RF and power penalty due to the extra auxiliary path, the area is increased by a large scale as well. Fundamentally, this is because, unlike mixer-first receivers, which use resistors in the feedback network of the baseband amplifiers to define

Table 2.1: Performance Summary and Comparison with the State-of-the-Art

	[10] JSSC'12	[14] JSSC'16	[19] JSSC'18	[30] JSSC'19	[36] JSSC'19	[37] JSSC'18	[38] JSSC'20	**This work**
Architecture	FTNC	*N*-path + DT filtering	TI-FA	*N*-path	*N*-path	*N*-path	*N*-path	**TI-FA + PTV-NC + *N*-path**
Technology	40 nm	65 nm	65 nm	28 nm	65 nm	45 nm SOI	28 nm	**28 nm**
RF frequency (GHz)	0.08–2.7	0.1–0.7	0.1–1	0.1–2	0.8–1.1	0.2–8	0.2–2	**0.1–1**
RF input	Single-ended	Differential	Differential	Differential	Differential	Differential	Single-ended	**Differential**
Bandwidth† (MHz)	4	6.4–9.6	2.5–40	13	30–50	20	18	**2.5–40**
A_{stop} (transition BW)	N/A	>70 dB (8.5× BW)	>45 dB (1.7× BW) >70 dB (4× BW)	>47* dB (6× BW)	>15* dB (0.5× BW)	>25 dB (4.5× BW)	~28* dB (2.8× BW)	**>46 dB (1.7× BW) >67 dB (4× BW)**
$NF_{min,IB}$ (dB)	1.9	6.8–9.7#	6# @ 0.5 GHz	4.1–10.3#	5.0–8.6#	2.3–7.2*#	4.3–7.6	**3.1–4.9#**
$NF_{avg,IB}$ (dB)	N/A	N/A	6.5–8.5#	N/A	~7.6–9*#	N/A	N/A	**4.1–5.8#**
OOB IIP_3 (dBm)	+13.5 (20× BW)	+24 (4.7× BW)	+24 (4× BW)	+44 (12.3× BW)	+24 (1× BW)	+39 (4× BW)	+33 (4.4× BW)	**+18 (8× BW)**
OOB B_{1dB} (dBm)	−2 (20× BW)	+14.7 (4.7× BW)	+13 (4× BW)	+13 (12.3× BW)	+9 (1× BW)	+12 (4× BW)	+12 (3.3× BW)	**+9 (8× BW)**
OOB IIP_2 (dBm)	+55	N/A	+64	+90	+61	+88	N/A	**+65**
Gain (dB)	72	40	23	16	−5*	21	13	**30**
Supply voltage (V)	1.3	1.2/1.6	1.2/1	1.2/1.0	1	1.2/1	1.2	**0.9**
Power (mW)	35–78	59–105	75–99	38–96	80–97	56–290	146.6–179	**48–74**
Area (mm^2)	1.2	1.2	2.3	0.49	1.9	0.8	0.48	**3.75**

*Estimated from figures #Excludes balun loss †RF bandwidth

the receiver voltage gain, FA receivers' gain is defined by the integrating capacitor, C and $R(t)$. As a consequence of required matching and filtering shape, the values of $R(t)$ generally cannot be used to defined the gain, hence C is the primary parameter to control the gain. As a result of requiring $k_1 \approx k_2$ and large k_1 to suppress G_{m} cells' noises, large k_2 is needed, leading to large capacitors used in the auxiliary path, which is $5\times$ that in the main path. Due to the large capacitors used in FA receivers, the area penalty is also relatively large. In the case where N is chosen to be 8 rather than 4 to further lower the harmonic folding noise contribution, the overall area of the receiver will become even larger since that will require twice as many baseband devices. This is rather unique to noise cancellation for FA receivers.

CHAPTER 3

A Dual-Channel High-Linearity Filtering-by-Aliasing Receiver Front-End Supporting Carrier Aggregation

3.1 Introduction

So far we have been discussing single-channel receiver front-ends, which are already facing many obstacles for being practically used in a software-defined radio. Due to the demand for high data throughput and the scarcity of wide contiguous spectral bands in the sub-6-GHz spectrum, programmable receivers that can support carrier aggregation (CA) are also highly demanded and face their own challenges. Unfortunately, conventional N-path mixer-first approaches cannot be readily extended to support CA. This is because, while a single-channel N-path structure presents 50-Ω input impedance at the carrier frequency to achieve impedance matching, it presents low impedance at other non-harmonic frequencies. When two or more mixer-first receivers with different LO frequencies are connected in parallel, the resultant input impedance is always low across all frequencies. It thus cannot be used to receive more than one channel concurrently. Several techniques have been proposed to overcome this problem [20], [24], [39], [40], however, almost all of them require a low-noise amplifier (LNA) at RF, which limits the linearity [typically <10-dBm OOB IIP_3 and <0-dBm blocker 1-dB compression point (B_{1dB})]. Even the purely mixer-first one [40], albeit using modulated clocks, still demonstrates only ∼15-dBm OOB IIP_3 and ∼5-dBm B_{1dB}, which is lower than what a single-channel mixer-first receiver can achieve (typically >20-dBm OOB IIP_3 and ∼10-dBm B_{1dB}).

Furthermore, even though some mixer-first receivers have shown excellent linearity, such as [30], which reported an OOB IIP_3 as high as +44 dBm, most of them typically employ

1.2-V or higher supply voltages to improve linearity even in advanced nodes such as 28-nm CMOS, where the core voltage is only 0.9 V. Their LO leakage power is generally larger than -70 dBm, not compliant with the Federal Communications Commission (FCC) requirement [35].

On the other hand, in Chapter 2, we have introduced PTV noise cancellation to lower the noise of an FA receiver, it only demonstrated moderate linearity, which is not only about 20 dB lower in terms of OOB IIP_3 than the highest reported number, but insufficient in some scenarios like frequency division duplex (FDD), hence having limited overall dynamic range. Moreover, as can be seen from Subsection 1.2.3 (and Fig. 23 in [18]), FA receivers do not work well with non-resistive source impedances: unintended bumps may show up in the transition band when the source is not purely resistive and the transition bandwidth could suffer. It does not support carrier aggregation, either. Methods to further enhance the dynamic range and improve other metrics are needed. In this Chapter, we show the concept of a slice-based FA architecture [41], [42] that helps overcome some of prior FA receivers' problems. Section 3.2 details the problems of conventional FA receiver designs. Section 3.3 explains the proposed slice-based architecture in detail and shows how it resolves some of these problems. Section 3.4 describes the dual-channel implementation with the proposed FA architecture. Detailed circuit implementation is presented in Section 3.5, followed by measurement results in Section 3.6.

3.2 Limitations of Prior FA Receivers

3.2.1 FA Receiver in the Presence of RF-Node Reactance

Consider again the representative FA receiver shown in Fig. 3.1(a), where Z_{p} represents the reactive part of the antenna impedance and inevitable parasitics due to the board, bond pads, bond wires, etc. With a purely resistive source impedance, R_{s}, the FA filter's impulse response, $g(\tau)$, is given by (2.1). However, with Z_{p}, (2.1) is no longer accurate. Intuitively, at different frequencies, Z_{p} will siphon away different amounts of current from the time-

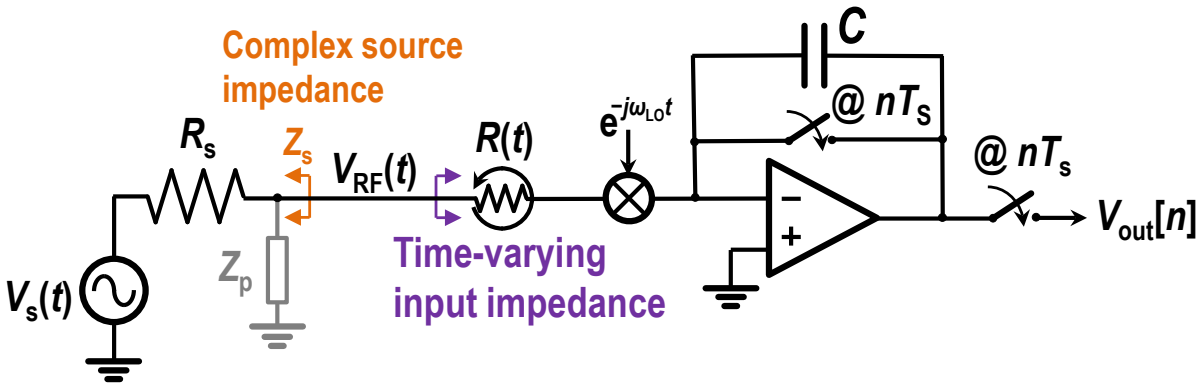

(a)

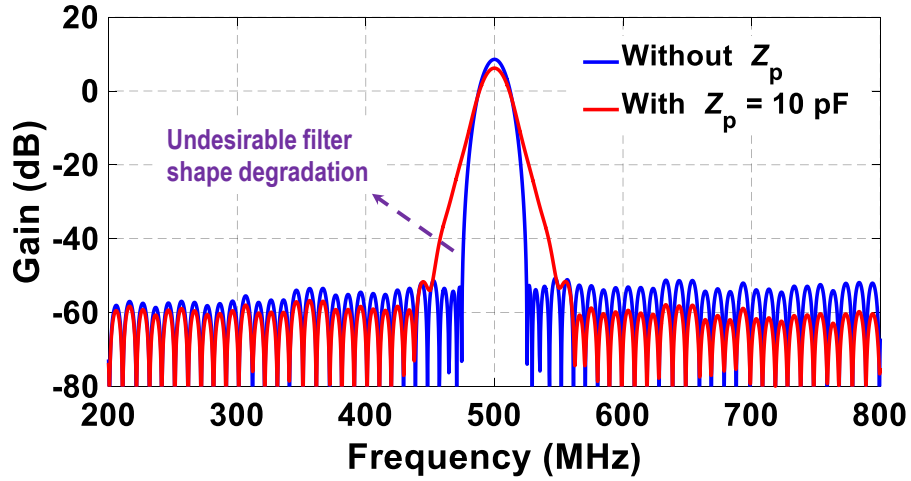

(b)

Figure 3.1: (a) Prior FA receiver front-end with a sampling period of T_s in the presence of Z_p, and (b) effect of Z_p on the attainable filter.

varying $R(t)$, leading to a distorted $g(\tau)$ and hence filter degradation. Fig. 3.1(b) illustrates the effect by plotting the simulated filter magnitude responses, $|G(j\omega)|$, where $G(j\omega)$ is the Fourier transform of $g(\tau)$, without Z_p and with $Z_p = 10$ pF for an example band-pass filter centered at 500 MHz (with $C = 100$ pF, amplifier gain $= 40$ dB, $f_{LO} = 500$ MHz, and $T_s = 100$ ns). As is apparent, the filter transition bandwidth has almost doubled. Similar phenomenon has been observed in Subsection 2.3.2, where the NPF's impedance leads to undesirable FA filter degradation. With Z_p more complicated than a simple capacitor, the filter shape degradation might be worse. Furthermore, since the knowledge of Z_p is imprecise

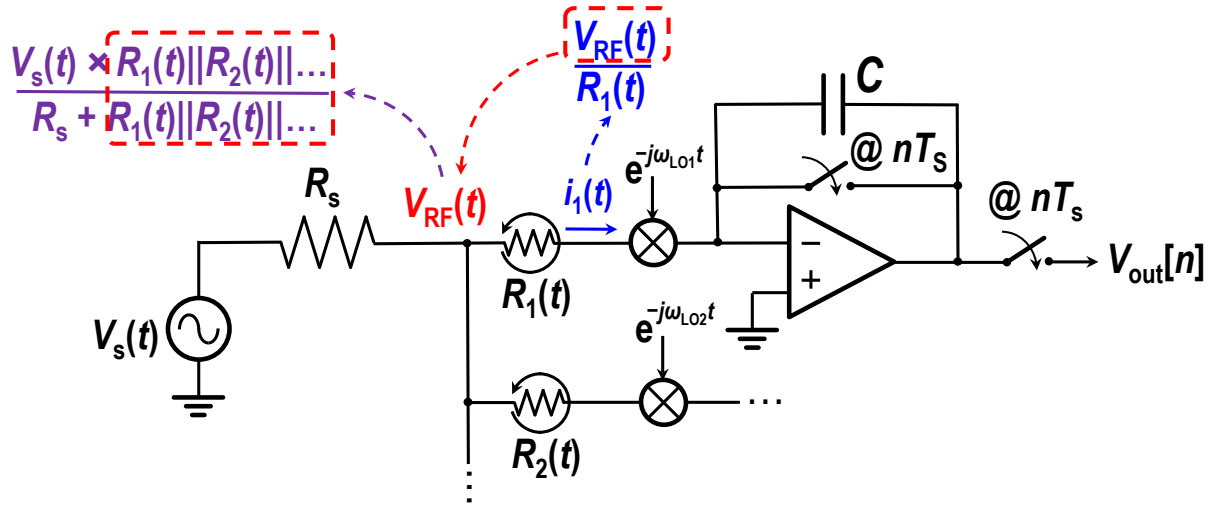

Figure 3.2: Prior FA receiver front-ends in parallel for multi-channel operation.

(because it is a real-world reactance) and Z_p may vary substantially over time (as is common with many antennas), its effect on the filtering can be unpredictable.

3.2.2 Problems with Multi-Channel Operation

Fig. 3.2 shows a naïve extension of the FA receiver concept to multi-channel operation, where $R_i(t)$ is the time-varying resistor in the ith channel. Even ignoring any input reactance, it is apparent that the current flowing into any one channel depends on the $R_i(t)$s of all the channels. This may lead to corruption of each channel's filter shapes. In principle, careful co-design of the $R_i(t)$s can recover the filter shapes but can be challenging in practice owing to mismatches and timing errors in realizing precise $R_i(t)$s.

3.2.3 Linearity Issues

FA receivers demonstrated better close-in linearity than much of the other prior art [19], which is because FA filters do not use a feedback resistor to define the gain, but the capacitance C, whereas the bandwidth is set by T_s. This decouples FA filter's gain and bandwidth, and typically the required C for a 10-MHz BW FA filter with 10–20-dB gain is large. Therefore, the close-in linearity is better. However, the linearity needs to be further improved,

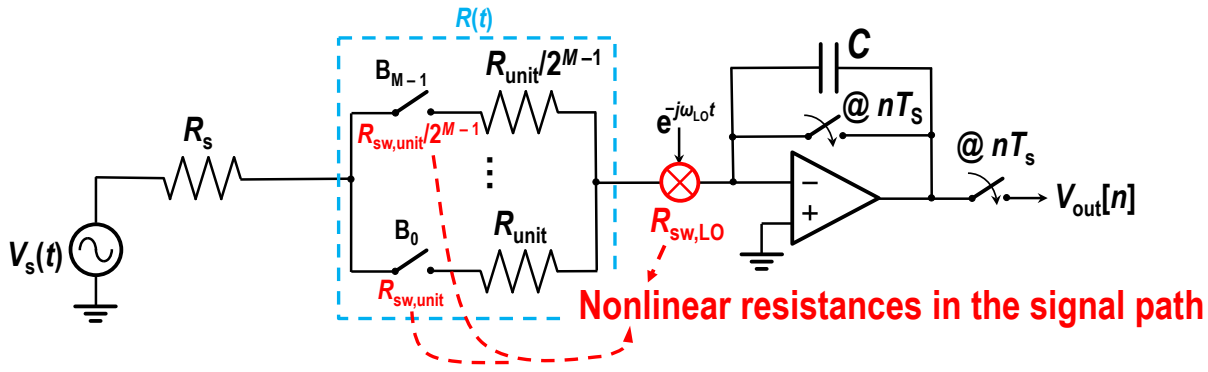

Figure 3.3: Linearity limitation of the prior implementation of FA receivers due to nonlinear switches in the signal path.

especially at high offset frequencies. Consider the implementation of the PTV resistor using a resistor DAC (RDAC) [17]–[19], [27], [28] as shown in Fig. 3.3. A bank of resistors is placed in series with transmission gate switches controlled by a digital control code (B_0, B_1, …, B_{M-1}). A small ratio of switch ON resistance to the physical resistor reduces signal swings across the switch transistors, resulting in reasonably high linearity. In [17] and [19], about +25- and +33-dBm OOB IIP_3 was achieved with $R_{\text{sw,unit}} : R_{\text{unit}} = 1{:}4$ and 1:10, respectively (both at 1.2-V supply). Reducing the ratio further is impractical since the large transistors introduce too much parasitic capacitance with attendant degradations of filter shape, S_{11}, etc. As such, the switch transistors present directly in the signal path can limit the linearity of the overall receiver. Mixer switches also contribute their own nonlinear currents but are less of a problem. Similarly, baseband amplifiers also contribute their own nonlinearity, which is also less significant than that from the RDAC at this level of linearity performance.

3.2.4 Residual Aliases

Since FA combines filtering and sampling into a single structure, any undesirable signals that are insufficiently filtered can alias back onto the desired signal. This is unlike in the mixer-first approaches where subsequent stages can provide additional filtering. Even with up to 70-dB A_{stop} reported by time-interleaved FA [19], residual aliases from very strong blockers

pose a fundamental challenge to FA receivers. This remains unsolved in this Chapter, but Chapter 4 provides an alias cancellation technique for FA receivers that helps resolve this problem to some extent.

3.2.5 Noise

The noise performance of FA receivers is generally slightly worse than the mixer-first ones, mainly because of the $R(t)$ variation and aliased noise from the source. In order to perform sharp filtering, the required $R(t)$ may be larger than 50 Ω for much of the period, T_s, leading to slightly more than 3-dB NF due to $R(t)$ alone. This part of noise can be improved by employing PTV noise cancellation techniques [27], [28], but at the expense of degraded linearity. In addition, since the FA filter, $g(\tau)$, is not an ideal brick-wall filter, source noise at frequencies outside the band folds in after sampling, albeit being attenuated. This generally adds another 1–2 dB to the average in-band NF, which is also inherent with FA.

3.3 Slice-Based FA Architecture

Instead of building the RDACs as in [17]–[19], [28], we propose a slice-based FA architecture [41], [42], where the DAC combines both the resistor and the baseband amplifiers, i.e., G_m cells, together in each slice, as illustrated in Fig. 3.4. No switches are present before the virtual ground created by the amplifiers in each slice, and all switches, including mixer switches, are moved into the feedback network. The switches are now, essentially, selection switches that either steer the current into the common integrating capacitor, C, or to the output of the G_m cells to form a unity-gain buffer, as illustrated, for a single slice, in Fig. 3.5. An M-bit *CtrlCode* determines which slices, out of the total M binarily scaled ones, steer the current to C with the rest forming unity-gain buffers. As described in detail later, periodically varying the *CtrlCode* in time realizes the desired FA operation with the attendant sharp filtering.

As described below, the slice-based structure offers three major advantages: a) constant input impedance while maintaining PTV operation, b) linearity improvement, and c) LO

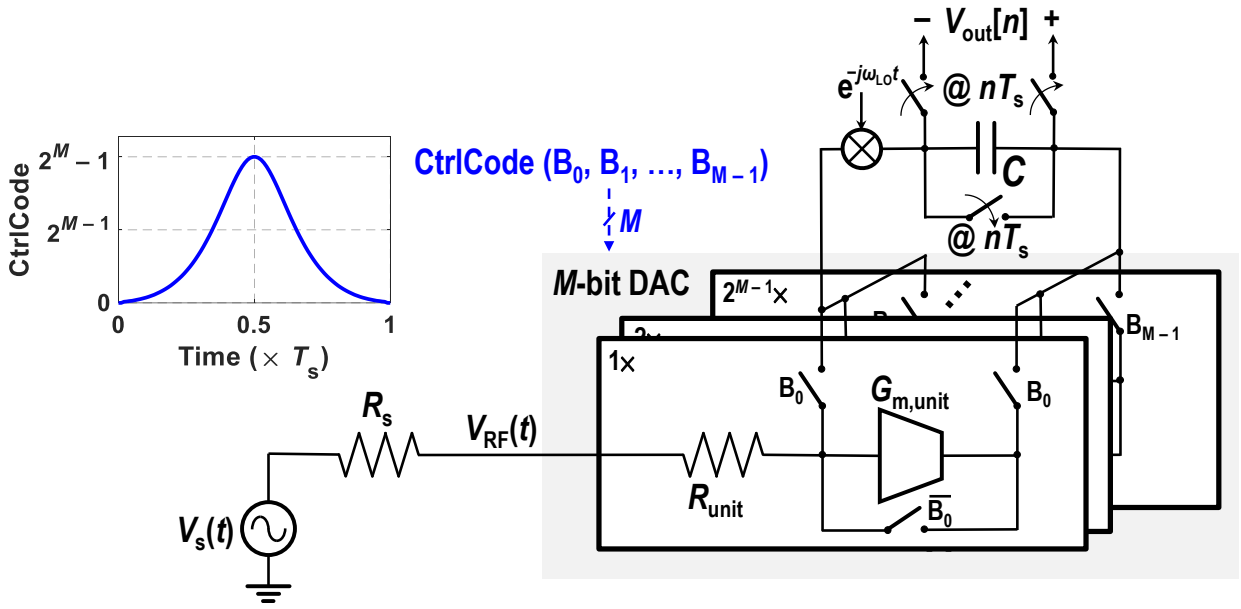

Figure 3.4: Proposed slice-based FA architecture, where the G_m cells are integrated with the resistor in each slice, and switches are all moved within the feedback network.

leakage suppression. The constant input impedance leads to easy multi-channel operation. A two-channel CA receiver implementation will be detailed in Section 3.4. In the following, we analyze how the proposed architecture offers these benefits and solve the aforementioned problems with FA receivers at the expense of worsened noise performance. It is important to note that residual aliases mentioned in Subsection 3.2.4 remain a problem, and this work does not improve the performance in this respect. For certain applications, the achieved stopband rejection of ∼50 dB of this work might still be a problem.

3.3.1 PTV Operation and Input Impedance

Consider again Fig. 3.5, which illustrates the operation of the kth slice that is controlled by bit B_{k-1} in the *CtrlCode*, in both ON and OFF states (for the proposed architecture, we call a slice ON if it steers current to C, and OFF if it does not). For simplicity, we assume here the G_m cell is ideal. The input impedance of the kth slice is independent of whether the control bit, B_{k-1}, is 1 or 0. In fact, nominally, it is only dependent on the resistor and the G_m, and is equal to $(R_{unit} + 1/G_{m,unit})/2^{k-1}$. This is because, regardless of the

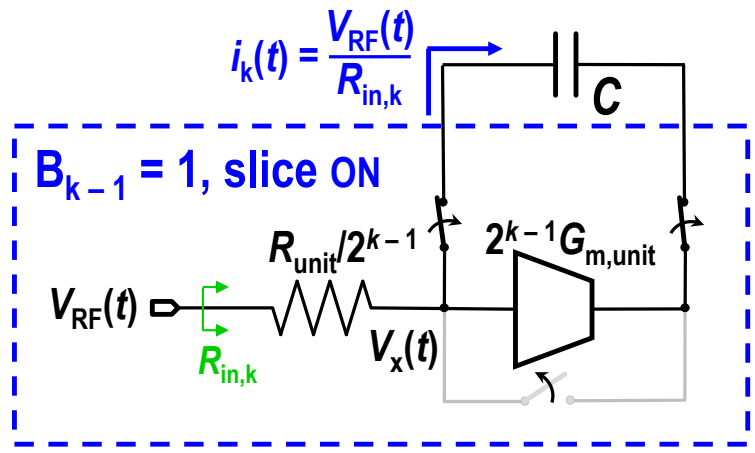

(a)

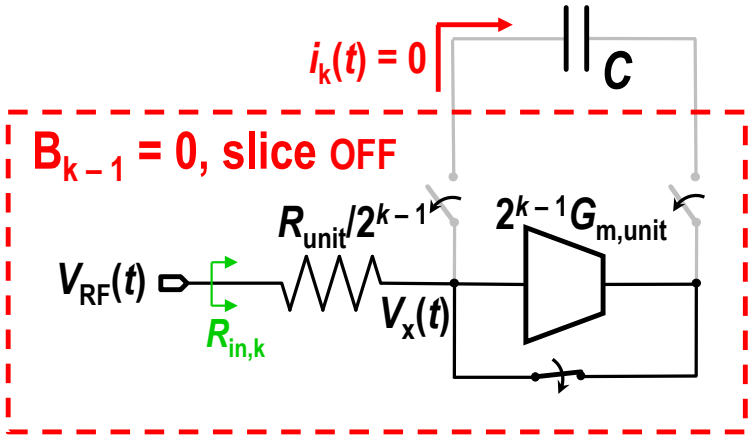

(b)

Figure 3.5: Operation using the kth slice as an example when (a) the slice is ON, and (b) the slice is OFF, where $R_{\mathrm{in,k}} = (R_{\mathrm{unit}} + 1/G_{\mathrm{m,unit}})/2^{k-1}$ to the first order.

status of the slice, the G_{m} cell is always in negative feedback. In practice, the finite output impedance of the G_{m} cell, has some small yet non-zero impact on the input impedance in the two states, but the effect is negligible as verified by simulations. Overall, independent of the *CtrlCode*'s value, the structure presents a constant, time-invariant input resistance of $R_{\mathrm{in}} = (R_{\mathrm{unit}} + 1/G_{\mathrm{m,unit}})/(2^{M-1})$, which can be matched to R_{s}. Since both R_{in} and R_{s} are linear time-invariant (LTI), the overall impedance at the RF node also remains LTI even in the presence of reactance due to the antenna or parasitics.

Now consider the amount of current steered to the capacitor. The current from the ON

kth slice to the capacitor is

$$i_{\mathrm{k}}(t) = \frac{V_{\mathrm{RF}}(t)}{R_{\mathrm{in,k}}} = \frac{2^{k-2}V_{\mathrm{s}}(t)}{R_{\mathrm{unit}} + 1/G_{\mathrm{unit}}}, \tag{3.1}$$

if the input of the receiver is matched to R_{s}. The current from the OFF kth slice to the capacitor, on the other hand, is zero. Therefore, the *CtrlCode* periodically changes the number of ON slices and hence the amount of current flowing into the capacitor over time. This enables the desired PTV operation just like the conventional FA filters.

The equivalent model of the proposed slice-based FA receiver is shown in Fig. 3.6(a). Essentially, at all times, t, the source is matched with an explicit resistor R_{in} that is time-invariant and $V_{\mathrm{RF}}(t)$ is nominally half of $V_{\mathrm{s}}(t)$. However, at time t, the ON slices, which account for an effective resistance of $R_{\mathrm{eff}}(t)$, steer the current to the capacitor, whereas the OFF slices form a shunt resistor at the RF node, $R_{\mathrm{shunt}}(t)$, such that $R_{\mathrm{eff}}(t)||R_{\mathrm{shunt}}(t) = R_{\mathrm{in}}$. Another way to look at how the time-invariant input impedance is realized is that the ON slices realize a resistor of $R_{\mathrm{eff}}(t)$, while the OFF slices create another resistor, $R_{\mathrm{shunt}}(t)$ in parallel with $R_{\mathrm{eff}}(t)$, and it follows that $R_{\mathrm{eff}}(t)||R_{\mathrm{shunt}}(t) = R_{\mathrm{s}}$ if they are designed to match the source. Effectively, $V_{\mathrm{RF}}(t)$ is processed by an equivalent FA filter with the PTV resistance, $R_{\mathrm{eff}}(t)$. Note that the FA filter impulse response is now $g(\tau) = 1/(2CR_{\mathrm{eff}}(-\tau))$. Recalling (2.1), we can see that $R_{\mathrm{eff}}(t)$ should be a scaled version of $(R_{\mathrm{s}} + R(t))$, in order to retain the same filter shape and achieve impedance matching. This is because, R_{in} is formed by $R_{\mathrm{eff}}(t)$ and $R_{\mathrm{shunt}}(t)$ in parallel, hence $R_{\mathrm{eff}}(t) \geq R_{\mathrm{in}}$. To match R_{in} and R_{s}, the minima that $R_{\mathrm{eff}}(t)$ can become is 50 Ω, whereas there is no such constraint in the prior FA approach [18]. Fig. 3.6(a) also shows an example of the $R(t)$ used in the FA receiver of Fig. 3.1 and the corresponding $R_{\mathrm{eff}}(t)$ needed in this work, to nominally realize the same FA filter shape. Note that the reactance at RF no longer sees any time-varying resistance on the FA side, and hence the effect of it is the same as the conventional LTI front-ends. A filter is still formed at the RF node due to Z_{p} and $R_{\mathrm{s}}||R_{\mathrm{in}} = R_{\mathrm{s}}/2$ if $R_{\mathrm{in}} = R_{\mathrm{s}}$. The PTV filter now simply acts on the LTI-filtered signal, $V_{\mathrm{RF}}(t)$, instead of the original signal $V_{\mathrm{s}}(t)$. Fig. 3.7 shows the filter shapes without Z_{p} and with $Z_{\mathrm{p}} = 10$ pF, i.e., the same condition as that in Fig. 3.1(b). Apparently, the filter transition bandwidth is intact, while the overall gain

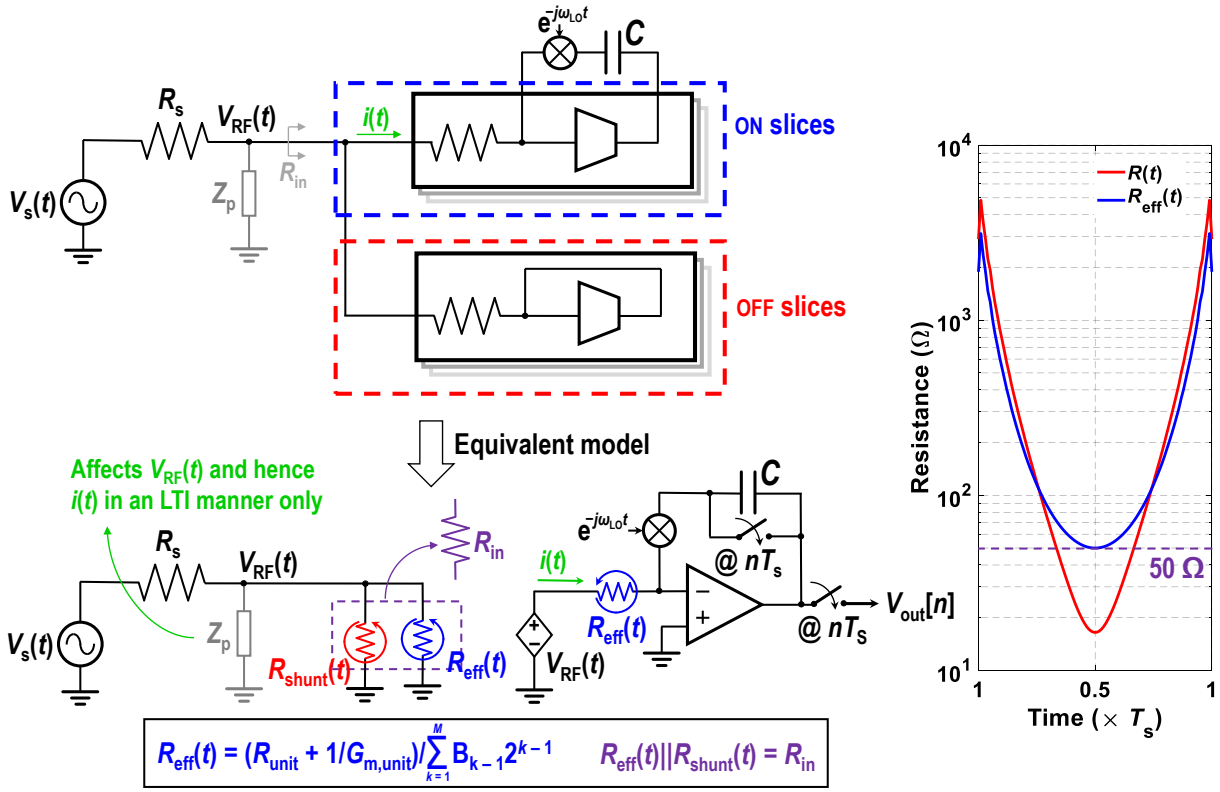

(a)

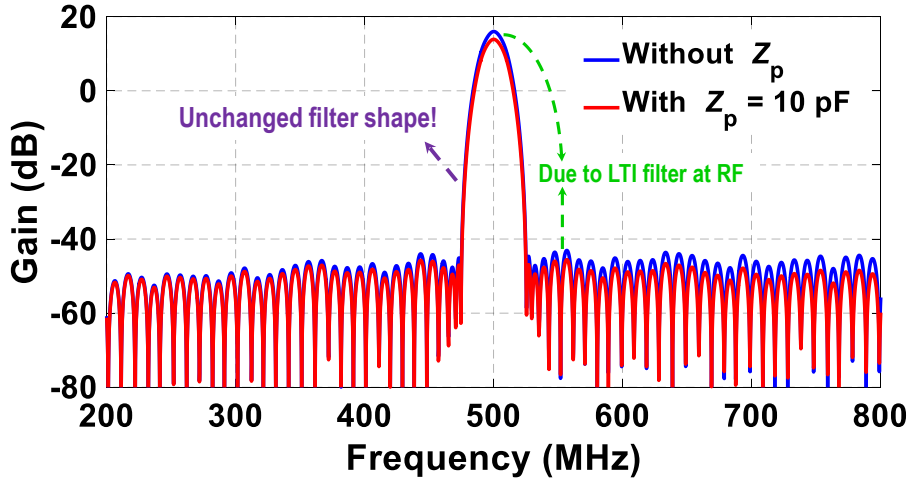

(b)

Figure 3.6: (a) Equivalent model of the proposed slice-based FA receiver with an example of $R_{\text{eff}}(t)$ and (b) effect of Z_{p} on the slice-based FA filter.

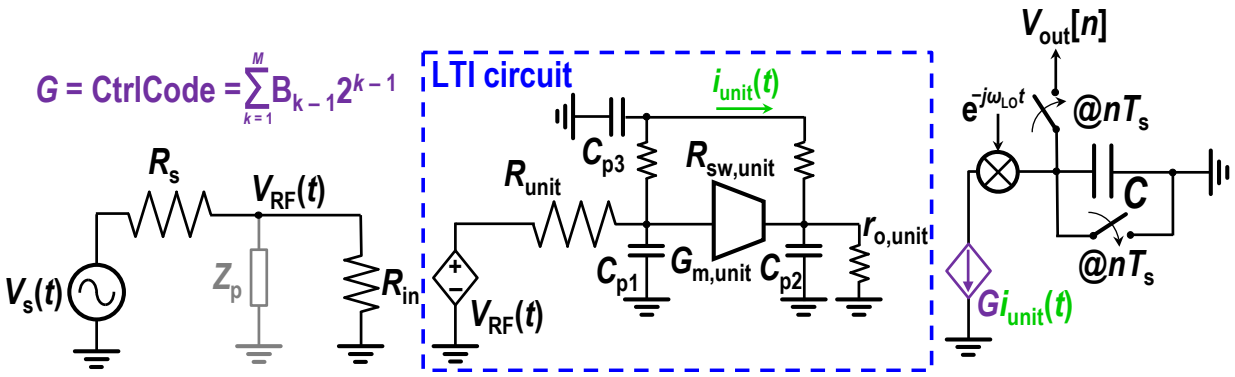

Figure 3.7: Alternative model of the proposed slice-based FA receiver for analyzing parasitics' effect on operation frequency.

is gradually decreasing slowly as frequency increases, due to the first-order RC filter at the RF node.

It is instructive to look at what limits the operational frequency of this architecture. The nature of the slice-based approach allows us to use simple LTI analysis to determine this. Consider a simplified model of the proposed FA receiver shown in Fig. 3.7, where the parasitics of the mixer and the integrating capacitor are ignored for simplicity, and the other circuit parasitics are lumped into $C_{\mathrm{p1\text{–}3}}$. Note the time-varying aspect is confined to $G = CtrlCode$, the mixer, and the sampler, while the rest of the front-end, which represents the core of each slice, is in fact an LTI circuit. Within the BW of this LTI circuit, $i_{\mathrm{unit}}(t)$ is proportional to $V_{\mathrm{s}}(t)$, and proper FA filtering can be achieved. Beyond the BW, $i_{\mathrm{unit}}(t)$ starts getting filtered, and FA filtering is degraded (although in reality, due to mismatches among slices, the ideally LTI circuit in Fig. 3.7 could still show certain PTV behavior, which causes extra filter degradations). In this work, large switches and unintended layout parasitics limit the BW, which is approximately estimated as $1/(r_{\mathrm{o,unit}} \sum_{i=1}^{3} C_{\mathrm{p}i})$ to the first order (here conservatively we consider the loop gain BW, since the loop gain is the key to many improvements achieved in this work), where $r_{\mathrm{o,unit}}$ is the output resistance of the unit G_{m} cell and $\sum_{i=1}^{3} C_{\mathrm{p}i} \approx 0.5$ fF per unit slice, to about 1.3 GHz, hence an operating frequency up to 1 GHz is chosen in this work. More advanced nodes and careful layout help improve this frequency.

3.3.2 Baseband Filter Noise Performance

Although the proposed slice-based architecture does provide tolerance to the reactance at the RF node due to its time-invariant input impedance, it comes with an NF penalty. This becomes apparent by input-referring the PTV resistor noise sources as shown in Fig. 3.8. Contrasting this with Fig. 3.1(a), it is easy to see that the NF of the proposed architecture will be worse than that in [18] because of two reasons. Firstly, the noise source due to $R_{\text{eff}}(t)$ is effectively amplified by $(R_{\text{shunt}}(t) + R_{\text{s}})/R_{\text{shunt}}(t)$, which is greater than unity. In other words, the smaller $R_{\text{shunt}}(t)$ is, i.e., as more slices are OFF (unused for signal conduction), the more noise results. Secondly, the OFF slices themselves, i.e., $R_{\text{shunt}}(t)$, introduce some extra, though small, noise.

Mathematically, the corresponding NF caused by the baseband slice-based FA filter can be found by following the calculation method given in Appendix A. Note since we have input-referred all noise sources, the transfer function that these sources see is identical. The baseband noise factor is

$$F_{\text{baseband}} = 1 + \frac{\int_{t=0}^{T_{\text{s}}} dt/R_{\text{eff}}(t)}{R_{\text{s}} \int_{t=0}^{T_{\text{s}}} dt/R_{\text{eff}}^2(t)} + \left(2R_{\text{s}} + \frac{R_{\text{s}}^2}{R_{\text{in}}}\right) \frac{\int_{t=0}^{T_{\text{s}}} dt/[R_{\text{shunt}}(t)R_{\text{eff}}(t)]}{R_{\text{s}} \int_{t=0}^{T_{\text{s}}} dt/R_{\text{eff}}^2(t)}. \tag{3.2}$$

Here the excess noise factor $\gamma = 1$ is assumed. If $R_{\text{eff}}(t) = R_{\text{s}}$ and $R_{\text{shunt}}(t)$ is infinity, then $\text{NF}_{\text{baseband}} = 3$ dB, as expected for an LTI system. The switches' noise contributions are negligible. They degrade the total NF by less than 0.1 dB according to simulation and are hence omitted in our discussions. Comparing (3.2) with (13) in [18], we see that F_{baseband} of slice-based FA is larger than conventional FA because different $R_{\text{eff}}(t)$ is used, and an extra term, the last one, is introduced in (3.2) that further deteriorates the noise performance. The calculated $\text{NF}_{\text{baseband}} = 5.2$ dB, which is flat across the band, unlike that in Chapter 2. This is about 2 dB higher than that in [18], as expected. The contribution from the noise of $V_{\text{nRshunt}}(t)$ is small, about 0.3 dB only. A loose bound on the baseband NF can be found, since $R_{\text{shunt}}(t)_{\text{MIN}}$ is bounded to R_{s}, given by

$$F_{\text{baseband}} \leq 1 + \left[1 + 2\frac{R_{\text{s}}}{R_{\text{shunt}}(t)_{\text{MIN}}}\left(1 + \frac{R_{\text{s}}}{2R_{\text{in}}}\right)\right] \frac{\int_{t=0}^{T_{\text{s}}} dt/R_{\text{eff}}(t)}{R_{\text{s}} \int_{t=0}^{T_{\text{s}}} dt/R_{\text{eff}}^2(t)}. \tag{3.3}$$

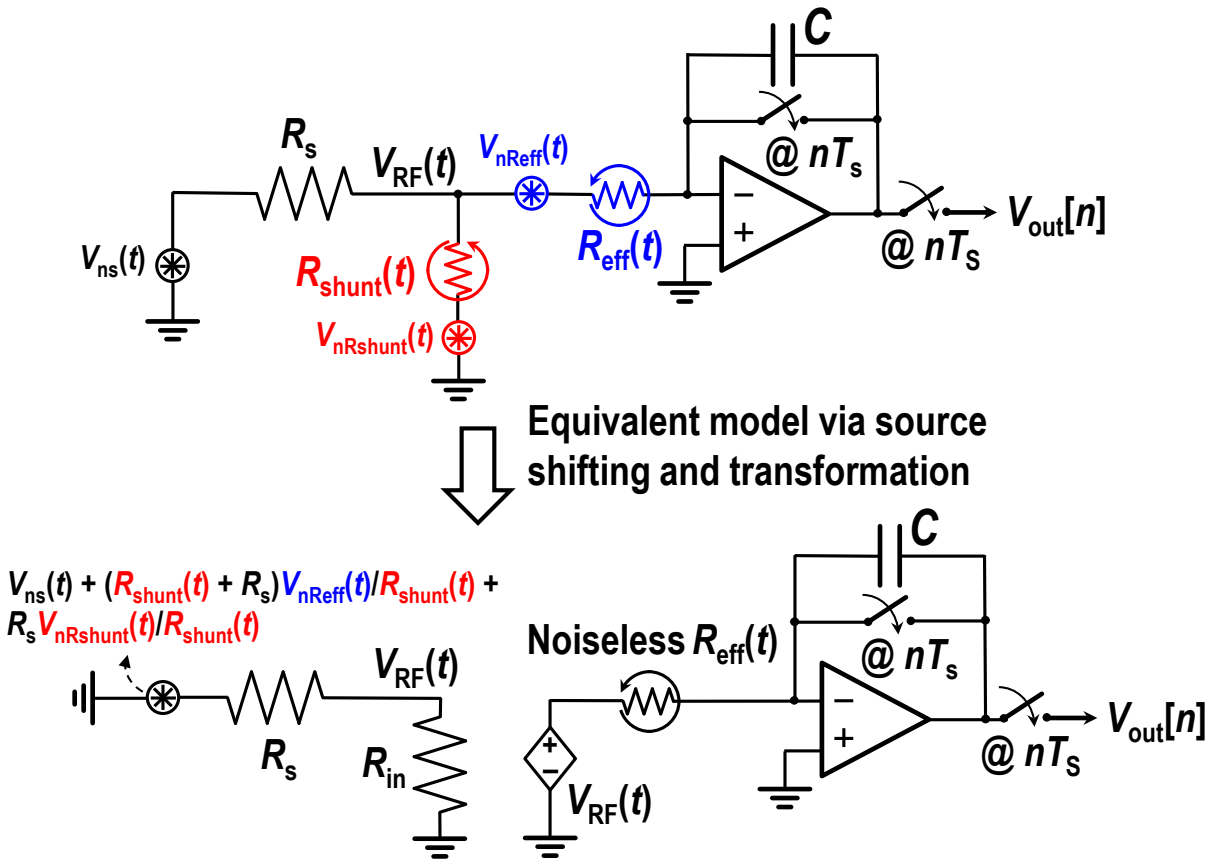

Figure 3.8: Equivalent circuit for noise analysis in the baseband of the receiver.

The second term is due to the noise of the receiver itself. In the case where $R_{\text{shunt}}(t)$ is not involved, i.e., $R_{\text{shunt}}(t) = R_{\text{shunt}}(t)_{\text{MIN}} = \infty$, the term in the square bracket is just 1. When finite $R_{\text{shunt}}(t)$ is added, $R_{\text{shunt}}(t)_{\text{MIN}} \geq R_{\text{s}}$. Then using $R_{\text{shunt}}(t) = R_{\text{s}}$, the term in the square bracket becomes 4. This means the penalty to the noise factor term contributed by the receiver will at most be worsened to 4× compared to without $R_{\text{shunt}}(t)$. As will be shown later in Section 3.4, the analysis here agrees with simulation and measurement well. Section 3.4 describes how a two-channel implementation can reduce the impact of the OFF slices on NF, and presents a complete noise analysis for the CA receiver.

3.3.3 Linearity Improvement

Moving the switches to within the feedback network brings a major advantage: owing to the loop gain, nonidealities of the feedback network, both in terms of parasitics and nonlineari-

ties, do not nominally matter. This can be seen from Fig. 3.5, where $i_{\rm k}(t)$ only depends on $R_{\rm unit}$ and $G_{\rm m,unit}$, and not on the feedback network's impedance, whether linear or nonlinear, which includes the switches' impedances. Essentially, to the first order, any nonlinear current generated will be greatly suppressed by the finite, but high, loop gain of the feedback.

Switch Nonlinearity: Its impact can be quantified using the simplified model shown in Fig. 3.9(a). $R_{\rm sw,prop}(t)$ represents the total switch resistance of the ON slices. The switch nonlinearity is modeled using a dependent current source of value, $g_{\rm sw3,prop}(t)V^3_{\rm sw,prop3}(t)$, where $g_{\rm sw3,prop}(t)$ is the total nonlinear conductance of all the ON slice switches at time t, and $V_{\rm sw,prop}(t)$ is the voltage across the equivalent switch. Only third-order nonlinearity is considered here, but the discussion can be similarly extended to other orders of nonlinearity. For the sake of simplicity, the $G_{\rm m}$ cells are assumed perfectly linear and only OOB operation is considered and accordingly, the capacitor is modeled as a short. Note that the ratio $R_{\rm sw,prop}(t) : R_{\rm eff}(t)$ is a constant, $R_{\rm sw,unit} : (R_{\rm unit} + 1/G_{\rm m,unit})$, since both the resistors and the switches in each slice are similarly scaled. Similarly, $g_{\rm sw3,prop}(t)R_{\rm sw,prop}(t)$ is a constant set by the process technology and bias conditions. Fig. 3.9(b) shows a similar model for the prior FA receiver architecture [i.e., Fig. 3.1(a)], where again, for OOB operation, the capacitor is assumed to behave as a short.

The slice-based architecture is much more linear than the prior FA architecture for two reasons. First, note that the introduced nonlinear current into the capacitor, $i_{\rm NL,prop}(t) = g_{\rm sw3,prop}(t)V^3_{\rm sw,prop}(t)/(1+A)$ is suppressed by $(1+A)$, where $A = G_{\rm m,unit}r_{\rm o,unit}$ is the voltage gain of the $G_{\rm m}$ cells. A 20-dB voltage gain is typical. The second reason is subtler but more impactful. Note that in the slice-based architecture, the voltage swing across the switch is a time-invariant, scaled version of the input signal, expressed by

$$V_{\rm sw,prop}(t) = V_{\rm RF}(t)\frac{R_{\rm sw,prop}(t)}{R_{\rm eff}(t)} = \frac{V_{\rm s}(t)R_{\rm sw,unit}}{2(R_{\rm unit} + 1/G_{\rm m,unit})}, \tag{3.4}$$

and can be reduced by a small $R_{\rm sw,unit} : R_{\rm unit}$ ratio. In contrast, in Fig. 3.9(b), the voltage swing across the switch depends strongly on the PTV resistor, $R(t)$, given by

$$V_{\rm sw,prior}(t) = V_{\rm s}(t)\frac{R_{\rm sw,prior}(t)}{R(t) + 1/G_{\rm m} + R_{\rm s}}. \tag{3.5}$$

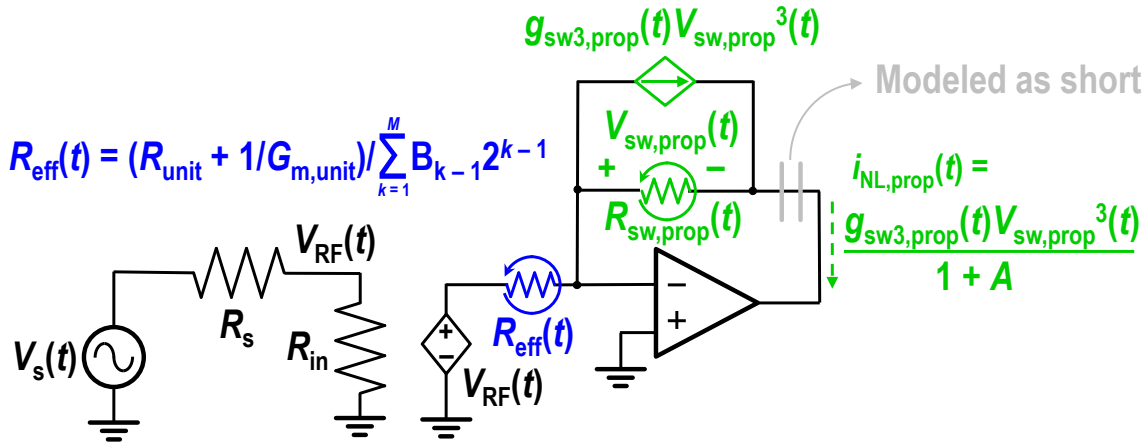

(a)

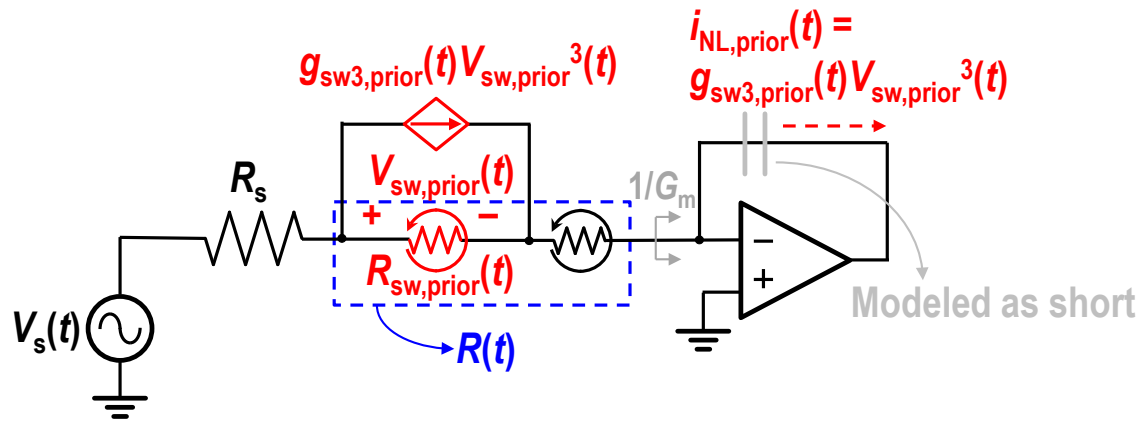

(b)

Figure 3.9: Equivalent models for analyzing OOB switch nonlinearity in (a) slice-based FA receiver and (b) prior FA receiver.

While $V_{\mathrm{sw,prior}}(t)$ is similar to $V_{\mathrm{sw,prop}}(t)$ for small $R(t)$, for large $R(t)$, $V_{\mathrm{sw,prior}}(t)$ can be significantly larger, e.g., for $G_{\mathrm{m}} = 125$ mS, $R(t)_{\mathrm{MIN}} = 16\ \Omega$, and $R_{\mathrm{sw,prior}}(t) : R(t) = 1{:}5$, which was employed in [18], the swing across the switch can be about ∼13 dB higher than in the slice-based architecture. Accordingly, the nonlinear current in Fig. 3.9(b), $i_{\mathrm{NL,prior}}(t)$, can be ∼40 dB higher for parts of the PTV cycle. Overall, over the duration of the PTV cycle, the nonlinear current flowing into the capacitor in the slice-based architecture can be 20–60 dB lower than in the original FA architecture considering both effects. The exact improvement for a given $R(t)$ can be determined analytically by considering the ratio of the

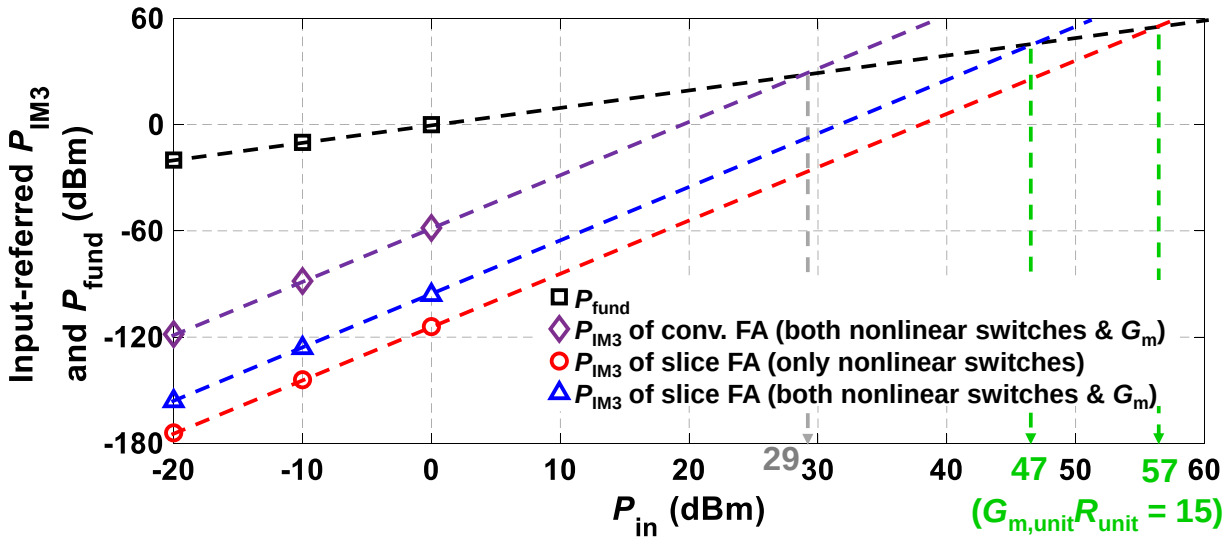

Figure 3.10: Behavioral simulation results of input-referred P_{IM3} versus P_{in} for the prior FA approach (limited by RDAC nonlinearity), proposed approach with only switch nonlinearities, and with both switch and G_{m} nonlinearities.

integrated error current over T_{s} in both cases, given by

$$\frac{\int_{t=0}^{T_{\mathrm{s}}} i_{\mathrm{NL,prop}}(t)dt}{\int_{t=0}^{T_{\mathrm{s}}} i_{\mathrm{NL,prior}}(t)} = \frac{\int_{t=0}^{T_{\mathrm{s}}} g_{\mathrm{sw3,prop}}(t)[R_{\mathrm{sw,unit}}/(2(R_{\mathrm{unit}}+1/G_{\mathrm{m,unit}}))]^3 dt}{(1+A)\int_{t=0}^{T_{\mathrm{s}}} g_{\mathrm{sw3,prior}}(t)[R_{\mathrm{sw,prior}}(t)/(R(t)+1/G_{\mathrm{m}}+R_{\mathrm{s}})]^3 dt}$$
$$\approx \frac{\int_{t=0}^{T_{\mathrm{s}}}[R(t)_{\mathrm{MIN}}/(2R_{\mathrm{s}})]^3 dt/R_{\mathrm{eff}}(t)}{(1+A)\int_{t=0}^{T_{\mathrm{s}}} R^2(t)dt/(R(t)+1/G_{\mathrm{m}}+R_{\mathrm{s}})^3}, \tag{3.6}$$

where, for simplicity, we assume $V_{\mathrm{s}}(t)$ is a constant, since the models in Fig. 3.9 are not frequency-dependent, and $R_{\mathrm{sw,unit}}$ and $g_{\mathrm{sw3,unit}}$ are the same in both approaches. Using the $R(t)$ and $R_{\mathrm{eff}}(t)$ given in Fig. 3.6, (3.6) predicts about 52-dB less integrated nonlinear current and hence approximately 26-dB IIP_3 improvement for the proposed architecture over prior FA implementation, since the linear currents in both approaches have similar magnitudes. Switch nonlinearity therefore becomes much less significant. Fig. 3.10 shows the behaviorally simulated OOB IIP_3 for prior approach (limited by the RDAC, G_{m} nonlinearity introduces a difference of less than 1 dB at that linearity level) and this approach with switch nonlinearity only and a voltage gain of all G_{m} cells = 20 dB at an offset frequency of 82 MHz. Apparently, this approach is no longer limited by switch nonlinearities. The IIP_3 improvement, $\sim$28 dB, is very close to our previous calculation.

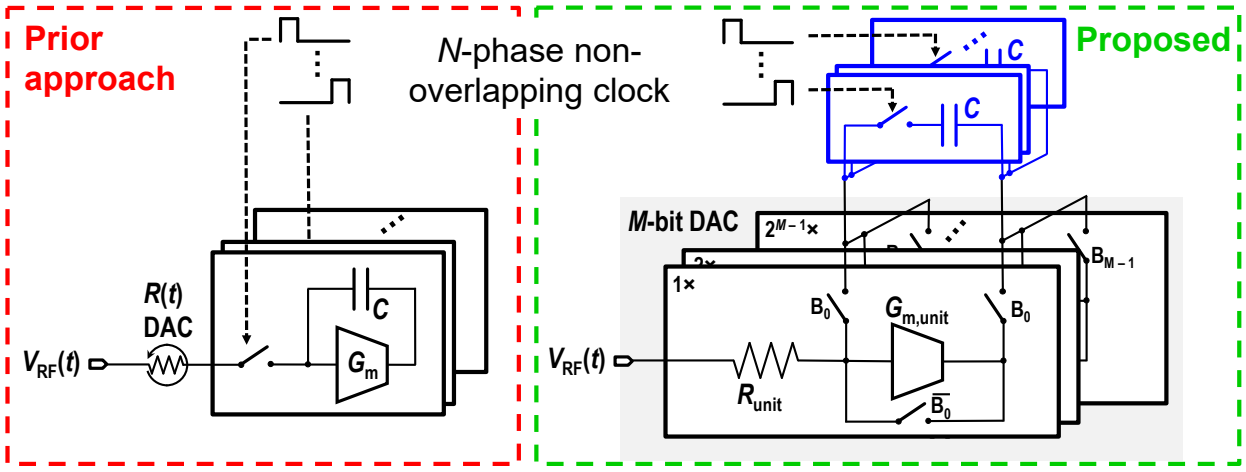

Figure 3.11: Comparison between the mixer implementations in the prior and proposed FA receivers.

G_m Nonlinearity: With switches no longer limiting the linearity performance, G_m nonlinearity becomes the dominant limiting factor. Fortunately, this effect can be suppressed in a scalable manner. By increasing $G_{m,unit}$, the virtual ground will be better and better, since $1/G_{m,unit}$ is smaller and smaller compared to R_{unit}. The voltage at the input of the G_m cells, $V_x(t)$ (see Fig. 3.5), will be smaller and smaller as well for a fixed blocker power, because the G_m cell and R_{unit} form a voltage divider for OOB blockers. The nonlinear currents, such as $G_{m3,unit}V_x^3(t)$, will also be much smaller, where $G_{m3,unit}$ is the third-order transconductance of a unit G_m cell. Moreover, in this work, instead of using N baseband G_m cells for an N-path passive mixer, the mixer is implemented in the same manner as the selection switches in the DAC, both shown in Fig. 3.11. The currents are steered to N capacitors on a rotation basis to perform downconversion (this mixer architecture is essentially the same as the gain-boosted N-path filters [43], [44], but the motivation is not completely the same). For the same power consumption of G_m cells, this work can enjoy N times larger G_m value than prior works, further enhancing the linearity. As also shown in Fig. 3.10, with G_m nonlinearity included, the slice-based approach still offers ~20 dBm IIP_3 improvement. Here, as an optimal tradeoff among power, R_{unit} noise, and linearity, we choose a $G_{m,unit}R_{unit}$ value of about 15 in this work.

3.3.4 LO Leakage Suppression

In receivers that use passive mixers without an upfront LN(T)A, various nonidealities, such as mixer switch mismatches, lead to undesirable leakage charge at the LO's fundamental frequency reaching the antenna [35]. For example, consider LO leakage in a conventional N-path mixer-first receiver. Fig. 3.12(a) shows a simplified model of LO leakage where $V_{\mathrm{LO}}(t)$, R_{drive}, and C_{eff} model the equivalent LO voltage source, mixer driver resistance, and an equivalent coupling capacitance that causes LO leakage, respectively. The LO leakage charge injected by the LO source is evenly split between the antenna and the amplifier since R_{in} is designed to match R_{s}. In contrast, the proposed architecture presents a high impedance on the antenna side (>100 Ω) and a low impedance on the amplifier side, R_{Gm}, as shown in Fig. 3.12(b). As a result, most of the leakage will not go to the antenna. A pessimistic estimate of the LO leakage reduction can be made by ignoring $R_{\mathrm{shunt}}(t)$ in Fig. 3.12(b), which would normally siphon away more of the LO leakage charge from the antenna. Now, the instantaneous LO leakage is determined by the relative magnitude of $(R_{\mathrm{eff}}(t) + R_{\mathrm{s}})$ compared to R_{Gm}, and the average LO leakage accordingly depends on the average of the former. The LO leakage reduction of the slice-based approach relative to the typical mixer-first receiver can now be shown to be

$$\frac{P_{\mathrm{s,prop}}}{P_{\mathrm{s,mixer\text{-}first}}} = \left(\frac{2R_{\mathrm{Gm}}}{R_{\mathrm{s}} + \mathrm{mean}[R_{\mathrm{eff}}(t)] + R_{\mathrm{Gm}}} \right)^2 . \tag{3.7}$$

Note that R_{Gm} is ideally $1/G_{\mathrm{m}}$ at all frequencies, and in reality, $\sim 1/G_{\mathrm{m}}$ at non-zero offset frequencies from f_{LO} and ∼30 Ω at f_{LO}, due to the equivalent Miller resistance of the capacitor under periodical reset. Using the $R_{\mathrm{eff}}(t)$ given in Fig. 3.6(a) and $R_{\mathrm{in}} = 30$ Ω, ∼22 dB reduction in leakage power is predicted by (3.7). This is validated by a 100-run Monte Carlo simulation of LO leakage at $f_{\mathrm{LO}} = 500$ MHz in both a conventional mixer-first receiver and the slice-based FA receiver as shown in Fig. 3.12(c). In both cases, the input impedances are matched to the source, and the same mixer and mixer driver sizes are used. As is evident, the mean of the LO leakage power of the proposed FA receiver front-end is less than −82 dBm, which has a reduction of about 26 dB compared to the mixer-first one, while the standard deviations are roughly the same.

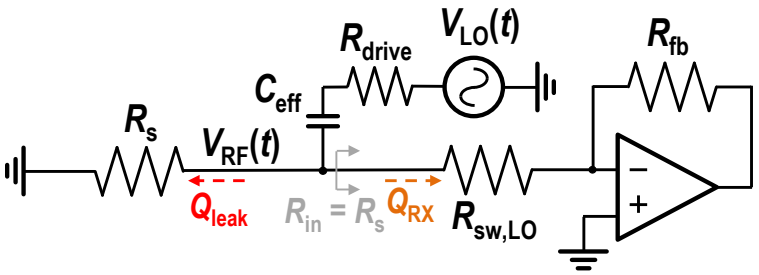

(a)

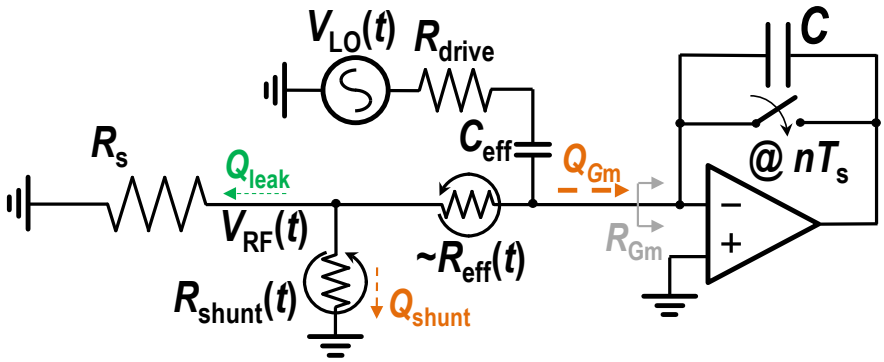

(b)

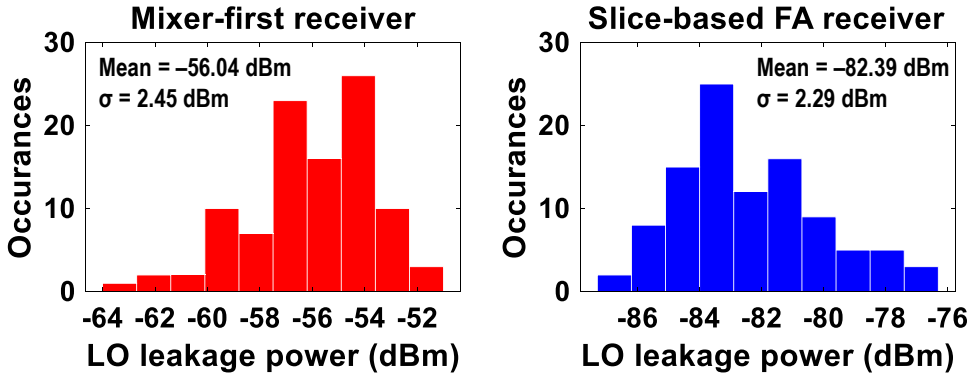

(c)

Figure 3.12: Equivalent models for LO leakage in (a) mixer-first receivers, (b) the slice-based FA receiver, and (c) histograms of 100-run Monte Carlo simulation results of LO leakage powers for a mixer-first receiver and the proposed FA receiver at $f_{\mathrm{LO}} = 500$ MHz.

3.4 Dual-Channel Slice-Based FA Receiver

Using the proposed FA architecture, a naïve implementation of a two-channel FA receiver is depicted in Fig. 3.13, where two single-channel sliced-based DACs are placed in parallel.

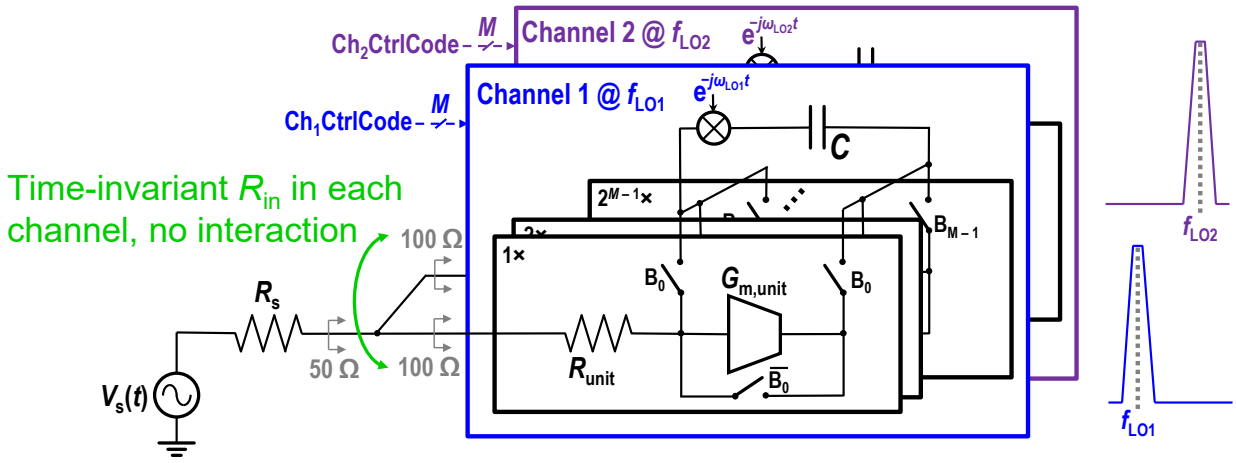

Figure 3.13: Simplistic approach to realizing a two-channel receiver using the slice-based DACs by paralleling two single-channel DACs with scaled input resistances.

Given the time-invariant input impedance of the proposed approach, the two channels will concurrently receive signals with two different carriers without interaction. Consequently, by using two LOs, reception of signals in two arbitrary channels, i.e., intra- or inter-band CA, can be realized.

However, note that, in the naïve implementation, in order to guarantee 50-Ω impedance matching, each channel's R_{in} needs to be 100 Ω, and each channel behaves as an extra shunt resistor to the other (in addition to the $R_{\text{shunt}}(t)$ formed by the OFF slices), siphoning away part of signal currents regardless of the carrier frequency. This results in about 4 dB higher NF than the single-channel case. To avoid this, the proposed dual channel slice-based FA receiver employs dynamic reuse of one channel's OFF slices as the other channel's ON slices. In other words, instead of connecting an OFF slice of channel 1 in unity buffer configuration, and thereby wasting signal current, its current would be routed to the integrating capacitor of channel 2. Of course, if $R_{\text{eff}}(t)$ of channel 2, $R_{\text{eff2}}(t)$, is equal to the shunt resistance in channel 1, $R_{\text{shunt1}}(t)$, all wasted current of channel 1 will be reused by channel 2, and vice versa. However, this may not be possible to achieve, while simultaneously guaranteeing desired FA filter responses on both channels. The proposed dual-channel FA receiver employs a good sub-optimal solution, where we set $R_{\text{eff2}}(t) = R_{\text{eff1}}(t - T_{\text{s}}/2)$, where $R_{\text{eff1}}(t)$ is the $R_{\text{eff}}(t)$ of channel 1. In addition, the MSB, which has the highest conductance among all slices, is

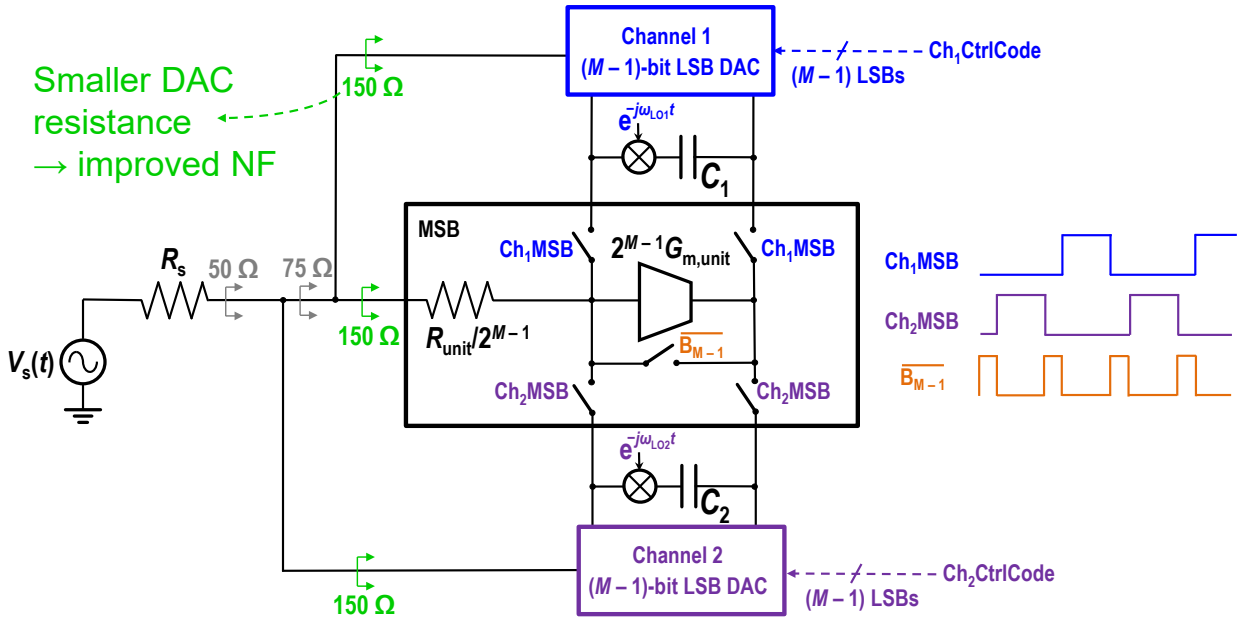

Figure 3.14: Two-channel implementation with shared MSB and scaled down resistances to lower NF.

shared between channels 1 and 2, as shown in Fig. 3.14. The MSB steers current to either channel 1's or channel 2's capacitor at a given time. When neither channel uses it, it forms a unity-gain buffer. Fig. 3.15 plots $R_{\text{eff1}}(t)$, $R_{\text{eff2}}(t)$, and the net effective shunt resistance at the RF node, $R_{\text{shunt}}(t)$, such that $R_{\text{eff1}}(t)||R_{\text{eff2}}(t)||R_{\text{shunt}}(t) = R_{\text{in}} = 50\ \Omega$ and matching is achieved. In this way, each channel presents effectively only 75-Ω input impedance and part of the shunt resistors in channels 1 and 2 are absorbed by the other channel to minimize the waste of source current. Note that this MSB sharing technique is only viable for the two-channel implementation and not scalable, unless the required filtering on the third channel is very relaxed. If more than two channels are desired, the extra channels will need to be added in the manner shown in Fig. 3.13, and the noise performance will degrade. Nevertheless, the proposed MSB sharing leads to an $\text{NF}_{\text{baseband}}$ of 7.9 dB, about 1.5 dB better than the naïve approach in Fig. 3.13. In this design, a slightly lower $\text{NF}_{\text{baseband}}$ of 7.6 dB is achieved by sizing down the slice resistances such that $R_{\text{in}} \approx 33\ \Omega$ targeting an S_{11} of -14 dB if no reactance were present at the RF node. This is simply a design choice and not fundamental to the architecture itself.

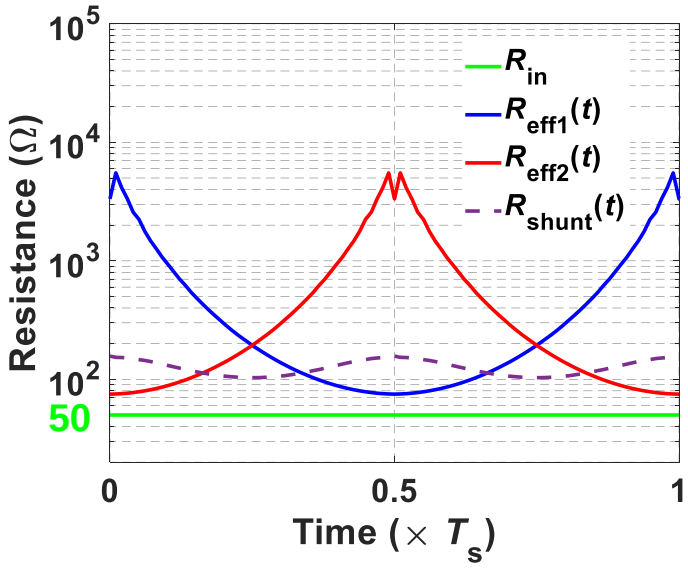

Figure 3.15: Example of resistance variations over time for $R_{\text{eff1}}(t)$, $R_{\text{eff2}}(t)$, overall $R_{\text{shunt}}(t)$ due to two channels, and $R_{\text{in}} = R_{\text{eff1}}(t)||R_{\text{eff2}}(t)||R_{\text{shunt}}(t)$.

The NF of the complete receiver can be then readily calculated by accounting for contributions due to aliasing and 4-path harmonic folding. Proceeding similarly as in Chapter 2 [18], [19], [28]

$$\begin{aligned} \text{NF}_{\text{aliasing}}(\Delta f) &= \frac{\text{PSD}_{\text{Rs}}(\Delta f)}{2kTR_{\text{s}}|G(\Delta f)|^2} = \frac{\sum_{n=-\infty}^{+\infty}|G(\Delta f + nf_{\text{s}})|^2}{|G(\Delta f)|^2}, \\ \text{NF}_{\text{harminocs}} &= \frac{1}{\text{sinc}^2(1/4)} \approx 0.91 \text{ dB}, \end{aligned} \tag{3.8}$$

where $|\Delta f| \leq f_{\text{s}}/2$ is the IB offset frequency. The average IB NF_{alias} is about 1.8 dB, which is similar to prior FA works, as mentioned in Subsection 3.2.5. Finally, the overall NF at a certain Δf for the complete two-channel system can be derived as

$$\text{NF}_{\text{total}}(\Delta f) = \text{NF}_{\text{baseband}} + \text{NF}_{\text{aliasing}}(\Delta f) + \text{NF}_{\text{harmonics}}. \tag{3.9}$$

The calculated NF_{total}, whose average across the band is about 10.3 dB, is shown in Fig. 3.16 together with the simulated and measured NFs for $f_{\text{s}} = 10$ MHz and $f_{\text{LO1}} = 500$ MHz (f_{LO2} is set to be 740 MHz). Both simulation and measurement agree with the calculation well, and the residual difference between simulation and calculation is due to parasitics.

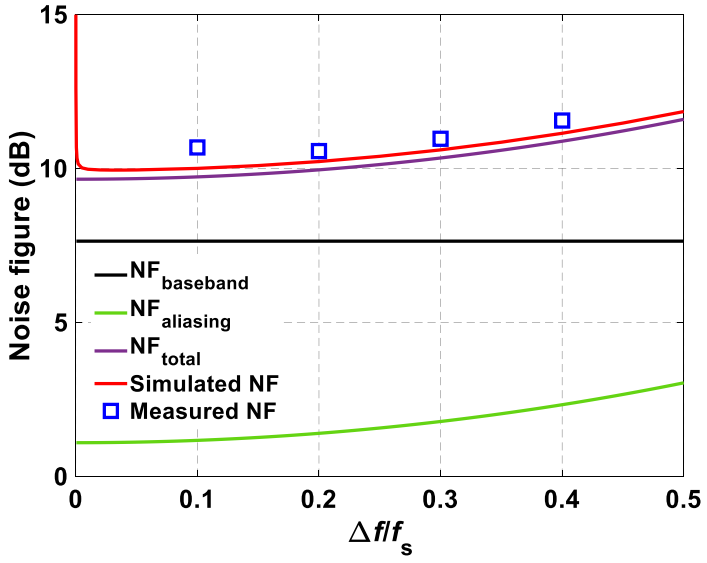

Figure 3.16: Calculated NF for the receiver front-end and comparison with the simulated and measured results.

3.5 Circuit Implementation

Fig. 3.17 shows the block diagram of the implemented dual-channel slice-based FA receiver front-end. The receiver front-end consists of only switches, inverter-based amplifiers, digital circuits, and passive devices (namely, resistors and capacitors). All switches are realized using equally sized PMOS and NMOS devices to minimize clock feedthrough and charge injection.

Each channel is realized by a 4-path passive mixer and a 13-bit binary-weighted DAC using the slice-based architecture. This number of bits here is used to ensure that the DAC resolution does not limit filter shape [19]. The unit selection switches are designed to have a ratio of $R_{\text{sw,unit}} : R_{\text{unit}} \approx 1 : 10$, such that the linearity is not limited by switches. The bias of the receiver is set to about half of the supply voltage, V_{DD}, by resetting baseband amplifiers and OFF slices' self-bias. The DACs switch at a rate of $f_{\text{clk}}/2$, where f_{clk} is the frequency of an external clock signal. The effective PTV resistor variations in the two channels, $R_{\text{eff1}}(t)$ and $R_{\text{eff2}}(t)$, respectively, with a period of T_{s}, are also sketched in Fig. 3.17 to show how they are staggered to realize MSB sharing. The sampling and reset clocks are derived from the same

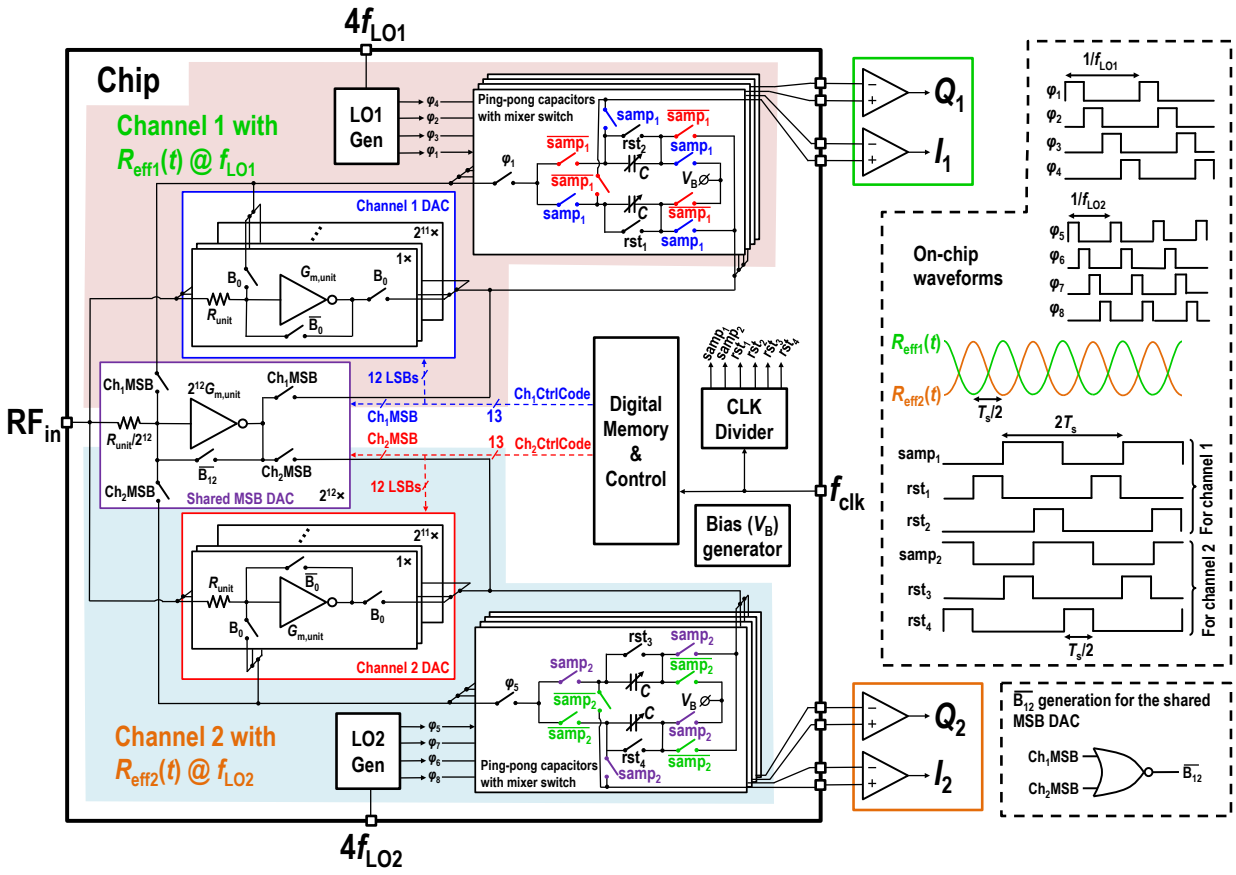

Figure 3.17: Complete block diagram of the implemented receiver front-end.

f_{clk} signal. As discussed in Section 3.4, although this is not required, $R_{\text{eff2}}(t)$ is deliberately chosen to be an equal but shifted version of $R_{\text{eff1}}(t)$. This shift guarantees that $R_{\text{eff1}}(t)$ and $R_{\text{eff2}}(t)$ are never simultaneously low, allowing the MSB slice to be shared, thereby saving power and area, and reducing the NF penalty from the OFF-slice shunt resistance. Also, it allows smaller area used for the digital memory. This, however, also constrains the filter shapes of the two channels to be identical, and it is no longer possible to use different filter shapes in the two channels. The liberty of having different filter shapes in the two channels can be achieved by using more digital memory to set $Ch_2CtrlCode$ separately and designing the two channels' impulse responses carefully to avoid overlapped usage of the MSB slice.

The integrating capacitors are realized in a ping-pong fashion to allow one capacitor integrating signal current while the other being read and then reset. They are tunable

from 10 to 80 pF. The mixer switches are driven by two sets of 25% duty-cycled non-overlapping clock signals at f_{LO1} and f_{LO2}, respectively, to mix the RF current to baseband for integration. The mixer switches are designed to have a 4-Ω ON resistance. Note that f_{LO1} and f_{LO2} can be any value within the RF range from a functional perspective. The constraint mainly comes from the required sideband rejection, i.e., the rejection of the signal at the other channel's frequency at one channel's output, when operating with two channels.

3.5.1 Low-Noise Mode

The proposed operation of the FA receiver presents time-invariant input impedance, and can therefore provide good filtering and high linearity, but it also leads to high NF (>10 dB), which is not preferred, especially when no strong blockers are present, since when no blockers are present, the NF requirement is more stringent, while when blockers are present, it may be relaxed [45], [46]. Therefore, in addition to the default high-performance (HP) mode that has been discussed so far, we also introduce an extra low-noise (LN) mode for the receiver front-end. This is done by disabling the switches that short the inputs and outputs of the G_{m} cells when the slices are OFF, i.e., $\overline{\mathrm{B_{k-1}}}$, as shown conceptually in Fig. 3.18(a) using one of the channels. In the LN mode, the operation is very similar to the time-interleaved FA in [19], except the two paths have different LOs and their outputs are not summed. The second channel still presents itself like a shunt resistor to the first channel, and vice versa. However, as can be seen from the sketches of $R_{\mathrm{eff1}}(t)$ and $R_{\mathrm{eff2}}(t)$ in Fig. 3.17, the two resistances vary in a way that when one is high, the other is low, and vice versa. Their interaction is relatively weak, similar to [19]. This reduces the $\mathrm{NF_{baseband}}$ to about 5 dB, thus helping improve the NF by about 2–3 dB. The calculation for the LN-mode NF is almost the same as that in [19], except that the output noise power spectral density (PSD) is white as the outputs are not summed to realize time-interleaved FA filtering, so we omitted it here for brevity. However, some degradation (∼1–2 dB) compared with [19] is expected, since the minimum input resistance in [19] is $R(t)_{\mathrm{MIN}} + R_{\mathrm{sw,LO}} + 1/G_{\mathrm{m}} \approx 30\ \Omega$, while it is about 50 Ω in this work. Adding few extra bits that are not used in the HP mode to lower the LN-mode $R_{\mathrm{in}}(t)_{\mathrm{MIN}}$ will help in this regard (to achieve the same $R_{\mathrm{in}}(t)_{\mathrm{MIN}}$ as in [19]), but is not

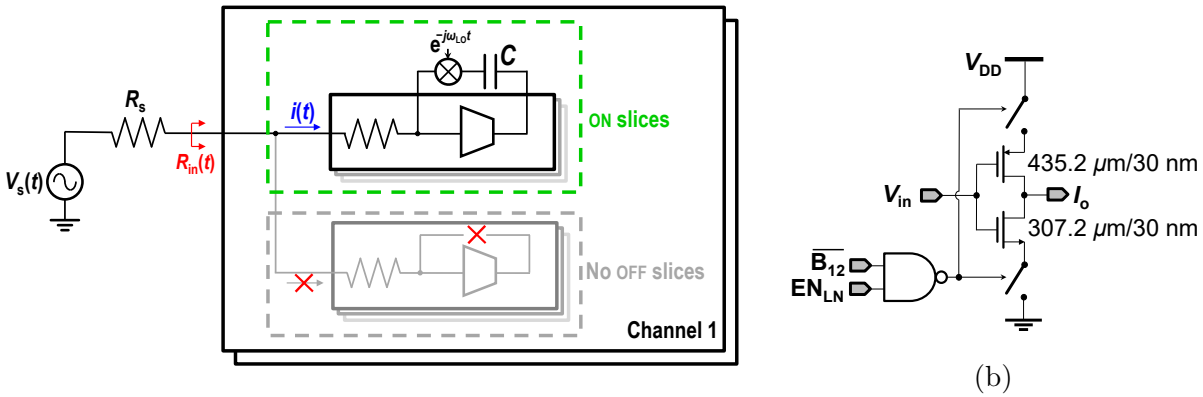

(a) (b)

Figure 3.18: (a) Operation principle of the LN mode, and (b) schematic of the G_m cell in the MSB slice.

implemented on this chip. In the LN mode, the G_m cells in the OFF slices are powered down to save power by controlling switches at the inverter-based amplifiers' supply and ground, similar to the G_m cells in Chapter 2. The schematic of the G_m cell in the MSB slice is shown in Fig. 3.18(b), where high-V_T devices are used to increase the gain and g_m/I_D efficiency, and those in the LSBs are binarily scaled from it. EN_{LN} is the control signal that enables power saving in the LN mode. Due to the lack of constant input impedance, some tradeoff in designing $R_{eff1}(t)$ and $R_{eff2}(t)$ for better noise performance, and the operation being less well behaved than the HP mode, the filtering, linearity, and some other metrics are expected to degrade slightly. By employing an integrated blocker detector [47] or a spectrum scanner [17] to determine if strong blockers exist, the HP or LN modes can be chosen for the proper scenarios, respectively. Note that further NF improvement of close to 3 dB can be achieved by employing noise cancellation, which has been demonstrated in Chapter 2 for FA receivers, for both HP and LN modes, at the expense of linearity, power, and silicon area.

3.6 Measurement Results

The implemented test chip was fabricated in TSMC 28-nm CMOS process. Fig. 3.19 shows the die photo of the chip. The active area is 1.3 mm^2. The supply voltage of the whole chip is 0.9 V. At $f_{LO1} = 500$ MHz and $f_{LO2} = 740$ MHz, the entire chip consumes 50- and 42-mW

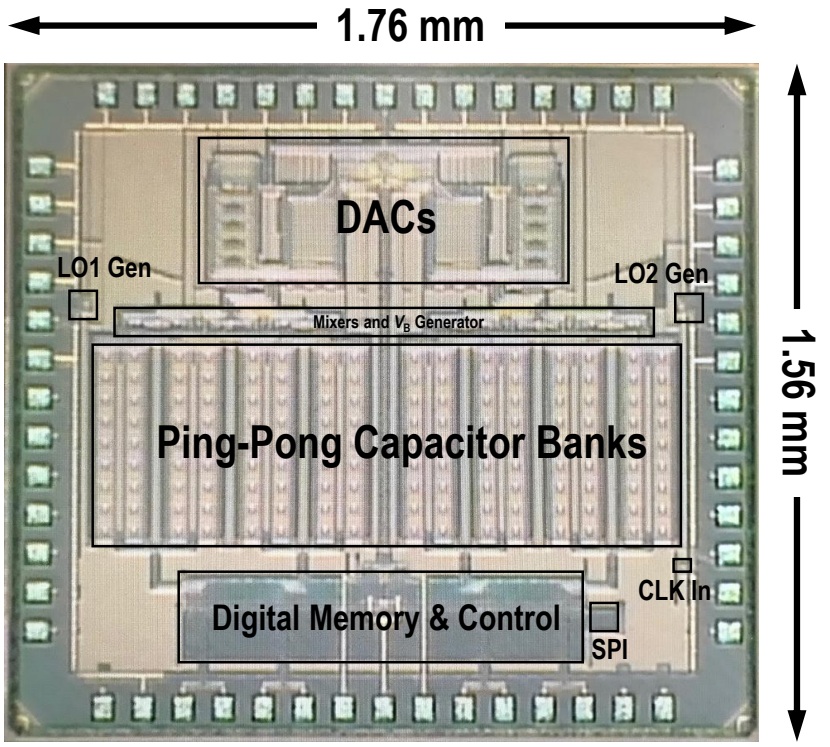

Figure 3.19: Chip micrograph.

power in the HP and LN modes, respectively. The DAC consumes 31-mA current in HP mode, and 22 mA in LN mode. The digital control circuitry dissipates ∼10 mA at a nominal f_{clk} of 2 GHz, regardless of the mode of operation. The frequency of f_{clk} is chosen to make the image of the filter passband caused by the sampled-and-held waveform of $R_{\text{eff}}(t)$ due to it being digitally controlled, driven by f_{clk}, suppressed by ∼50 dB [18]. Each LO divider and its associated switch drivers consume about 11 mA/GHz. The sampled outputs are buffered externally on board for measurement. The DACs are dc calibrated at startup to account for mismatches of resistances in different slices.

Fig. 3.20(a) shows the measured single-channel 10-MHz BW filter responses in three different filter configurations (filters 1–3) with different transition BW and A_{stop} in the default HP mode. The transition BWs for filters 1–3 were 17, 22, and 31 MHz, respectively, while the achieved A_{stop} was observed to be better than 35, 45, and 51 dB, respectively. Fig. 3.20(b) shows the filter shape at $f_{\text{LO}} = 170$ MHz. Like a 4-path mixer-first receiver,

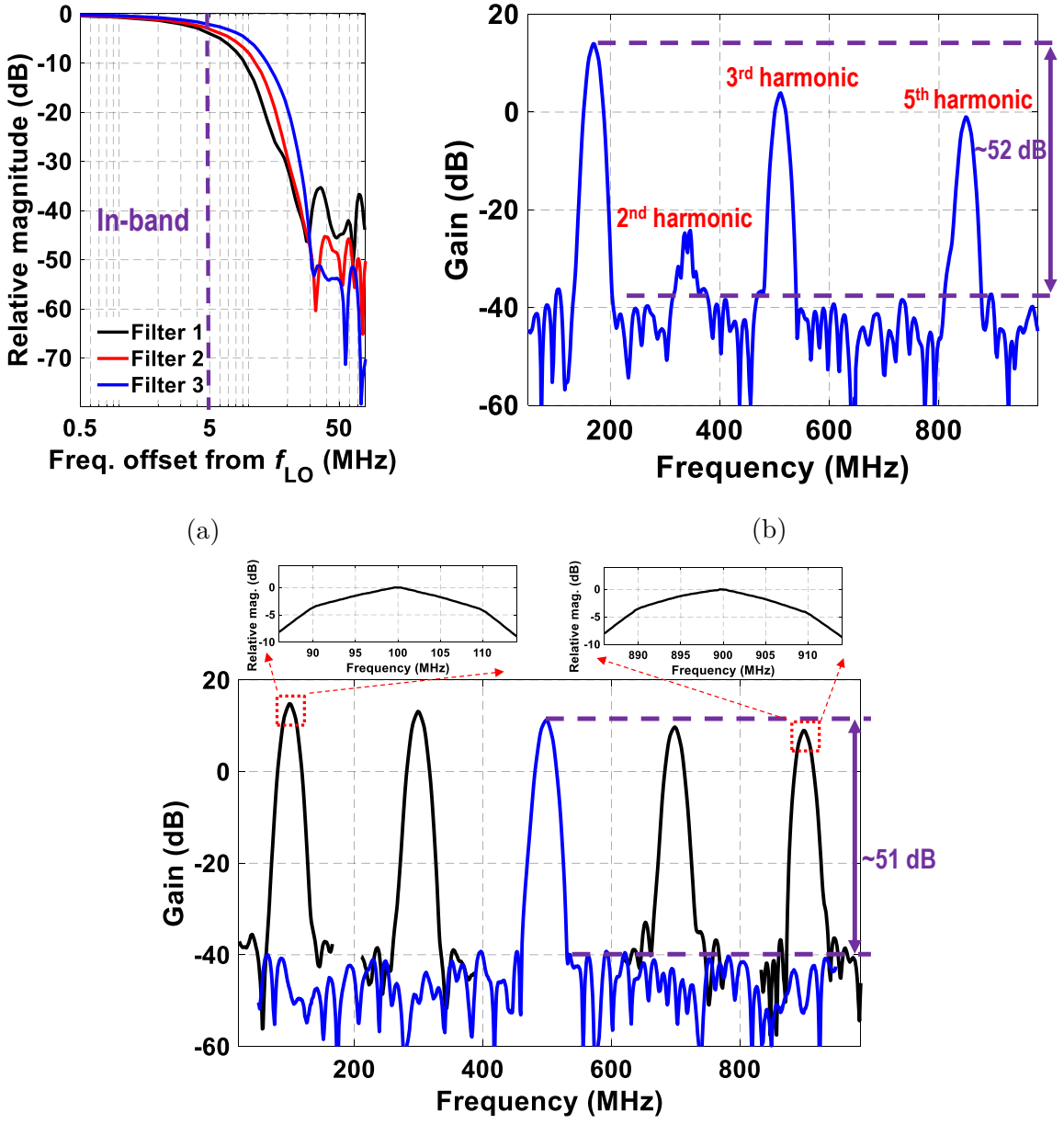

Figure 3.20: (a) Measured single-channel 10-MHz RF BW filter responses in the HP mode, (b) single-channel filter 3 at $f_{\mathrm{LO}} = 170$ MHz, showing the harmonic responses, and (c) single-channel filter 3 for different LO frequencies.

the odd harmonics will fold in. The second harmonic rejection was slightly worse than that in [18]. Fig. 3.20(c) shows the single-channel filter at different LO frequencies in filter 3 configuration, with zoomed-in views for the filter shapes around f_{LO} at the lower and higher

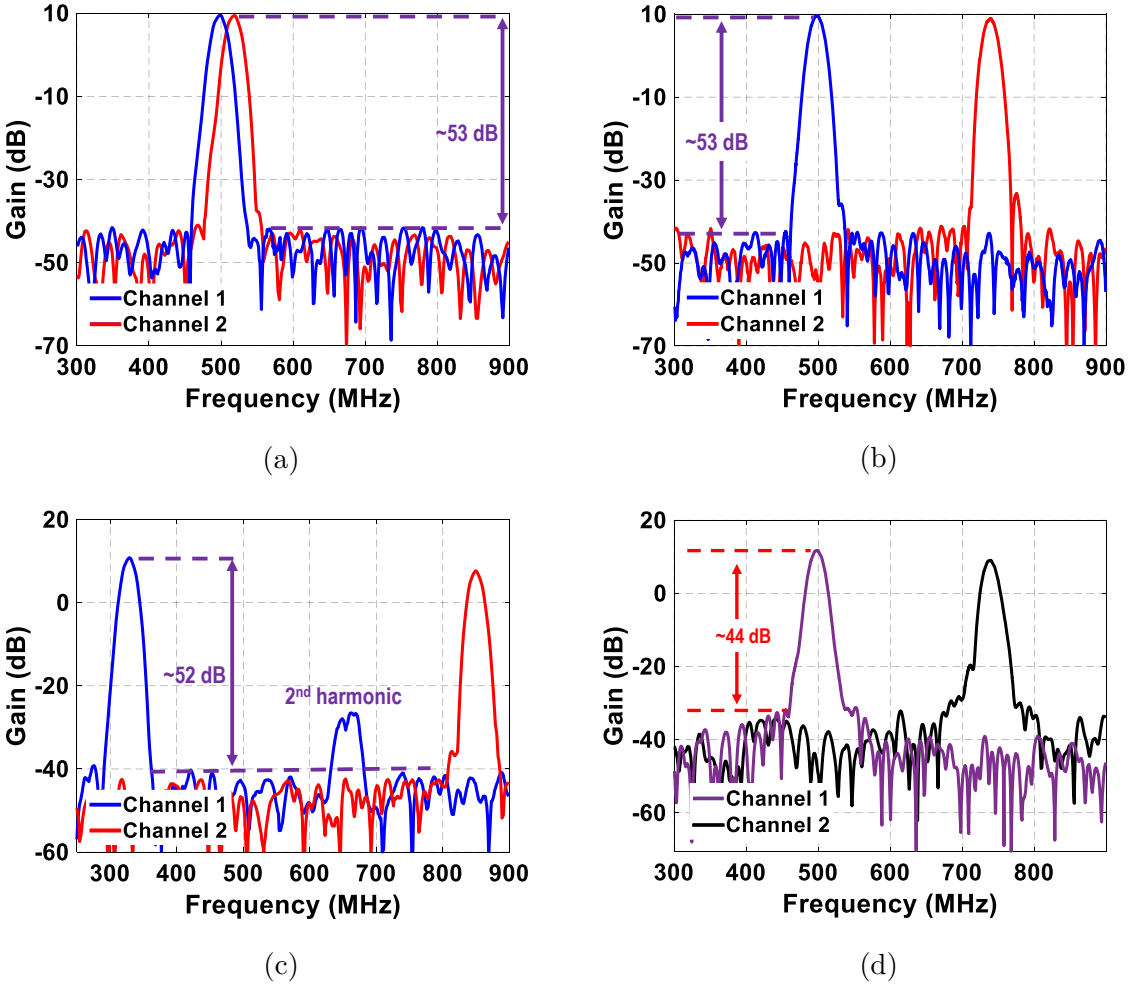

Figure 3.21: Measured concurrently receiving filter shapes in the HP mode (a) at $f_{\mathrm{LO1}} = 500$ MHz and $f_{\mathrm{LO2}} = 520$ MHz, (b) at $f_{\mathrm{LO1}} = 500$MHz and $f_{\mathrm{LO2}} = 740$MHz, (c) at $f_{\mathrm{LO1}} = 330$ MHz and $f_{\mathrm{LO2}} = 850$ MHz, and (d) in the LN mode at $f_{\mathrm{LO1}} = 500$MHz and $f_{\mathrm{LO2}} = 740$MHz.

ends of the LO range. Figs. 3.21(a), 3.21(b), and 3.21(c) show the measured concurrent receiving two-channel filter responses with $f_{\mathrm{LO1}} = 500$ MHz and $f_{\mathrm{LO2}} = 520$ MHz, $f_{\mathrm{LO1}} = 500$ MHz and $f_{\mathrm{LO2}} = 740$ MHz, and $f_{\mathrm{LO1}} = 330$ MHz and $f_{\mathrm{LO2}} = 850$ MHz, respectively, in the HP mode. Fig. 3.21(d) shows that in the LN mode with $f_{\mathrm{LO1}} = 500$ MHz and $f_{\mathrm{LO2}} = 740$ MHz. It is observed that the stopband rejection was deteriorated to about 44 dB in the LN mode with worse filter shapes. The following measurements were performed with the same filter BW and LO frequencies as Figs. 3.21(b) and 3.21(d) unless otherwise specified.

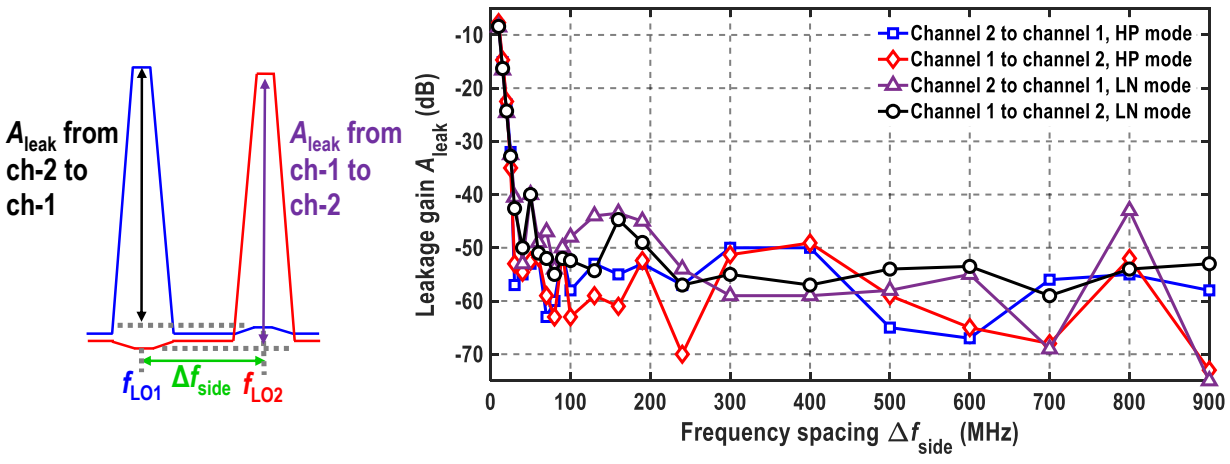

Figure 3.22: Measured sideband leakage.

The measured sideband rejection of both channels in both modes with different spacing between the two LO frequencies is depicted in Fig. 3.22. The measurement was performed by measuring one channel's output when the RF input frequency is close to the other channel's LO frequency (in our measurement, we chose an offset frequency $\Delta f = 1$ MHz from the LO frequencies for the input signal). The sideband rejection is almost the same as the filter shape.

Fig. 3.23(a) shows the linearity measurements for channel 1 with 10-MHz BW, $f_{\mathrm{LO1}} = 500$ MHz, and $C = 80$ pF in both modes. While the IB $\mathrm{IIP_3}$ was measured to be about +12 dBm in both modes, the OOB $\mathrm{IIP_3}$ was about +35 dBm in the HP mode, and about +27 dBm in the LN mode at an offset frequency, Δf, of 82 MHz away from the corresponding channel's f_{LO}. In both modes, the $\mathrm{B_{1dB}}$ was better than +12 dBm at the same offset frequency. Fig. 3.23(b) shows the measured $\mathrm{IIP_3}$ of both channels in both modes at $f_{\mathrm{LO}} = 82$ MHz at different LO frequencies. On average, the $\mathrm{IIP_3}$ was about +35 dBm in the HP mode and +25.5 dBm in the LN mode.

The receiver was further characterized with concurrently receiving error vector magnitude (EVM) measurements. Two different 2.5-MSps 16QAM modulated signals with $\alpha = 0.35$ were combined and fed to the input of the receiver. The power of each carrier was about -42 dBm at the input of the receiver, the power level of which is limited by the low gain

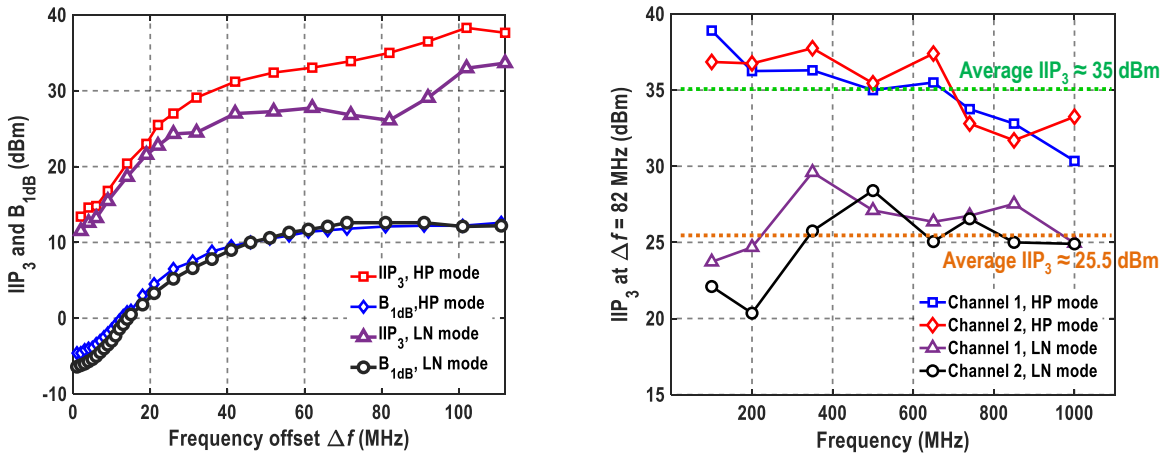

(a) (b)

Figure 3.23: (a) Measured $\mathrm{IIP_3}$ and $\mathrm{B_{1dB}}$ of channel 1 at $f_{\mathrm{LO1}} = 500$ MHz for different offset frequencies, and (b) $\mathrm{IIP_3}$ of both channels at 82-MHz offset frequency for different LO frequencies, in both modes.

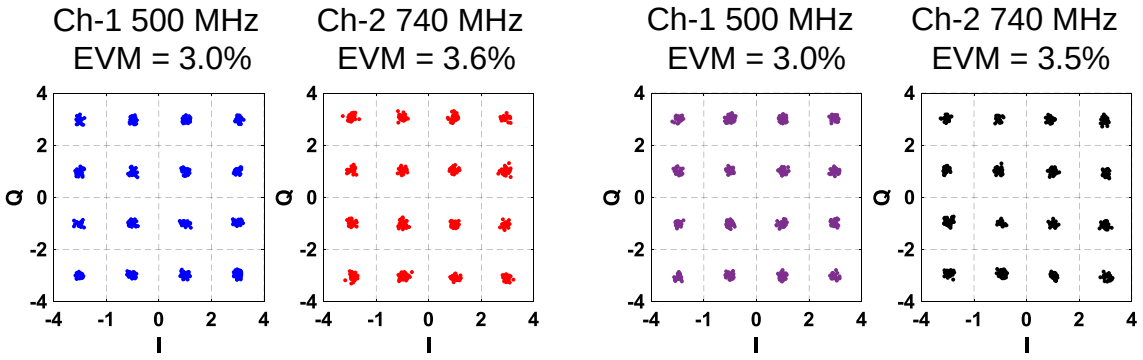

(a) (b)

Figure 3.24: Measured demodulated constellations of the two carriers in (a) HP mode and (b) LN mode.

of the front-end and the input-referred noise of the oscilloscope. The measurements were performed without I/Q error calibration. The demodulated constellations in the two modes are shown in Fig. 3.24. The worst-case EVM was 3.6%rms.

Fig. 3.25(a) shows the measured $\mathrm{S_{11}}$ in the two modes together with the simulation results. In the HP mode, the $\mathrm{S_{11}}$ was better than -10 dB till about 2.3 GHz, partially

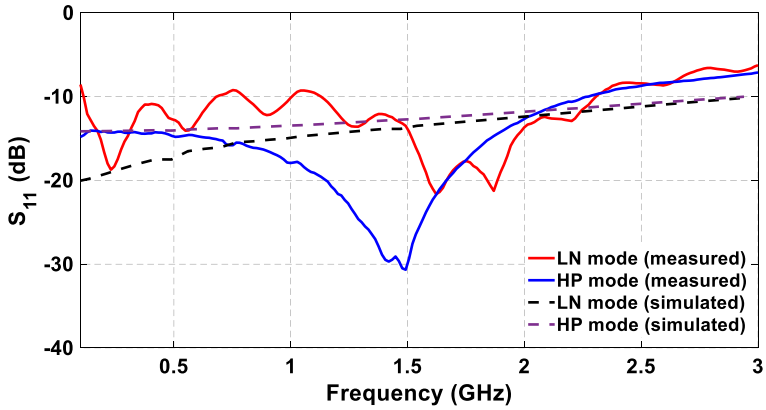

(a)

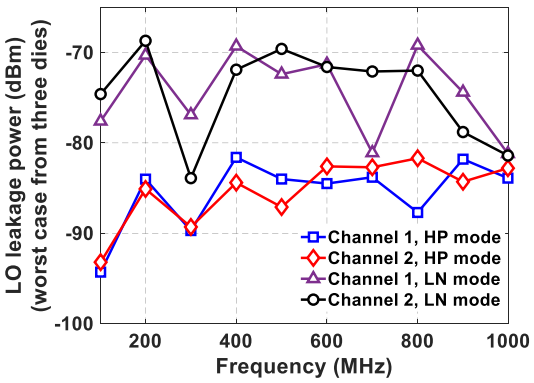

(b)

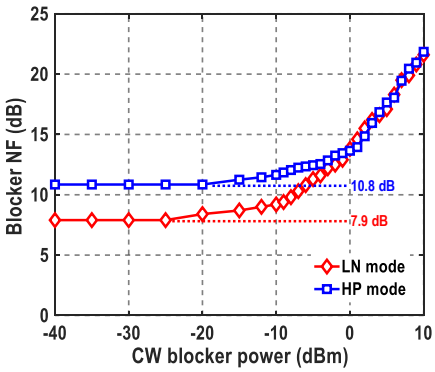

(c)

Figure 3.25: Measured two-mode (a) S_{11}, (b) LO leakage at different LO frequencies, and (c) blocker NF in the presence of a CW blocker at $\Delta f = 60$ MHz for a 10-MHz RF BW filter with $f_{LO1} = 500$ MHz.

confirming the achieved wideband input matching. At low frequencies, it was about -14 dB, as predicted by the designed input resistance. The dip at about 1.5 GHz is likely due to the reactance introduced in measurement, from measurement equipment, bond wire, board, etc. The S_{11} was less well behaved in the LN mode, but still better than -8.5 dB across the frequency of interest (0.1–1 GHz). Fig. 3.25(b) shows the worst-case LO leakage power measured from three dies. In the HP mode, it was better than -81 dBm, and in the LN mode it was better than -68 dBm. The measured NF was 10.8 dB in the HP mode and 7.9 dB in the LN mode at 500-MHz LO. They were worsened to about 13.6 and 13.8 dB, respectively,

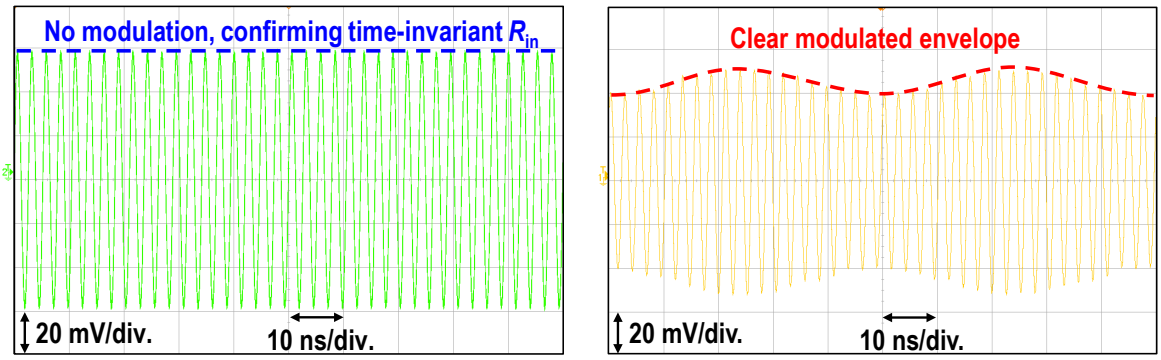

(a) (b)

Figure 3.26: Measured voltage waveform at the RF node of the receiver, $V_{\mathrm{RF}}(t)$, when a sinusoidal signal at 380 MHz is injected to its input, in (a) HP mode and (b) LN mode.

when a 0-dBm continuous-wave (CW) blocker was present at 60-MHz offset, shown in Fig. 3.25(c). This is mostly due to the phase noise of the LO dividers, since the front-end itself is very linear. The linearity, S_{11}, and noise measurements did not vary appreciably between channels and configurations.

Since the signal processing is primarily done at RF in the proposed FA receiver, due to the presence of parasitics, performance at higher carrier frequencies is in general worse than that at lower carrier frequencies. This is because the parasitics load the G_{m} cells and the virtual grounds are less well behaved at higher LO. Metrics that depend on good virtual grounds would therefore suffer at higher carrier frequencies. It can be seen that, for example, the OOB IIP_3 degrades with higher LO frequencies. A few dB of NF degradation also appears at high LO frequencies, similar to the mixer-first ones [9]. Better layout and finer technology nodes would help reduce the parasitics and hence push the operational frequency higher.

As a final remark, a sinusoidal signal at 380 MHz was fed to the input of the receiver. Fig. 3.26 shows the voltage waveform at the RF node, $V_{\mathrm{RF}}(t)$, of the receiver in the HP and LN modes, respectively, captured using an oscilloscope. Obviously, the LN mode shows clear modulation on the envelope of the waveform, while the HP mode has none. This helps confirm the achieved time-invariant R_{in} in the default HP mode.

Table 3.1 summarizes the performance of this work and compares it with the state-of-the-

Table 3.1: Performance Summary and Comparison with State-of-the-Art Single- and Multi-Channel Receivers and Filters

	Single-channel receivers/filters				Carrier-aggregation receivers				
	[19] JSSC'18	[30] JSSC'19	[36] JSSC'19	[38] JSSC'20	[20] JSSC'15	[39] JSSC'18	[40] JSSC'21*	**This work**	
								LN mode	**HP mode**
Architecture	TI-FA	*N*-path	*N*-path	*N*-path	Current-domain signal process.	Code-domain *N*-path	Multi-branch mod.-mixer-clock	**Slice-based FA**	
CMOS technology	65 nm	28 nm	65 nm	28 nm	65 nm	65 nm	65 nm	**28 nm**	
RF freq. (GHz)	0.1–1	0.1–2	0.8–1.1	0.2–2	0.5–3	0.5–1.4	0.3–1.3	**0.1–1**	
RF input	Differential	Differential	Differential	Single-ended	Differential	Differential	Differential	**Single-ended**	
BW (MHz)	2.5–40	13	30–50	18	1–30	2	10–66	**5–20**	
No. of channels	1				3	2	2	**2**	
Carrier spacing	N/A				<100	<700	200–600	**30–900**§	
A_{stop} (transition BW)	>58 (2.5× BW)	>47# dB (6× BW)	>17 (0.5× BW)	>27# (1.7× BW)	>30 (3× BW)	>28# (10× BW)	>60# (12× BW)	**>44 (3.2× BW)**	**>51 (3.2× BW)**
S_{11} (dB)	<–9	<–8#	<–7#	<–10#	<–10#	<–11#	<–6#	**<–8.5**	**<–14**
IB IIP_3 (dBm)	+8.2	+5#	+25	+1.5#	–28	–26	–6.9	**+11.5**	**+13.4**
OOB IIP_3 (dBm)	+24 (Δ*f*/BW = 6)	+44 (Δ*f*/BW = 12.3)	+24 (Δ*f*/BW = 1)	+33 (Δ*f*/BW = 4.4)	–4.8 (Δ*f*/BW = 4)	–15 (Δ*f*/BW = 10)	+16 (Δ*f*/BW = 12)	**+25 (Δ*f*/BW = 8)**	**+35 (Δ*f*/BW = 8)**
OOB IIP_2 (dBm)	+64	+90	+61	N/A	N/A	N/A	N/A	**+71 (Δ*f*/BW = 8)**	**+82 (Δ*f*/BW = 8)**
OOB B_{1dB} (dBm)	+12 (Δ*f*/BW = 6)	+13 (Δ*f*/BW = 12.3)	+9 (Δ*f*/BW = 1)	+12 (Δ*f*/BW = 4.4)	–1	–11.8	+4	**+12.6 (Δ*f*/BW = 8)**	**+12.1 (Δ*f*/BW = 8)**
LO leakage (dBm)	N/A	N/A	–45	N/A	N/A	N/A	N/A	**<–68**	**<–81**
Sideband rej. (dB)	N/A				N/A	35	>48	**>43**	**>49**
Supply voltage (V)	1.2/1	1.2/1	1	1.2	1.2/2.5	N/A	1.2	**0.9**	
Power (mW)	75–99	34–96	80–97	146.6–179	84/channel	18/channel	19.6/channel	**16–27.5 /channel**	**21–31 /channel**
NF (dB)	6.5–8.5	4.1–10.3	5.0–8.6	4.3–7.6	4.8	3.4–4.9	12.8–12.9	**7.8–12.0**	**10.5–14.1**
Gain (dB)	23	16	–4.2	13	50	38.5	53.2	**12**	**10**
Area (mm^2)	2.3	0.8	1.9	0.48	7.8†	0.31	1.8	**1.3**	

Estimated from reported data * High-linearity mode only † Including on-chip frequency synthesizer

§ For achieving a rejection of the other carrier by more than 40 dB. Otherwise, the spacing can be arbitrarily small till the two channels become adjacent.

art single-channel receivers and N-path filters, and multi-channel receivers. The implemented prototype maintains the sharp filtering of single-channel FA, even in a dual-channel mode. The filter sharpness is close to that of [19] without using time-interleaving. Better S_{11} than [19] is also achieved. While the NF is worse than most of the other multi-channel receivers, it achieves an IB and OOB IIP_3 as high as +13 and +35 dBm, respectively, which are both close to 20 dB higher than prior multi-channel works. The B_{1dB} of this work, which is better than +12 dBm, is at least 8 dB higher than the prior multi-channel receivers as well. The supply voltage is mere 0.9 V, which is the lowest among all. The overall performance is similar or even better than the single-channel ones. Note that the overall signal gain of this work is lower than prior art. Signal gain can be improved by using additional baseband stages. The linearity of these additional stages is not critical due to the high rejection provided by the front-end. However, the relatively lower front-end gain means that baseband stages need to

maintain a moderate noise performance in order not to degrade the overall NF. This would add to system power consumption but since the sampling rate is low, the additional power overhead is not expected to be high. Alternatively, the integrating capacitor C can be made smaller to increase the gain, but the G_{m} cells may need to be designed to achieve higher gain and g_{ds} nonlinearity might be more pronounced.

CHAPTER 4

Alias Cancellation for Filter-by-Aliasing Receivers

4.1 Introduction

While presenting a charming method to build high-selectivity receivers using periodically time-varying circuits, as briefly described in Chapter 3, FA receivers inherently face a unique problem: the rejection is finite due to finite $R(t)$ precision and parasitics [18], and the residual aliases present at the output of the receivers cannot be removed after the sampling operation, which is also core to the FA operation (prior to sampling, no sharp filtering is realized). One way to mitigate this is to incorporate time-interleaving and obtain certain level of OSR [28] for unwanted signals in the transition band. However, this will become more and more costly when higher and higher OSR is demanded, and it does not work for blockers in the stopband. Even though FA receivers have demonstrated high stopband rejection up to 70 dB [19], it is not sufficient in some applications. In this Chapter, we propose a technique to solve this problem to a good extent for FA receivers, where the residue blockers can actually be reduced after the sampling operation (or in other words, canceled) by using another receiver channel for blocker reception and employing digital signal processing (DSP). Briefly speaking, baseband digital filters are built to create replicas of the blocker aliases through scaling the received blocker from a second channel, which then can be used to subtract the blocker aliases at the FA receiver's output digitally. While there are many ways to find the correct digital filters, the approach we employed to building them is to send a sinusoid to the input of the two receivers simultaneously and sweep the frequency of the sinusoid to obtain the effective frequency responses between the FA receiver and the other receiver, whereas the digital filters should match the measured frequency responses. In order to demonstrate this

technique, we utilize the chip fabricated in Chapter 3 and off-the-shelf ADCs in conjunction with MATLAB algorithms. The achievable cancellation on measured data is about 15 dB on average across the band. This Chapter is organized as follows. Section 4.2 reviews the FA residual alias problem with an example. Section 4.3 describes proposed alias cancellation technique, followed by measurement results and discussion in Section 4.4.

4.2 Residual Alias Problem of FA Receivers

Now let us consider the FA receiver shown in Fig. 1.6, the mixer will downconvert signals to baseband, and then the baseband FA filter performs filtering at the sampled output. The OOB blockers will hence be downconverted to a frequency outside the BW of the baseband FA filter. Equivalently, the blocker will be suppressed by the stopband rejection of the FA filter and then alias to within the band (in principle the filtering and aliasing occur simultaneously, but here we explain it this way for easy comprehension, since this is typically what happens to a conventional receiver with a sampled output, e.g., an ADC at its output). The wanted signal, on the other hand, will be downconverted to within the bandwidth of the baseband FA filter by the mixer, and then remain at the same frequency albeit being slightly shaped due to the in-band filter droop. As a result, as far as the output of the FA receiver is concerned, now the blocker and signal are both in-band and cannot be separated from each other, as shown in Fig. 4.1 (we look at the baseband filter only and omit the mixing operation for simplicity), and the eventual SNR is limited by, in addition to noise and nonlinear distortions, the residual alias of the blocker. Note that, while we use single-tone signals to elaborate this problem, and the two signals seem separable due to their distinct frequencies, practical signals are wideband and become overlapped with each other after sampling and hence not separable [recall Fig. 1.7(b)]. In addition to the case we show here where the blocker is in the stopband, for undesirable signals within the transition band, the same phenomenon occurs except the filtering is less since the rejection within the transition band is lower than that in the stopband.

Ideally with an $R(t)$ of infinite precision and the absence of parasitics, the stopband

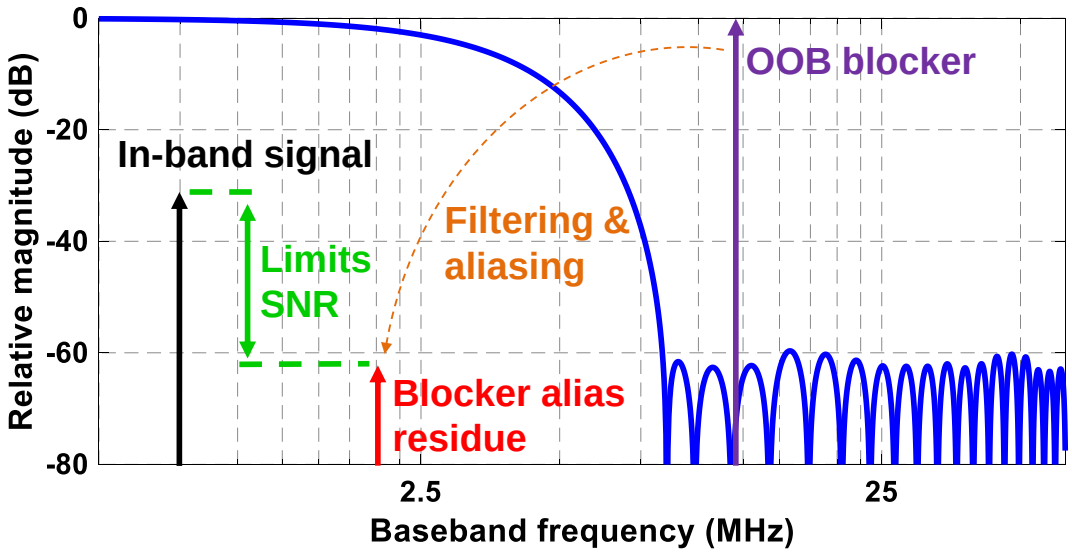

Figure 4.1: Illustration of the residual alias problem faced by the baseband FA filter with an f_s of 5 MHz.

rejection can be very large to attenuate any blockers with tradeoff against in-band droop and transition bandwidth. While such tradeoff may not be desirable, it at least is theoretically possible, just like a digital filter. However, in reality, the precision of $R(t)$ is finite and parasitics always kick in, even with the slice-based approach described in Chapter 3, whose feedback network's impedance is of less importance. This fundamentally suggests that the blocker rejection of an FA receiver is limited by and only by the FA filter itself unless pre-filtering is realized without degrading the FA filtering performance (recall that in Chapter 2 we have shown that pre-filtering may deteriorate the FA filtering if not done with care). In contrast, conventional or mixer-first receivers can be followed by subsequent baseband filtering stages to perform further filtering to achieve higher and higher rejection of unwanted signals at the expense of power and silicon area. Note that in both cases, blockers at harmonic frequencies of the LO will not be filtered unless a harmonic-rejection mixer is employed.

As mentioned in Section 2.5, such a problem for the transition band may be extenuated when an OSR > 1 is involved by intentionally using only part of the full bandwidth (rather than choosing a baseband passband BW to be half of the sampling rate) or employing time-interleaving if the sampling rate and BW need to remain the same. However, for the finite

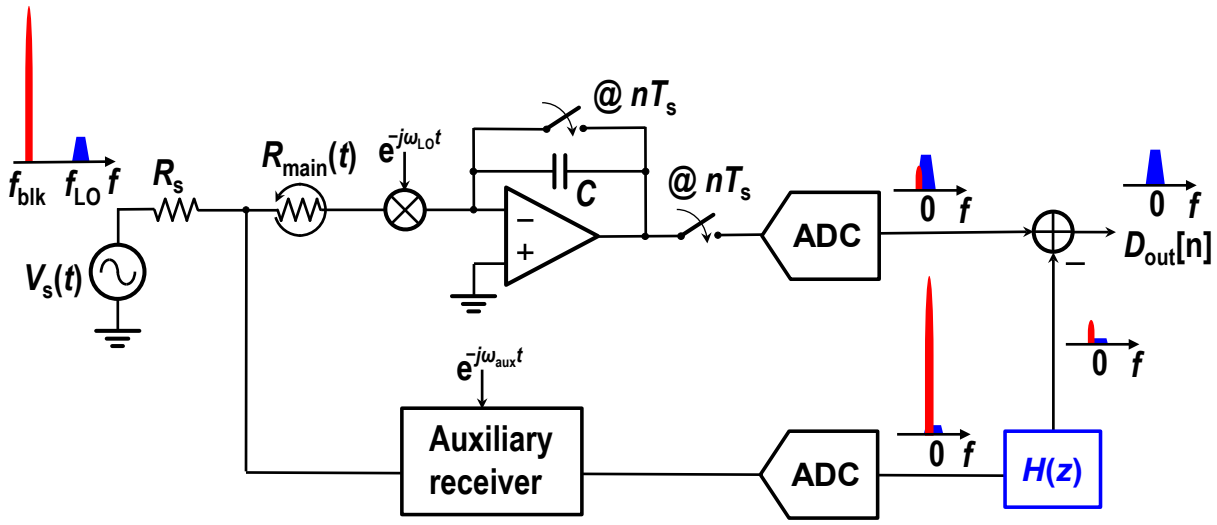

Figure 4.2: Illustration of the alias cancellation concept for an FA receiver.

and insufficient stopband rejection, even an OSR > 1 does not help and this is fundamental to the current FA filters. Therefore, to make FA receivers more practical, especially under the circumstances where strong blockers are present and not fully rejected by the FA stopband rejection, we propose an alias cancellation technique for further reducing the magnitude of the residual blocker alias even after it has been sampled.

4.3 DSP-Based Alias Cancellation

4.3.1 Concept of the Proposed Alias Cancellation Technique

The concept of the proposed alias cancellation technique is depicted in Fig. 4.2, where the main channel is the FA receiver centered at f_{LO} with $R_{\mathrm{main}}(t)$ and the auxiliary channel is another receiver centered at a frequency, f_{aux}, around the frequency of the blocker, f_{blk}. Note that f_{aux} is not necessary to be the same as the blocker frequency. Instead, it should be chosen to be a frequency at which the blocker will alias to the same baseband frequency as the main channel. In general, the auxiliary receiver can be any types of receivers, such as the mixer-first receiver [9] or even the spectrum scanner [17], as long as it is reasonably linear for the given blocker strength and does not mess up with the FA receiver's input impedance. In our setup, since the dual-channel receiver in Chapter 3 is readily available, we employ

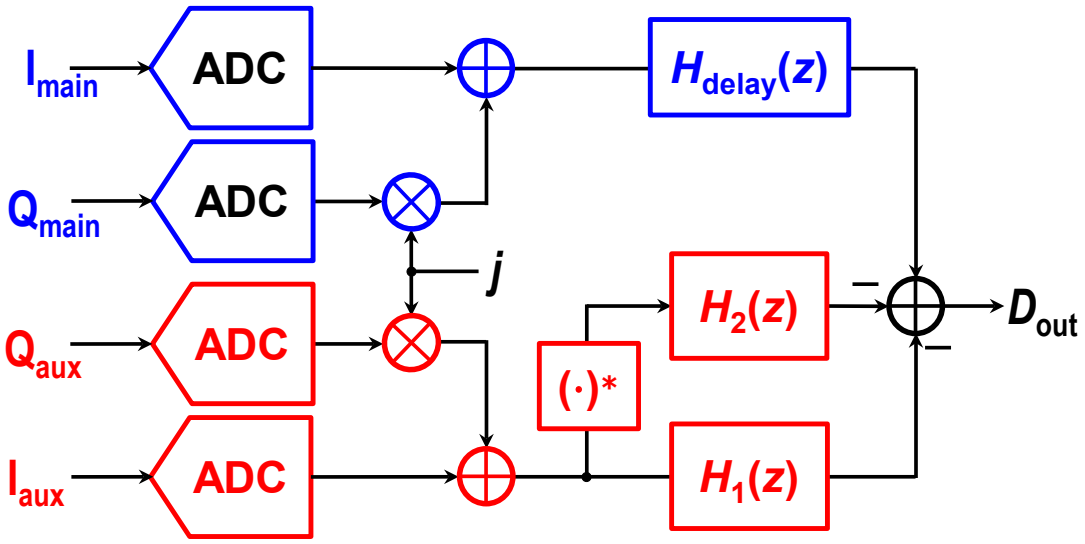

Figure 4.3: System overview of the alias cancellation block in the digital baseband [$(\cdot)^*$ is the complex conjugate operator].

this particular chip to demonstrate the alias cancellation technique as an example. In this specific setup, both receiver channels are FA receivers. The wanted signal will be around dc after frequency translation at the output of the main-path FA receiver. The blocker, albeit being attenuated significantly, will fold on top of the wanted signal at the main-path output. The auxiliary channel, on the other hand, captures the blocker, which land around dc at the auxiliary path's output. Note that as far as the auxiliary channel is concerned, the wanted signal is actually out-of-band, so it will be attenuated by the FA filter's stopband rejection and become slim. The digital filter $H(z)$ scales the signal at the output of the auxiliary path with proper magnitude and phase such that it generates an exact replica of the residual alias of the blocker in the main channel. Then by digitally subtracting the outputs of the main path and the digital filter, the residual alias of the blocker is canceled and the desired signal is untouched. The wanted signal not only goes through the FA filtering in the auxiliary channel but the scaling in $H(z)$, which is generally much smaller than unity, and hence the residual alias of the wanted signal from the auxiliary path will not pose an SNR problem.

The overall system for the proposed alias cancellation is shown in Fig. 4.3. I_{main}, Q_{main}, I_{main}, and Q_{main} are the I/Q outputs of the main and auxiliary receivers, respectively. After being digitized by four ADCs, they are correspondingly processed by in total one delay

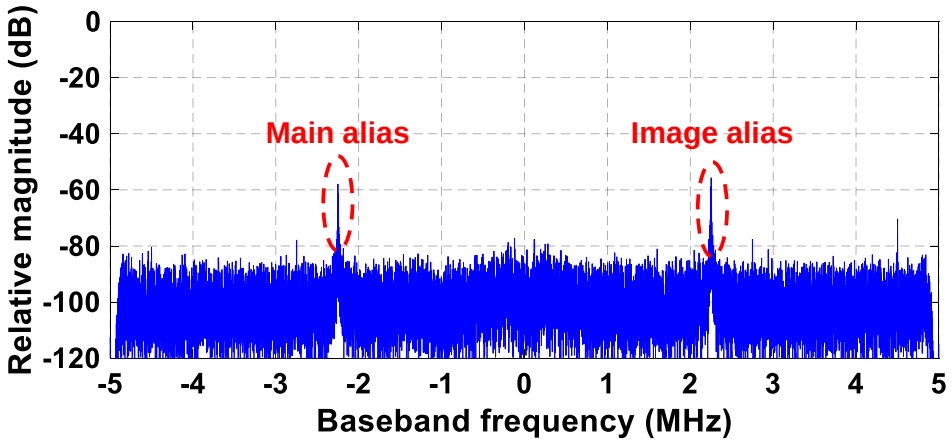

(a)

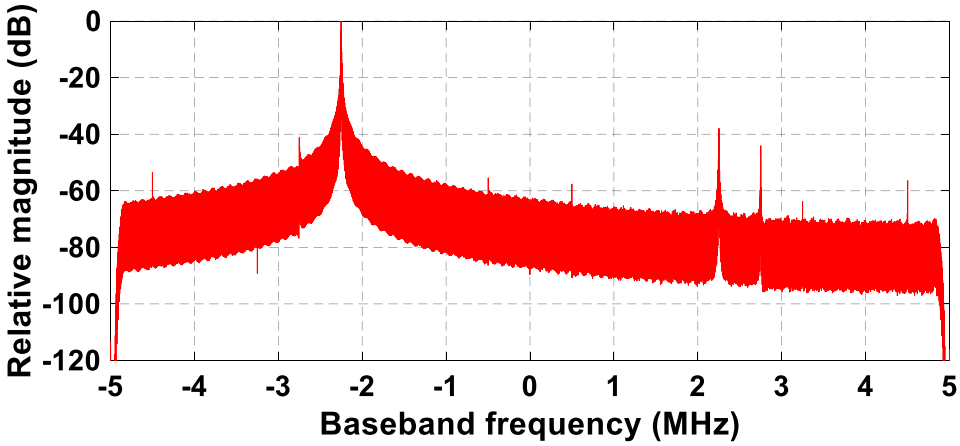

(b)

Figure 4.4: Measured baseband spectra at $f_{\mathrm{LO}} = 270$ MHz, $f_{\mathrm{aux}} = 350$ MHz, and $f_{\mathrm{s}} = 10$ MHz with a sinusoid at 347.75 MHz sent to the input of the receiver for (a) the main and (b) auxiliary channels.

element and two filters. The delay element simply adds a fixed group delay for equalization. The selection of this delay will be explained in Subsection 4.3.3. The first filter $H_1(z)$ is rather straightforward. It captures the blocker sensed by the auxiliary channel. Then, as illustrated conceptually in Fig. 4.2, the blocker needs to be properly scaled such that it becomes an exact replica of the residual alias in the main channel. $H_1(z)$ is the filter that scales the blocker. Since both magnitude and phase are needed, in this system, I/Q signals

are necessary. Fortunately, the chip in Chapter 3 inherently has I/Q channels, thanks to the N-path-based mixer. The second filter, on the other hand, is less intuitive. The need for $H_2(z)$ is because the residual alias also has an image at its opposite frequency. The cause of this image is due to the carrier being real, while the mixing is complex. An example can be used to elaborate this. If $f_{\mathrm{LO}} = 350$ MHz and the input signal, assuming it is a sinusoid, is at 271 MHz, which actually has two tones in the spectrum at ± 271 MHz, the two tones will be translated to -79 and -621 MHz. The former will alias to 1 MHz after the sampling operation at FA filter's output, while the latter will alias to -1 MHz. Both are in-band now, and both are filtered only by FA filtering, so these two aliases are defined by the FA filter shape in the stopband. For a wideband wanted signal that spans across the entire band, both aliases cause SNR degradation. Consequently, we need to cancel the image alias as well using the same approach as the main alias residue. The exact replica of this image residue is found by scaling the complex conjugate of the blocker from the auxiliary channel, which converts it to locate at the opposite baseband frequency. Then, subtracting the two filters' outputs with the main channel's output results in an ideally alias-free signal, D_{out}. Obtaining the complex conjugate is hardware-friendly, since a conjugate here simply means a negative sign for the Q channel.

Fig. 4.4 shows an example of the measured baseband spectrum when $f_{\mathrm{LO}} = 270$ MHz and $f_{\mathrm{aux}} = 350$ MHz with $f_{\mathrm{s}} = 10$ MHz using the chip in Chapter 3 with a sinusoid at 347.75 MHz sent to the receiver input. The auxiliary path clearly captures the blocker. While the main path shows an alias of the blocker, it also clearly shows an image of the blocker alias at the opposite frequency. Since these two tones have similar magnitude and either one of them may limit the SNR, the image alias also needs to be taken care of, thus the filter $H_2(z)$. The cancellation of these two aliases is the focus of this work.

4.3.2 Frequency Response Measurement

The required digital filters, $H_{1,2}(z)$, essentially equalize the blocker's strengths in the two channels, so it is critical to obtain the relative frequency responses between the two channels.

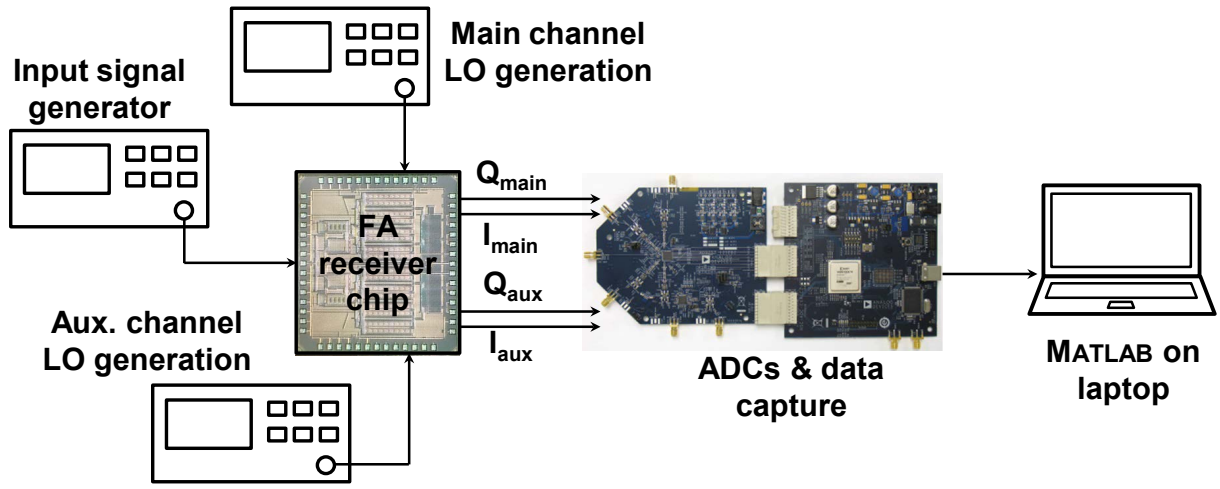

Figure 4.5: Measurement setup for accurately obtaining the effective frequency responses between the two channels (ignoring PCB and on-board buffers).

Since FA filters depend not only on the designed filter coefficients, i.e., $R(t)$ variation, but also on parasitics, $R(t)$ accuracy, and even timing, it is not easy to obtain the correct frequency responses accurately via analysis or simulation, especially under the presence of voltage and temperature variations (assuming process variation has been taken care of by calibration at startup).

Here, we resort to directly measure the frequency responses using signal generators to generate sinusoids and sweep the frequencies of the sinusoids to cover the band of interest. For now, we only talk about the filter for the main alias, $H_1(z)$, for the sake of brevity, so in the following descriptions, $H(z)$ represents $H_1(z)$. However, the other filter, $H_2(z)$ can be obtained in the same manner and we will summarize the procedures to obtain both in Subsection 4.3.3. The measurement setup is shown in Fig. 4.5, which is the same setup that obtained Fig. 4.4. We use AD9253 from Analog Devices [48] to perform conversation of analog signals to digital ones. The digital baseband signal at the output of the main channel is $V_{\mathrm{d,main}} = I_{\mathrm{d,main}} + jQ_{\mathrm{d,main}}$ and that of the auxiliary channel is $V_{\mathrm{d,aux}} = I_{\mathrm{d,aux}} + jQ_{\mathrm{d,aux}}$, where $I_{\mathrm{d,main}}$, $Q_{\mathrm{d,main}}$, $I_{\mathrm{d,aux}}$, and $Q_{\mathrm{d,aux}}$ are the digital versions of the sampled outputs of the receiver, I_{main}, Q_{main}, I_{aux}, and Q_{aux}, respectively. Considering that they are close resemblances of each other with small differences due to quantization error, which is true as AD9253 has an effective number of bit (ENOB) of about 12, the desired $H(j\Omega)$ at a

given baseband frequency of the input sinusoid (tone), Ω_{tone}, can be obtained by

$$H(j\Omega)|_{\Omega=\Omega_{\text{tone}}} \approx \tilde{H}(j\Omega)|_{\Omega=\Omega_{\text{tone}}} = \frac{G_{\text{main}}(j\Omega_{\text{tone}})}{G_{\text{aux}}(j\Omega_{\text{tone}})} = \frac{\hat{V}_{\text{d,main}}(j\Omega_{\text{tone}})}{\hat{V}_{\text{d,aux}}(j\Omega_{\text{tone}})} = \frac{\mathcal{F}[V_{\text{d,main}}](j\Omega_{\text{tone}})}{\mathcal{F}[V_{\text{d,aux}}](j\Omega_{\text{tone}})}, \tag{4.1}$$

where $-\pi \leq \Omega < \pi$, $\tilde{H}(j\Omega)$ is the measured relative frequency response, $G_{\text{main}}(j\Omega)$ and $G_{\text{aux}}(j\Omega)$ are the frequency responses of the main and auxiliary channels, respectively. Here, for easy notation, we ignore the frequency translation and assume we are dealing with just the baseband FA filters. In principle, if one can sweep the frequency of the input sinusoids indefinitely finely, the complete frequency response of $\tilde{H}(j\Omega)$ ranging from $-\pi$ to π can be obtained. However, it is impossible to measure all frequency points, which is infinite. Instead, we choose to sweep the frequency at a few points only and then obtain the filter coefficients.

4.3.3 Generation of the Digital Baseband Filters

In this work, we coarsely sweep the frequency of the sinusoidal input for $K = 20$ points within $-\pi$ to π to obtain a sampled version of $\tilde{H}(j\Omega)$, which is found by comparing the magnitude and phase of the measured sinusoids at the baseband of the two channels, according to (4.1). For our measurement shown in this Chapter, unless otherwise specified, the input signal power is about -10 dBm as a good compromise such that the residual alias in the main channel is well above the noise floor and the auxiliary channel remains reasonably linear. For a given sinusoid, we perform fast Fourier transform (FFT) on the digitized outputs, through which we find the peak in the spectrum of the auxiliary path, for which the blocker is in-band, to determine which FFT bin has most of the sinusoid's power. Then, the relative frequency response between the two channels at this particular frequency is found by dividing the frequency-domain component of the main channel by that of the auxiliary channel at this frequency bin, i.e., following (4.1). After finding the relative frequency response for K frequency points,we find the filter coefficients $h[n]$ by performing inverse FFT. The filter will be an FIR filter and inherently stable. Note that with 20 samples, the corresponding filter will only have 20 taps. While this may seem a little challenging when trying to minimize the

error between $H(j\Omega) = \mathcal{F}(h[n])$ and $\tilde{H}(j\Omega)$, our results insinuate that it in fact suffices, plus this also suggests very little hardware overhead. Since $\tilde{H}(j\Omega)$ is complex, the obtained digital filter $h[n]$ is also complex. The ADCs in our experiment ran at a higher rate than $f_{\rm s}$, and hence decimation was performed. While not necessarily required, a simple I/Q calibration was performed in the digital domain before FFT, considering the board was not designed for matching the I/Q output channels. Such I/Q correction, as seen from the magnitude of the image alias (recall Fig. 4.4 where this I/Q correction has already been applied), does not remove this alias and therefore the second filter is demanded. The decimation filter is slightly over-designed and hence a small portion of the spectrum at the higher end is filtered out. This, however, is not necessary and therefore not an issue.

Fig. 4.6 shows the measured relative frequency response for the main alias. From Fig. 4.6(a), we again see that the sideband rejection (effectively the measured $\tilde{H}(j\Omega)$ is the sideband rejection) is roughly the same as the filter floor, and from Fig. 4.4(b) we see that the phase is roughly linear and the overall phase change is rather small from $-\pi$ to π. It is observed that, when the baseband offset frequency is very close to dc, the relative magnitude of $\tilde{H}(j\Omega)$ is higher and the phase also has some jumps. This is most likely because the RF input impedance at LO frequencies is slightly different due to the equivalent Miller resistance of the integrating capacitor under periodical reset. We also notice that, since the phase shift from $-\pi$ to π is quite small except one point, which corresponds to very small group delay over most of the frequency range, a 20-tap digital filter will not be able to obtain such a delay. Fortunately, we are only interested in equalizing the two channels' frequency responses. Therefore, a constant group delay, $H_{\rm delay}(z) = z^{-K/4}$ with a magnitude of 0 dB, is added to $\tilde{H}(j\Omega)$ before FFT such that the overall group delay is roughly 10 samples for a 20-tap filter (the main path needs to add this delay as well for equalization, as shown in Fig. 4.3). Then with the MATLAB function `ifft`, we obtain the filter $h[n]$, or equivalently, $H(z)$.

To summarize, the steps to obtain the desired baseband digital filters for one of the channels in a two-channel FA receiver are the following.

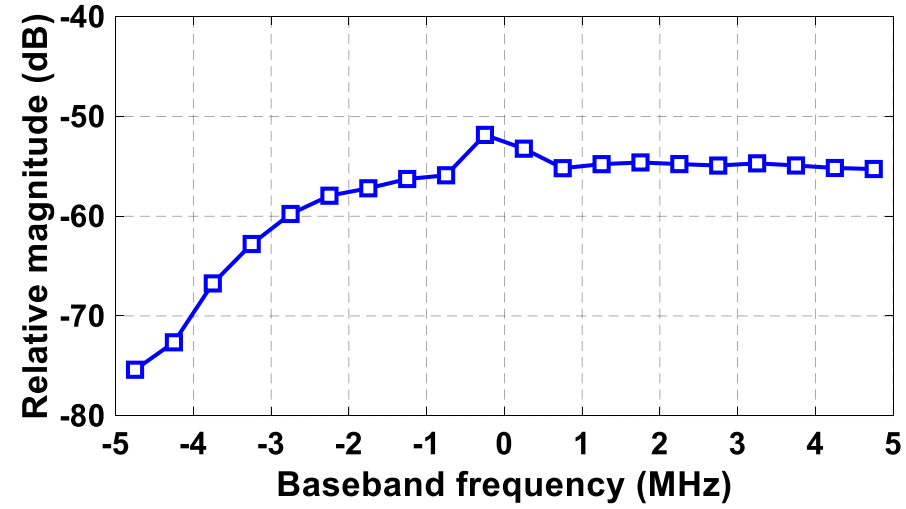

(a)

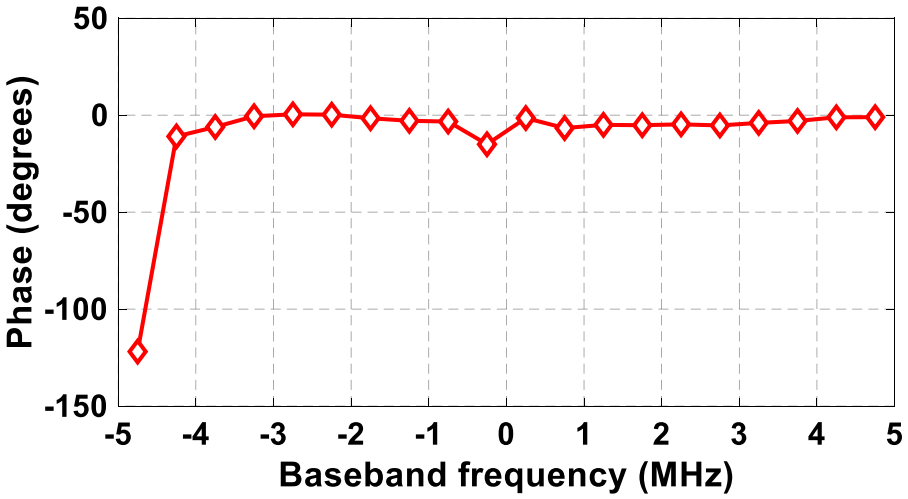

(b)

Figure 4.6: Measured baseband $\tilde{H}(j\Omega)$ with $f_{\mathrm{LO}} = 270$ MHz, $f_{\mathrm{aux}} = 350$ MHz, and $f_{\mathrm{s}} = 10$ MHz.

1. Place the two channels' LO frequencies at the desired signal's frequency and the anticipated blocker's frequency, respectively.

2. Send a sinusoid (tone) at one of the in-band frequencies of the auxiliary channel, which intends to pick up the blocker.

3. The FA receiver outputs 4 sets of data, I_{main}, Q_{main}, I_{aux}, and Q_{aux}. They are buffered

and then sent to 4 synchronized ADCs to obtain $I_{\mathrm{d,main}}$, $Q_{\mathrm{d,main}}$, $I_{\mathrm{d,aux}}$, and $Q_{\mathrm{d,aux}}$, which construct $V_{\mathrm{d,main}} = I_{\mathrm{d,main}} + jQ_{\mathrm{d,main}}$ and $V_{\mathrm{d,aux}} = I_{\mathrm{d,aux}} + jQ_{\mathrm{d,aux}}$.

4. Perform FFT on $V_{\mathrm{d,main}}$ and $V_{\mathrm{d,aux}}$, and find the frequency, Ω_{tone}, of the bin at which the spectrum reaches its maxima for the auxiliary path. Also perform FFT on the complex conjugate of $V_{\mathrm{d,aux}}$. Then four complex numbers are obtained: $\hat{V}_{\mathrm{d,aux}}(j\Omega_{\mathrm{tone}})$, $\hat{V}^*_{\mathrm{d,aux}}(-j\Omega_{\mathrm{tone}})$, $\hat{V}_{\mathrm{d,main}}(j\Omega_{\mathrm{tone}})$, and $\hat{V}_{\mathrm{d,main}}(-j\Omega_{\mathrm{tone}})$. The second one among these four is the frequency-domain component at $-\Omega_{\mathrm{tone}}$ for the complex conjugate of $V_{\mathrm{d,aux}}$, and the asterisk is the complex conjugate operator.

5. The relative frequency response for the main alias at this particular baseband frequency, $\tilde{H}_1(j\Omega_{\mathrm{tone}})$, is characterized by dividing $\hat{V}_{\mathrm{d,main}}(j\Omega_{\mathrm{tone}})$ by $\hat{V}_{\mathrm{d,aux}}(j\Omega_{\mathrm{tone}})$. For the image alias, we find $\tilde{H}_2(-j\Omega_{\mathrm{tone}}) = \hat{V}_{\mathrm{d,main}}(-j\Omega_{\mathrm{tone}})/\hat{V}^*_{\mathrm{d,aux}}(-j\Omega_{\mathrm{tone}})$.

6. Repeat Steps 2–5 for $(K-1)$ times until in total K samples of $\tilde{H}_1$ and $\tilde{H}_2$ are taken. The frequencies at which the tones are sent need to be at constant intervals and cover most of the band.

7. Add a delay of roughly $(K-1)/2$ samples to both $\tilde{H}_1$ and $\tilde{H}_2$.

8. Perform inverse FFT on $\tilde{H}_1$ and $\tilde{H}_2$ with the extra delay to obtain the filter coefficients $h_1[n]$ and $h_2[n]$.

The obtained $h_1[n]$ and $h_2[n]$ can be used as shown in Fig. 4.3 to obtain proper replicas of the residual aliases of the blocker for the main channel to cancel the corresponding aliases. Note that $h_1[n]$ is applied to the output of the auxiliary channel, while $h_2[n]$ needs to be used on the complex conjugate of that, just like how they are obtained in the first place.

4.4 Results and Discussions

For a setup using $f_{\mathrm{LO}} = 270$ MHz, $f_{\mathrm{aux}} = 350$ MHz, and $f_{\mathrm{s}} = 10$ MHz, we swept the input frequency within 10 MHz for 20 times starting from 345.25 MHz to 354.75 MHz with a step of 0.5 MHz to obtain $\tilde{H}_1$ and $\tilde{H}_2$, following the steps given in Subsection 4.3.3. Fig. 4.7 shows

the measured frequency responses, $\tilde{H}_1$ and $\tilde{H}_2$, and those of the two digital filters, $h_1[n]$ and $h_2[n]$. For easy comparison, the added extra phases (i.e., delays) in Step 7 given at the end of Subsection 4.3.3 are removed. Overall speaking, they match reasonably well, but the edges suffer from more deviations, because digital filters must have identical frequency responses at $-\pi$ and π, while an analog filter does not necessarily have this property even when its output is sampled. Fortunately, the difference is not too large, and even with a small OSR as long as it is larger than unity, such a problem can be mitigated. The mismatches at dc are also larger, but remain at an acceptable level. Besides, the aliases near dc are likely to be overwhelmed by flicker noise and offset, and hence less obvious.

In order to test the effectiveness of the alias cancellation, another set of data was collected, which contains also tones but at different frequencies. The input frequency of the test tones was swept from 345.5 MHz to 354.5 MHz with a step of 0.5 MHz, such that these frequencies are between the frequency points taken for obtaining $\tilde{H}_1$ and $\tilde{H}_2$. One example of comparing the output spectra for the signals at the output of the main channel before and after alias cancellation is shown in Fig. 4.8. In this particular case with an input frequency of 348.5 MHz, about 18-dB cancellation can be observed and both main and image aliases were canceled well. Fig. 4.9 compares the rejection of the main channel before and after alias cancellation for all test tones. Because the cancellation depends on how well the equalizing digital filters, $h_1[n]$ and $h_2[n]$, match the measured frequency responses, the alias cancellation was not always 18 dB as shown in Fig. 4.8. Specifically, at the band center, due to the impedance difference and hence larger filter mismatch, the cancellation was worse. While not obvious in this case, it will be shown later that the performance may be worse at the band edges as well because the matching at edges can be slightly worse as a consequence of digital filters needing to have the same frequency responses at $-\pi$ and π, as mentioned earlier. Nonetheless, an average cancellation of 14 dB was observed, which brings the overall rejection of the main channel from $\sim$55 dB to close to 70 dB for this measurement setup. Thanks to the alias cancellation, the blocker rejection for this band has effectively reached that of [19] and [28], which use time-interleaving while this work does not. It is worth noting that such improvement in the effective rejection is narrow-band, unlike [19] and [28], which

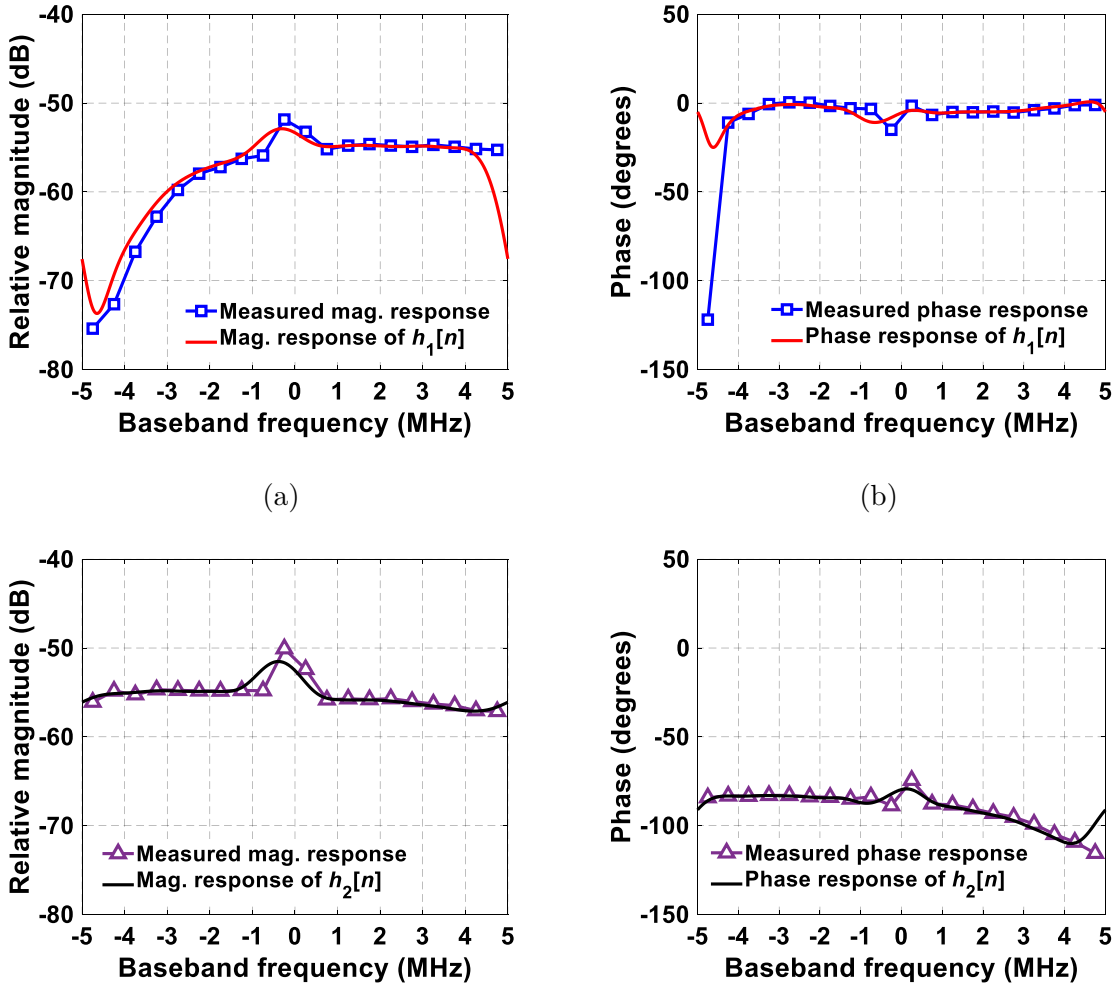

Figure 4.7: Comparison between the measured relative frequency responses between the two channels and those of the equalizing filters (no added artificial delay for easy comparison) in terms of (a) main alias' magnitude, (b) main alias' phase, (c) image alias' magnitude, and (d) image alias' phase.

have a high stopband rejection over a wide frequency range. However, as can be apparently seen from Figs. 4.8 and 4.9, this helps solve the residual alias problem faced by FA receivers to a good extent with only two 20-tap digital filters. It is anticipated that, with more complicated filter shapes, in terms of both magnitude and phase, the cancellation may suffer more, or more taps are needed.

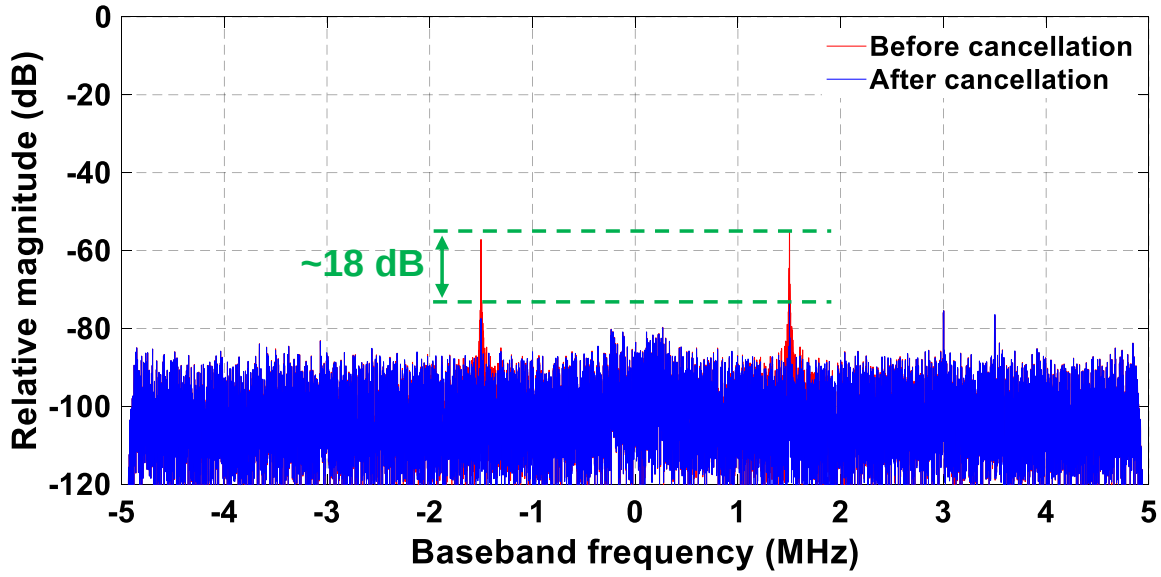

Figure 4.8: Measured baseband spectra at the output of the main channel with an input sinusoid at 348.5 MHz with $f_{\mathrm{LO}} = 270$ MHz, $f_{\mathrm{aux}} = 350$ MHz, and $f_{\mathrm{s}} = 10$ MHz before and after alias cancellation.

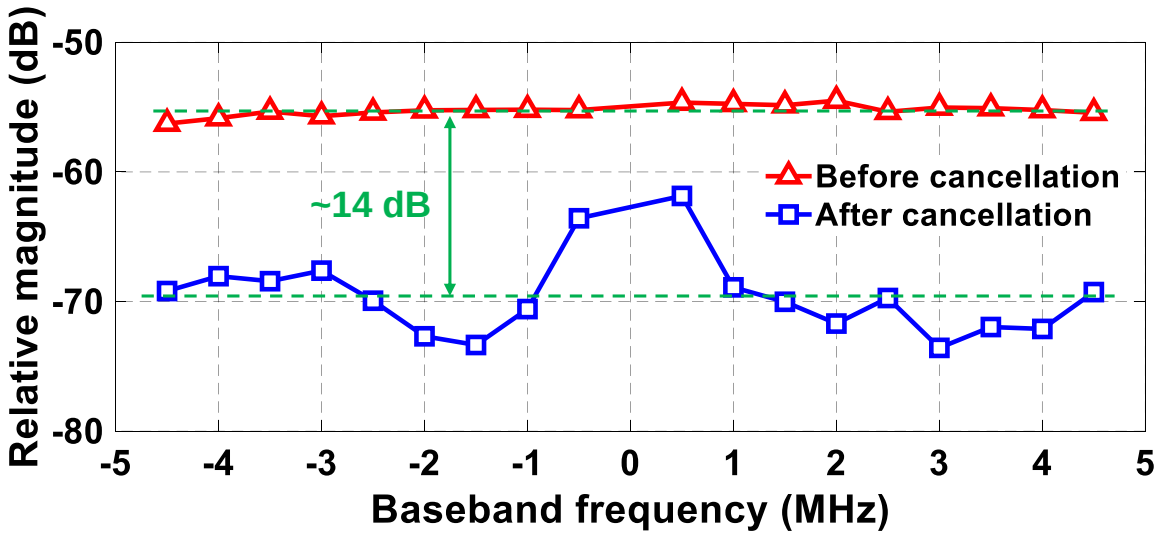

Figure 4.9: Measured rejection before and after cancellation using test tones.

Further, in addition to single-tone tests, a wideband signal has been sent to the receiver input and alias cancellation was performed to verify the effectiveness on wideband signals,

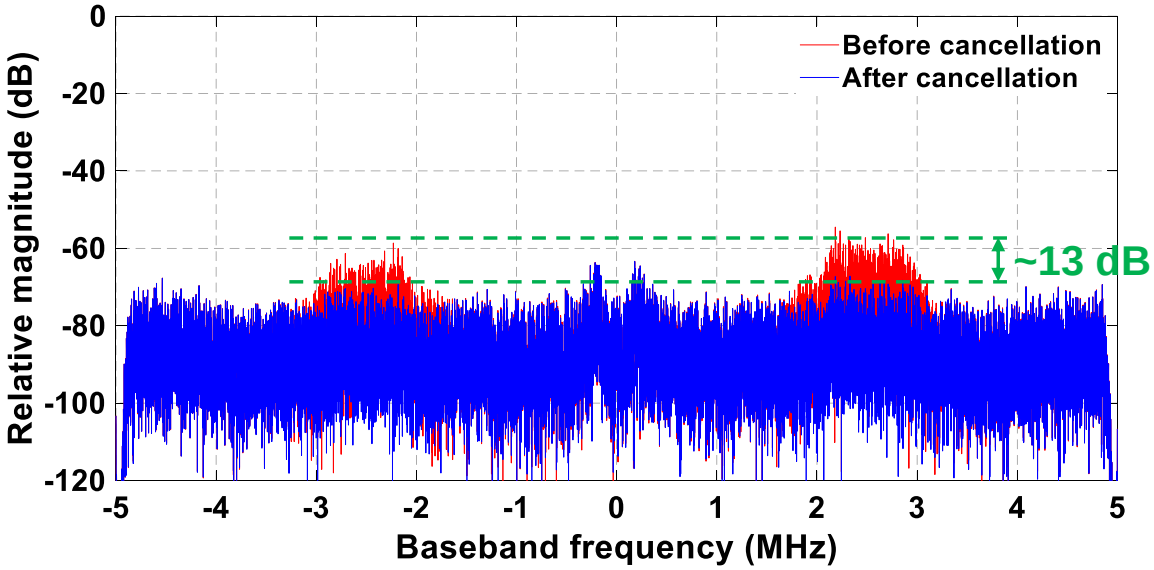

Figure 4.10: Measured spectra for a wideband phase-modulated blocker before and after cancellation.

which are more general. Due to limited access to equipment, a signal with simple phase modulation (PM) centered at 347.5 MHz was used for this measurement. Similar to the single-tone tests, the main and image aliases of the wideband signal were canceled successfully and the effective rejection was improved by about 13 dB, as can be found in the spectra in Fig. 4.10.

Another set of experiment was carried out for $f_{\text{aux}} = 270$ MHz and $f_{\text{LO}} = 350$ MHz. The input frequency of the measurement tones for generating the filters was swept from 265.25 MHz to 274.75 MHz with a step of 0.5 MHz. The measured frequency responses of the two filters and those of the digital baseband filters are shown in Fig. 4.11. The frequency responses show more mismatches at the band edges, as explained earlier. The deviation at dc still shows up as anticipated. The corresponding cancellation is illustrated in Fig. 4.12, where similar to the previous test, the test tones were swept from 265.5 MHz to 274.5 MHz with a step of 0.5 MHz such that they are at different frequencies from those used to generate the filters. The overall rejection was improved by 18 dB. Similar to Fig. 4.9, the cancellation was worsened at dc. Additionally, it can be observed that at the band edges (around $\pm\pi$,

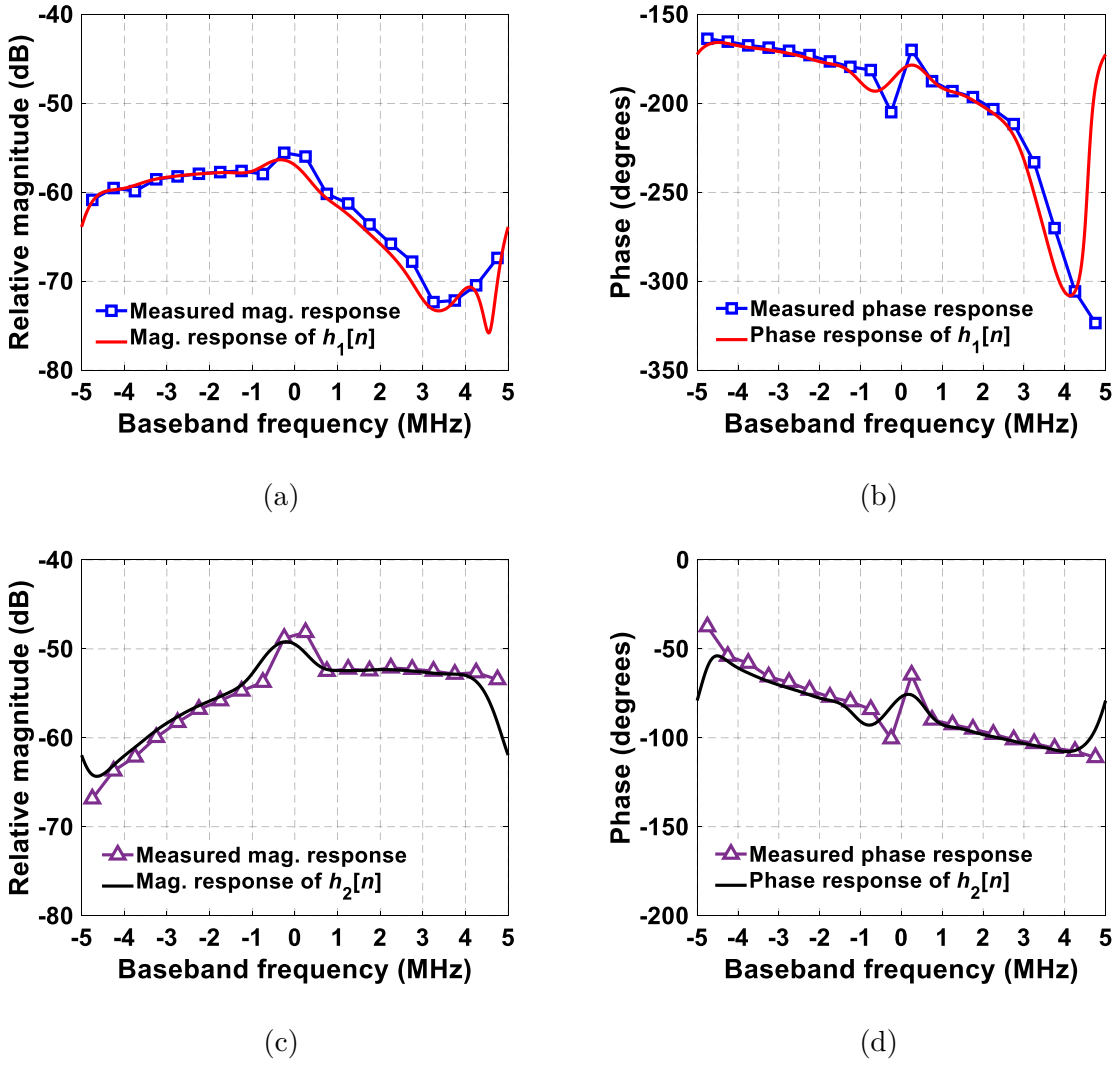

Figure 4.11: Comparison between the measured relative frequency responses between the two channels and those of the equalizing filters for $f_{\text{aux}} = 270$ MHz and $f_{\text{LO}} = 350$ MHz in terms of (a) main alias' magnitude, (b) main alias' phase, (c) image alias' magnitude, and (d) image alias' phase.

which are ± 5 MHz for this particular example), the cancellation was smaller, because of the mismatches of the frequency responses at band edges shown in Fig. 4.11.

So far we have demonstrated the cancellation of blockers, either a sinusoid or a wideband modulated signal, without the presence of an in-band signal in the main path. Using the setup with $f_{\text{aux}} = 270$ MHz and $f_{\text{LO}} = 350$ MHz, now we show the results with a small

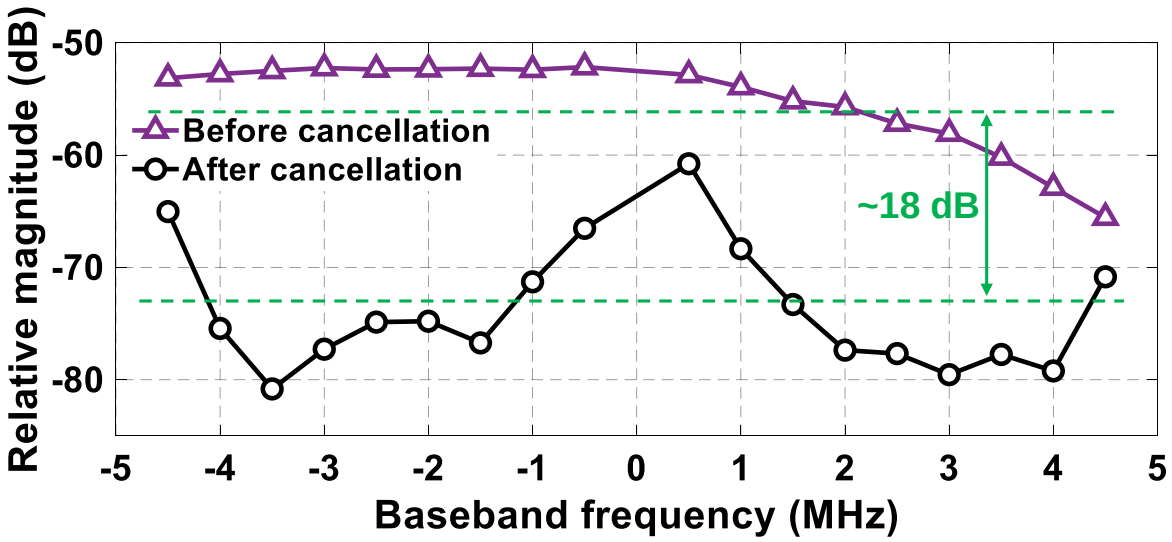

Figure 4.12: Measured rejection before and after cancellation using test tones for $f_{\text{aux}} = 270$ MHz and $f_{\text{LO}} = 350$ MHz.

sinusoid (-55 dBm) around the LO of the main path (347.5 MHz) and a wideband PM blocker at 272.5 MHz with -5-dBm power injected simultaneously to the receiver input (this set of data was collected at a different time from the previous ones). As can be seen from the spectra in Fig. 4.13, the FA filter greatly attenuated the blocker power, but after aliasing, the residual alias of the blocker was still observable and sat at the same frequency as the tonal signal. The alias cancellation technique effectively further suppressed the blocker by about 11 dB, while the signal was intact as depicted in the zoom-in view (the difference was less than 0.5 dB before and after cancellation). This demonstrates the alias cancellation technique for improving the effective SNR. The image of the signal itself was still present, and this is not canceled as it is outside the scope of this work. Digital image cancellation techniques are widely available [8] and hence this should not be a problem.

4.4.1 Alias Cancellation for All Channels

While it may seem that using an entire channel and thus doubling the power and area is a rather costly way to cancel the residual aliases of the blocker, this is not necessarily true. First, the second channel does not have to be a full receiver channel. Instead, any circuits

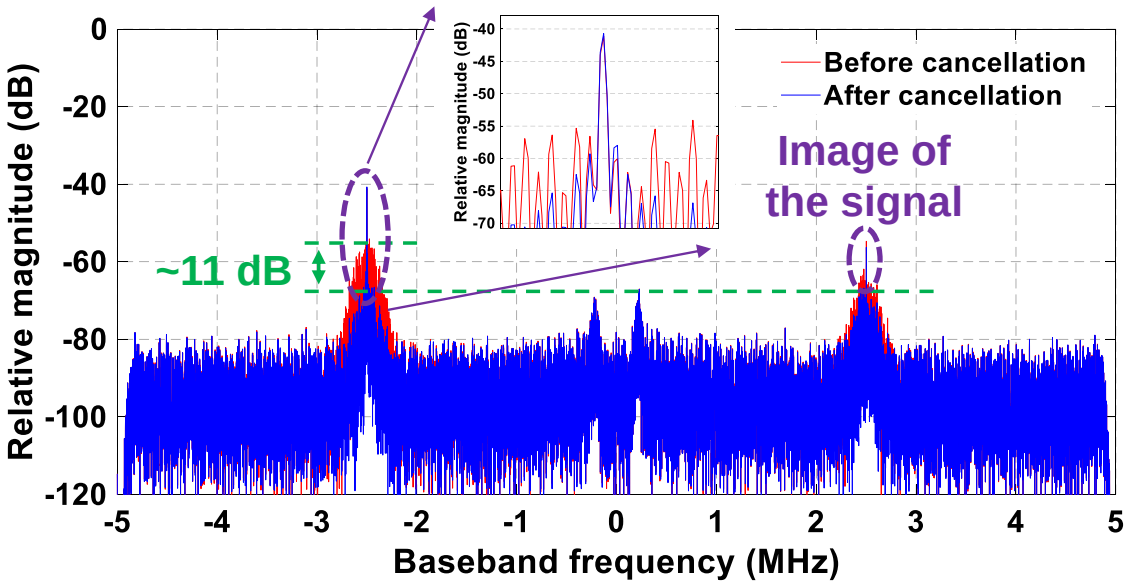

Figure 4.13: Measured spectra for a wideband phase-modulated blocker accompanied by an in-band signal before and after cancellation.

that can capture and downconvert the blocker can be used, which do not have to possess certain features that a receiver needs to, such as a matched input impedance (a high input impedance would still work well in parallel with the main-path receiver with 50-Ω input resistance) and low noise (it only needs to collect strong blockers and hence the noise figure can be high). It does need to provide reasonable in-band linearity and some programmability. The former is to avoid distortions dominating the captured data, and the latter is to be able to receive blockers at arbitrary frequencies, which is typical in a wireless environment. For example, the spectrum scanner in [17] can be a good candidate, which also has very low power consumption. Second, such alias cancellation can be applied to both channels. Effectively, this is increasing the sideband rejection for both channels. Fig. 4.14 shows the block diagram of the system, where $H_{m1}(z)$ and $H_{m2}(z)$ are the main and image alias filters, respectively, for the mth channel. As mentioned in Subsection 4.3.3, the conjugate operation is simply a sign inversion for the Q channel and hence not costly. For our current setup, the 4 filters will involve in total 80 taps, i.e., only 20 taps each. They operate at baseband rate, so they do not consume much power. The artificial delay, $z^{-K/4}$, is nothing but a few flip flops and

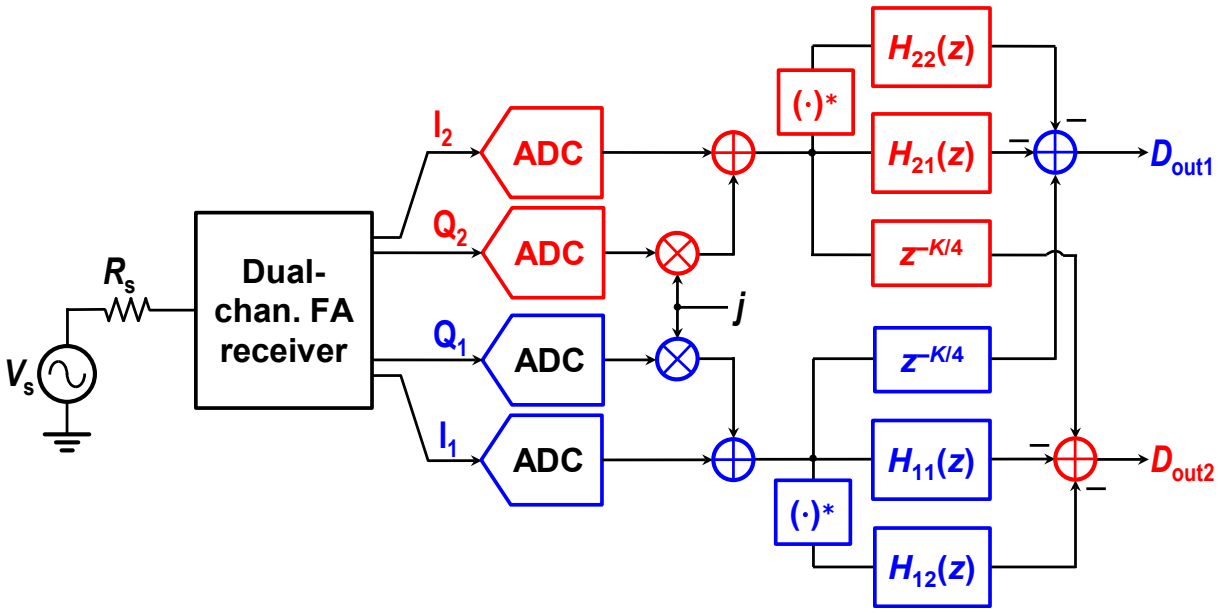

Figure 4.14: Simultaneous alias cancellation between the two channels (omitting I/Q calibration).

therefore cheap in terms of both power and hardware. Note that, while in our measurement, the ADCs ran at a higher rate than f_s and consequently decimation was required, it is not generally necessary. The ADCs can run at the same rate as the FA receiver output. In fact, if no intermediate buffering stages are needed, the sampling switch of an FA filter's output and that of the ADC's input can be merged as one. Therefore, in the block diagram in Fig. 4.14, we ignore decimation. The two outputs D_{out1} and D_{out2} are theoretically free from the aliases due to signals in each other's channel, similar to the case that we have so far described, where one dedicated channel is used for blocker collection only. This two-channel concurrent alias cancellation is beyond the scope of this work, and was not implemented, but should be straightforward to realize since everything in the digital domain is linearly processed. In practice, the best- and worst-case achievable cancellation is likewise limited by how well the digital filters match the actual relative frequency responses between the two channels plus how well the measured frequency responses hold against the variations of temperature and voltage.

In principle, such alias cancellation can also be applied to FA receivers with more than

two channels. The required hardware becomes more as well. Basically, for an M-channel FA receiver, if we desire every channel to be free from signals in all other channels, the total required number of filters is $2M(M-1)$. For a large M, it is approximately $2M^2$. Therefore, the cost in terms of hardware increases quadratically with the number of channels.

4.4.2 Known Limitations

As has been described at the end of Subsection 4.4.1, one limitation of the proposed alias cancellation technique is the required number of filters when the number of channels, M, is large. This may be relaxed by using the hybrid filter bank approaches [49], [50], but is beyond the scope of this work. Another limitation of the proposed alias cancellation scheme is that it relies on the precise knowledge of the relative frequency responses among channels. In the current approach, we are measuring them by sending tonal signals to the input of the receiver at startup and assuming that the filter responses do not change over time. However, because the frequency responses of FA filters heavily depend on the precision of $R(t)$ variation, parasitics, and timing, temperature and voltage variations will alter the frequency responses from time to time. This inevitably leads to inaccuracy of the measured frequency responses in a real-time application. Such foreground calibration of the digital baseband filters therefore has limited performance in the long run. Background calibration techniques that adaptively figure out the relative frequency responses over time will help in this regard, but come with much higher system complexity and possibly hardware and power overhead as well.

CHAPTER 5

Conclusion

This dissertation focuses on the design of wideband, programmable CMOS receiver front-ends using periodically time-varying circuits. More specifically, the filtering-by-aliasing (FA) technique has been employed as the primary means of realizing sharp filters. Enabling techniques were proposed in this dissertation to further extend the dynamic range of the FA receivers.

Chapter 2 presented a periodically time-varying noise cancellation technique for FA receivers. The key to the proposed technique is the use of a time-varying transconductance cell in an auxiliary path to sense the noise generated by the PTV resistor in an FA receiver. Through subtraction of the outputs of the main and auxiliary paths, noise of the PTV resistor is cancelled, while the sharp filtering offered by FA is well maintained. Weaker signals can be hence detected by the proposed receiver front-end. It is noteworthy that our theoretical study shows that, while conventional LTI noise cancellation can be employed in an FA receiver to null the PTV resistor's noise, it will also completely destroy the FA sharp filtering and render a first-order baseband filter with a sinc envelope on top of it, due to the sample-and-dump circuit used at baseband. A prototype IC fabricated in a 28-nm CMOS process shows that the noise figure is improvement by about 3 dB, while achieving over 67-dB stopband rejection with a transition BW of only four times the RF BW. A minimum in-band NF of 3.2 dB and an average in-band NF of 4.2 dB are demonstrated. With an upfront N-path filter to further enhance the linearity, the measured out-of-band IIP_3 is +18 dBm and the blocker 1-dB compression point is +9 dBm. Comparably, the out-of-band linearity is preserved well by introducing the NPF that helps the NC path better handle the OOB blockers, while in-band linearity is worsened due to the presence of active devices at

RF. The whole chip, including digital control circuitry, operates under a 0.9-V supply, while consuming 61-mW power at 500-MHz LO.

Chapter 3, on the other hand, described an FA receiver front-end based on a slice-based time-varying architecture. The architecture renders a time-invariant input impedance while the operation is still time-varying, leading to sharp analog FIR filtering with multiple benefits, such as tolerance to the reactance at the RF node. The time-invariant input impedance enables multi-channel operation and eliminates potential filter degradation due to interactions among different channels. The slice-based architecture also moves all transistor switches within a negative feedback loop to suppress the impact of the switch nonlinearities and parasitics on filter performance. A proof-of-concept two-channel prototype IC has been fabricated in a 28-nm CMOS process and demonstrates 50-dB stopband rejection, a transition BW of only 3.2 times the RF BW, an out-of-band IIP_3 of +35 dBm, a blocker 1-dB compression point of +12 dBm, and an LO leakage power better than −81 dBm, all from a 0.9-V supply voltage. With much higher linearity (∼10-dB higher IIP_3 than prior FA receivers), larger signals can be tolerated by the proposed receiver front-end without causing performance-degrading distortions. Its compatibility with carrier aggregation further enhances the throughput. Notably, compared with prior programmable receivers that support carrier aggregation, this work has close to 20-dB improvement on IIP_3 and 8-dB improvement on blocker 1-dB compression point. However, the downside is that the noise figure is a few dB higher as well. Thankfully, a low-noise mode is added to help extenuate this. In addition, this problem can be further alleviated by employing an LNA with a bypass switch, e.g., [51], of which the bypass switch itself has an IIP_3 larger than +55 dBm. Similar to enabling the LN mode, a blocker detector [47] or a spectrum scanner [17] can be used to determine whether the LNA should be enabled or bypassed. With such an LNA, the NF of the overall system is expected to be as low as ∼3.5–4 dB when no blockers are present and back to ∼14 dB when a 0-dBm CW blocker exists (ignoring the insertion loss of the bypass switch of the LNA).

Finally, Chapter 4 introduced a DSP-based alias cancellation technique tailored for FA receivers. In an FA receiver, due to the finite rejection, strong blockers' residual aliases

may still cause low SNR when the wanted signal is small. A second receiver is used to capture the blocker. With the blocker and the blocker aliases known, the only unknown is the relative frequency responses between the two receiver channels. By measuring the frequency responses of the two channels using sinusoids with swept frequencies, the relative magnitude and phase information between the two channels can be obtained, which is used to construct baseband digital filters for cancellation of the aliases. Using the dual-channel FA receiver chip fabricated in Chapter 3 and off-the-shelf ADCs together with the proposed alias cancellation algorithm implemented in MATLAB, we have successfully demonstrated the proposed technique and the measured rejection has on average been increased by about 15 dB for the blockers around the second channel's LO frequency. This work helps mitigate the residual alias problem faced by FA receivers, while in the past FA works, once the blockers alias within the band, they cannot be further reduced.

APPENDIX A

Generalized Noise Analysis for Baseband FA Filters

In this Appendix, we present a generalized analysis to calculate the noise factor contribution from each circuit component. The fundamental principles are the same as in [18], but more general.

For a particular noise voltage, $V_{\rm n}(t)$, consider it goes through an equivalent baseband filter by multiplying $V_{\rm n}(t)$ with a periodically time-varying conductance, $D_{\rm n}(t)$, and then integrating the current with a capacitor C. The equivalent model is depicted in Fig. A.1. The sampled output becomes

$$V_{\rm out}[n] = \int_{t=(n-1)T_{\rm s}}^{nT_{\rm s}} \frac{V_{\rm n}(t)D_{\rm n}(t)}{C} dt, \tag{A.1}$$

from which the autocorrelation of the output voltage samples, $R_{\rm oo}[m,n]$, can be calculated. As $D_{\rm n}(t)$ is periodic with a period of $T_{\rm s}$, $R_{\rm oo}[m,n]$ is wide-sense stationary and is given by [18]

$$\begin{aligned} R_{\rm oo}[m,n] &= R_{\rm oo}[m-n] = R_{\rm oo}[l] = E[V_{\rm out}[m]V_{\rm out}[n]] \\ &= E\left[\frac{1}{C^2}\int_{t_1=(m-1)T_{\rm s}}^{mT_{\rm s}}\int_{t_2=(n-1)T_{\rm s}}^{nT_{\rm s}} V_{\rm n}(t_1)V_{\rm n}(t_2)\times D_{\rm m}(t_1)D_{\rm n}(t_2)dt_1dt_2\right], \end{aligned} \tag{A.2}$$

where $D_{\rm m}(t)$ and $D_{\rm n}(t)$ are the time-varying conductances for $V_{\rm out}[m]$ and $V_{\rm out}[n]$, respectively. For non-TI-FA, they are identical, but for TI-FA, as will be shown later, they are not necessarily the same. If we assume the noise source to be white Gaussian with autocorrelation

$$R_{\rm nn}(t_1,t_2) = E[V_{\rm n}(t_1)V_{\rm n}(t_2)] = 2kTR_{\rm n}(t_1)\delta(t_1-t_2), \tag{A.3}$$

where k is the Boltzmann constant, T is the temperature in Kelvin, and $\delta(\cdot)$is the Dirac delta function, then we find that (A.2) can be expressed as

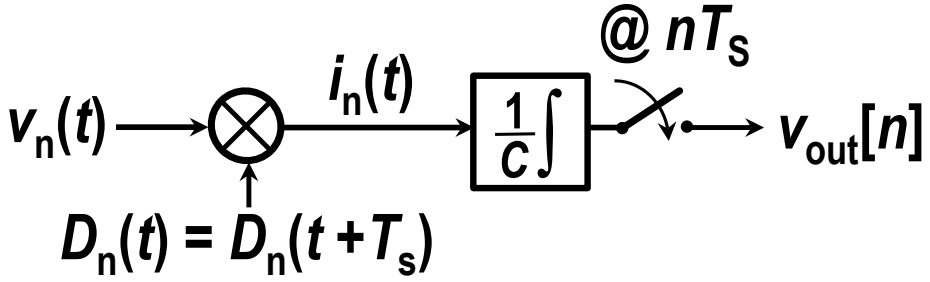

Figure A.1: Model for a general noise source $V_{\rm n}(t)$.

$$R_{\rm oo}[l] = \frac{2kT}{C^2} \int_{t_1=(m-1)T_{\rm s}}^{mT_{\rm s}} \int_{t_2=(n-1)T_{\rm s}}^{nT_{\rm s}} R_{\rm n}(t_1) D_{\rm m}(t_1) D_{\rm n}(t_2) dt_1 dt_2, \tag{A.4}$$

which for the non-TI case can be simplified into

$$R_{\rm oo}[0] = \frac{2kT}{C^2} \int_{t=0}^{T_{\rm s}} R_{\rm n}(t) [D(t)]^2 dt, \tag{A.5}$$

and $R_{\rm oo}[l] = 0$ when $l \neq 0$. The only remaining unknown factor $D(t)$ can be found with the equivalent models like Fig. 2.4(c) using simple KCL/KVL analyses. From (A.5), the overall output noise voltage autocorrelation can be easily computed with superposition since the noise sources, i.e., $R_{\rm s}$, $R(t)$, and $G_{\rm m}(t)$, are independent. For the circuit in Fig. 2.4(a), we consider the noise sources to be white Gaussian with autocorrelations

$$\begin{aligned} R_{\rm ss}(t_1, t_2) &= E[V_{\rm s}(t_1) V_{\rm s}(t_2)] = 2kTR_{\rm s}\delta(t_1 - t_2), \\ R_{\rm nRnR}(t_1, t_2) &= E[V_{\rm nR}(t_1) V_{\rm nR}(t_2)] = 2kTR(t_1)\delta(t_1 - t_2). \end{aligned} \tag{A.6}$$

By inspecting Figs. 2.4(b) and 2.4(c), we can find that for the noise from $R_{\rm s}$, $D(t) = (1+k_1/k_2)/[R(t)+R_{\rm s}]$, and for the noise from $R(t)$, $D(t) = -\{1-k_1R_{\rm s}/[k_2R(t)]\}/[R_{\rm s}+R(t)]$. Then the overall autocorrelation can be given by

$$R_{\rm oo}[0] = \frac{2kT}{C^2} \int_{t=0}^{T_{\rm s}} \frac{R_{\rm s}(1+k_1/k_2)^2}{[R_{\rm s}+R(t)]^2} dt + \frac{2kT}{C^2} \int_{t=0}^{T_{\rm s}} \frac{R(t)\{1-k_1R_{\rm s}/[k_2R(t)]\}^2}{[R_{\rm s}+R(t)]^2} dt, \tag{A.7}$$

and $R_{\rm oo}[0] = 0$ when $l \neq 0$. The corresponding PSD can be found

$$S_{\rm oo}(e^{j\omega}) = R_{\rm oo}[0]. \tag{A.8}$$

By dividing (A.7) by its first term, which is the source noise seen at the output of the filter, we obtain (2.4) after simplification.

Considering the noise from the $G_{\mathrm{m}}(t)$ cell is simple too, which is considered to have an input-referred noise with autocorrelation [as $G_{\mathrm{m}}(t) = k_1/R(t)$]

$$R_{\mathrm{GmGm}}(t_1, t_2) = E[V_{\mathrm{Gm}}(t_1)V_{\mathrm{Gm}}(t_2)] = \frac{2kT\gamma R(t_1)\delta(t_1 - t_2)}{k_1}, \tag{A.9}$$

and the corresponding $D(t) = G_{\mathrm{m}}(t)/k_2 = k_1/[k_2R(t)]$. This leads to

$$S_{\mathrm{oo}}(e^{j\omega}) = R_{\mathrm{oo}}[0] = \frac{2kT}{C^2}\int_{t=0}^{T_{\mathrm{s}}} \frac{\gamma k_1}{k_2^2 R(t)}dt. \tag{A.10}$$

Dividing (A.10) with the first term in (A.7) leads to (2.8), which is the noise factor that $G_{\mathrm{m}}(t)$ contributes.

Extending (A.4) to TI-FA is the same with an exception of $R_{\mathrm{oo}}[l] \neq 0$ for some non-zero l. Ignoring the NPF, PTV-NC with TI can be simplified into Fig. A.2 (mixer is omitted for baseband noise calculation), similar to Fig. 2.4. Here $G_{\mathrm{m1}}(t) = k_1/R(t)$ and $G_{\mathrm{m2}}(t) = k_1/R(t - T_{\mathrm{s}})$. Consider the noise from $R(t)$, $V_{\mathrm{nR1}}(t)$, with an autocorrelation of $2kTR(t_1)\delta(t_1 - t_2)$, (A.4) can be re-written into

$$R_{\mathrm{oo}}[l] = \begin{cases} \frac{2kT}{C^2}\int_{t=0}^{2T_{\mathrm{s}}} R(t)[D_0(t)]^2 dt & l = 0 \\ \frac{2kT}{C^2}\int_{t=0}^{T_{\mathrm{s}}} R(t)D_0(t)D_1(t)dt & l = \pm 1 \\ 0 & \text{else} \end{cases} \tag{A.11}$$

where the corresponding time-varying conductances, $D_0(t)$ and $D_1(t)$, can be again found by building equivalent models for the output samples similar to Fig. 2.4(c). They are given by

$$\begin{aligned} D_0(t) &= \frac{\lambda R_{\mathrm{s}}||R(t - T_{\mathrm{s}})/R(t) - 1}{R(t) + R_{\mathrm{s}}||R(t - T_{\mathrm{s}})} && \text{for } V_{\mathrm{out}}[2n] \\ D_1(t) &= \frac{(1 + \lambda)R_{\mathrm{s}}||R(t - T_{\mathrm{s}})}{R(t - T_{\mathrm{s}}) \times [R(t) + R_{\mathrm{s}}||R(t - T_{\mathrm{s}})]} && \text{for } V_{\mathrm{out}}[2n \pm 1] \end{aligned} \tag{A.12}$$

Substituting (A.12) with $\lambda = 0$, i.e., without NC, into (A.11) gives exactly the last term of (9) in [19]. Noises from other sources can be computed the same way, and the noise factor with NC can be calculated by taking the Fourier transform of $R_{\mathrm{oo}}[l]$ after considering all noise

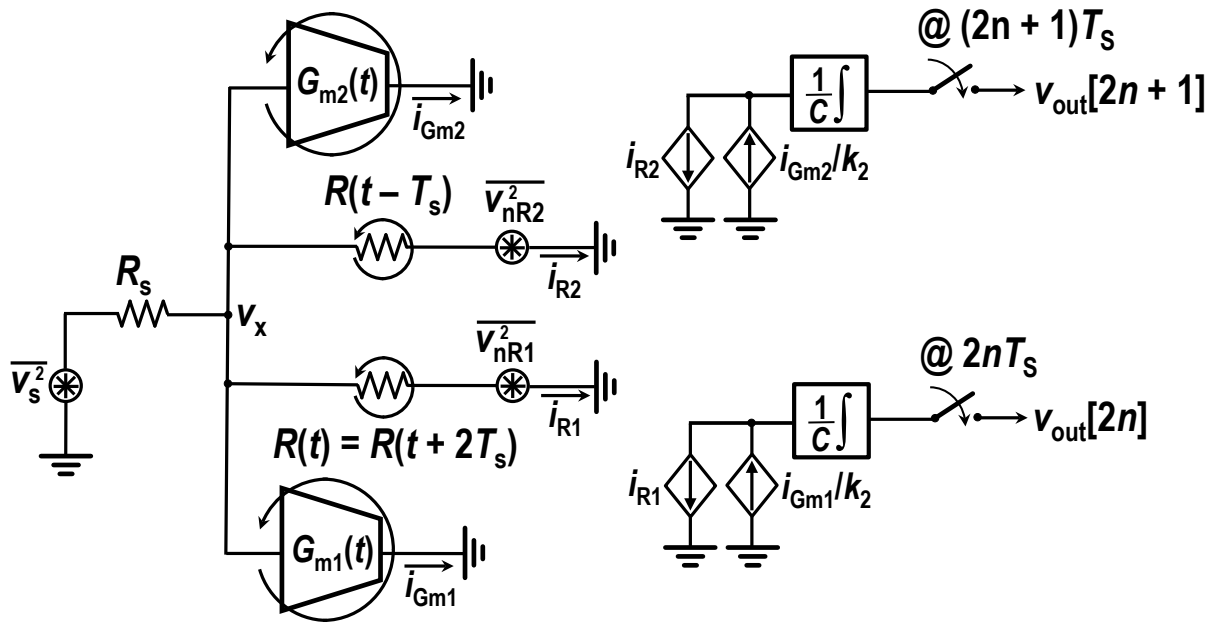

Figure A.2: Simplified model for calculating $D_{\mathrm{n}}(t)$ for PTV-NC with TI (ignoring $G_{\mathrm{m1,2}}(t)$'s noise).

sources to obtain the PSD with proper λ. As for the two G_{m} cells' noises, the corresponding autocorrelations of output voltages are single-tap, since the noise from $G_{\mathrm{m1}}(t)$ [or $G_{\mathrm{m2}}(t)$] only appears in its own path and is uncorrelated with the other one's noise. The resultant NF due to them is flat across the band. It can be calculated the same way as the non-TI case.

REFERENCES

[1] "Evolved universal terrestrial radio access (E-UTRA); physical channels and modulation (release 14)," *Tech. Rep. 36.211 (v14.2.0)*, 3rd Generation Partnership Project (3GPP), 2017.

[2] A. B. Flores, R. E. Guerra, E. W. Knightly, P. Ecclesine, and S. Pandey, "IEEE 802.11af: a standard for TV white space spectrum sharing," *IEEE Commun. Mag.*, vol. 51, no. 10, pp. 92–100, Oct. 2013.

[3] S. Hameed, "Design and analysis of programmable receiver front-ends based on LPTV circuits," Ph.D. dissertation, Depart. Elect. Comput. Eng., Univ. California, Los Angeles, CA, 2017.

[4] J. Mitola, "The software radio architecture," *IEEE Commun. Mag.*, vol. 33, no. 5, pp. 26–38, May 1995.

[5] B. Murmann, "ADC performance survey 1997–2021," 2021. [Online]. Available: http://web.stanford.edu/∼murmann/adcsurvey.html.

[6] A. A. Abidi, "The path to the software-defined radio receiver," *IEEE J. Solid-State Circuits*, vol. 42, no. 5, pp. 954–966, May 2007.

[7] "3rd-generation partnership project; technical specification group radio access network; further advancements for E-UTRA; physical layer aspects (release 9)," *Tech. Rep. 36.814 (v0.4.1)*, 3rd Generation Partnership Project (3GPP), 2009.

[8] S.-C. Hwu and B. Razavi, "An RF receiver for intra-band carrier aggregation," *IEEE J. Solid-State Circuits*, vol. 50, no. 4, pp. 946–961, Apr. 2015.

[9] C. Andrews and A. C. Molnar, "A passive mixer-first receiver with digitally controlled and widely tunable RF interface," *IEEE J. Solid-State Circuits*, vol. 45, no. 12, pp. 2696–2708, Dec. 2010.

[10] D. Murphy, H. Darabi, A. Abidi, A. A. Hafez, A. Mirzaei, M. Mikhemar, and M.-C. F. Chang, "A blocker-tolerant, noise-cancelling receiver suitable for wideband wireless applications," *IEEE J. Solid-State Circuits*, vol. 47, no. 12, pp. 2943–2963, Dec. 2012.

[11] A. Ghaffari, E. A. M. Klumperink, M. C. M. Soer, and B. Nauta, "Tunable high-Q N-path band-pass filters: Modeling and verification," *IEEE J. Solid-State Circuits*, vol. 46, no. 5, pp. 998–1010, May 2011.

[12] M. Darvishi, R. van der Zee, and B. Nauta, "Design of active N-path filters," *IEEE J. Solid-State Circuits*, vol. 48, no. 12, pp. 2962–2976, Dec. 2013.

[13] E. A. Klumperink, H. J. Westerveld, and B. Nauta, "N-path filters and mixer-first receivers: A review," in *Proc. IEEE Custom Integr. Circuits Conf. (CICC)*, Austin, TX, Apr./May 2017, pp. 1–8.

[14] Y. Xu and P. R. Kinget, "A switched-capacitor RF front end with embedded programmable high-order filtering," *IEEE J. Solid-State Circuits*, vol. 51, no. 5, pp. 1154–1167, May 2016.

[15] M. Tohidian, I. Madadi, and R. B. Staszewski, "A fully integrated discrete-time superheterodyne receiver," *IEEE Trans. VLSI Syst.*, vol. 25, no. 2, pp. 635–647, Feb. 2017.

[16] M. Rachid, S. Pamarti, and B. Daneshrad, "Filtering by aliasing," *IEEE Trans. Signal Process.*, vol. 61, no. 9, pp. 2319–2327, May 2013.

[17] N. Sinha, M. Rachid, S. Pavan, and S. Pamarti, "Design and analysis of an 8 mW, 1 GHz span, passive spectrum scanner with >+31 dBm out-of-band IIP3 using periodically time-varying circuit components," *IEEE J. Solid-State Circuits*, vol. 52, no. 8, pp. 2009–2025, Aug. 2017.

[18] S. Hameed and S. Pamarti, "Design and analysis of a programmable receiver front end based on baseband analog-FIR filtering using an LPTV resistor," *IEEE J. Solid-State Circuits*, vol. 53, no. 6, pp. 1592–1606, Jun. 2018.

[19] ——, "Design and analysis of a programmable receiver front end with time-interleaved baseband analog-FIR filtering," *IEEE J. Solid-State Circuits*, vol. 53, no. 11, pp. 3197–3207, Nov. 2018.

[20] R. Chen and H. Hashemi, "Reconfigurable receiver with radio-frequency current-mode complex signal processing supporting carrier aggregation," *IEEE J. Solid-State Circuits*, vol. 50, no. 12, pp. 3032–3046, Dec. 2015.

[21] A. A. M. Youssef, E. A. S. A. Ghany, and L.-C. Chang, "Carrier aggregation amplifier with dual gain control," U.S. Patent 9 479 131B2, Oct. 2016.

[22] A. Hadji-Abdolhamid, B. Pregardier, and M. Kahrizi, "Receiver for carrier aggregation," U.S. Patent 9 553 615B2, Jan. 2017.

[23] A. M. Tasic, C. Narathong, C. Holenstein, D. Pan, Y. Tang, R. Rangarajan, and L. K. Leung, "Multiplex modules for carrier aggregation receivers," U.S. Patent 9 774 485B2, Sep. 2017.

[24] J. Zhu and P. R. Kinget, "Frequency-translational quadrature-hybrid receivers for very-low-noise, frequency-agile, scalable inter-band carrier aggregation," *IEEE J. Solid-State Circuits*, vol. 51, no. 12, pp. 3137–3151, Dec. 2016.

[25] M. Nekovee, "Cognitive radio access to TV white spaces: Spectrum opportunities, commercial applications and remaining technology challenges," in *Proc. IEEE Symp. New Front. Dyn. Spect. (DySPAN)*, Apr. 2010, pp. 1–10.

[26] F. Bruccoleri, E. Klumperink, and B. Nauta, "Wide-band CMOS low-noise amplifier exploiting thermal noise canceling," *IEEE J. Solid-State Circuits*, vol. 39, no. 2, pp. 275–282, Feb. 2004.

[27] S. Bu, S. Hameed, and S. Pamarti, "An LPTV noise cancellation technique for a 0.9-V filtering-by-aliasing receiver front-end with >67-dB stopband rejection," in *Proc. IEEE Custom Integr. Circuits Conf. (CICC)*, Austin, TX, Apr. 2019, pp. 1–4.

[28] ——, "Periodically time-varying noise cancellation for filtering-by-aliasing receiver front ends," *IEEE J. Solid-State Circuits*, vol. 56, no. 3, pp. 928–939, Mar. 2021.

[29] S. Hameed and S. Pamarti, "Impedance matching and reradiation in LPTV receiver front-ends: An analysis using conversion matrices," *IEEE Trans. Circuits Syst. I, Reg. Papers*, vol. 65, no. 9, pp. 2842–2855, Sep. 2018.

[30] Y.-C. Lien, E. A. M. Klumperink, B. Tenbroek, J. Strange, and B. Nauta, "High-linearity bottom-plate mixing technique with switch sharing for N-path filters/mixers," *IEEE J. Solid-State Circuits*, vol. 54, no. 2, pp. 323–335, Feb. 2019.

[31] S. Hameed, M. Rachid, B. Daneshrad, and S. Pamarti, "Frequency-domain analysis of N-path filters using conversion matrices," *IEEE Trans. Circuits Syst. II, Exp. Briefs*, vol. 63, no. 1, pp. 74–78, Jan. 2016.

[32] ——, "Frequency-domain analysis of a mixer-first receiver using conversion matrices," in *Proc. IEEE Int. Symp. Circuits Syst. (ISCAS)*, Lisbon, Portugal, May 2015, pp. 541–544.

[33] B. J. Thijssen, E. A. M. Klumperink, P. Quinlan, and B. Nauta, "A 0.06–3.4-MHz 92-μW analog FIR channel selection filter with very sharp transition band for IoT receivers," *IEEE Solid-State Circuits Lett.*, vol. 2, no. 9, pp. 171–174, Sep. 2019.

[34] Y. Zhang, J. Zhu, and P. R. Kinget, "An out-of-band IM3 cancellation technique using a baseband auxiliary path in wideband LNTA-based receivers," *IEEE Trans. Microw. Theory Techn.*, vol. 66, no. 6, pp. 2580–2591, Jun. 2018.

[35] S. Jayasuriya, D. Yang, and A. Molnar, "A baseband technique for automated LO leakage suppression achieving <−80dBm in wideband passive mixer-first receivers," in *Proc. IEEE Custom Integr. Circuits Conf. (CICC)*, San Jose, CA, Sep. 2014, pp. 1–4.

[36] P. Song and H. Hashemi, "RF filter synthesis based on passively coupled N-path resonators," *IEEE J. Solid-State Circuits*, vol. 54, no. 9, pp. 2475–2486, Sep. 2019.

[37] Y.-C. Lien, E. A. M. Klumperink, B. Tenbroek, J. Strange, and B. Nauta, "Enhanced-selectivity high-linearity low-noise mixer-first receiver with complex pole pair due to capacitive positive feedback," *IEEE J. Solid-State Circuits*, vol. 53, no. 5, pp. 1348–1360, May 2018.

[38] S. Krishnamurthy and A. M. Niknejad, "Design and analysis of enhanced mixer-first receivers achieving 40-dB/decade RF selectivity," *IEEE J. Solid-State Circuits*, vol. 55, no. 5, pp. 1165–1176, May 2020.

[39] A. Agrawal and A. Natarajan, "An interferer-tolerant CMOS code-domain receiver based on N-path filters," *IEEE J. Solid-State Circuits*, vol. 53, no. 5, pp. 1387–1397, Aug. 2018.

[40] G. Han, T. Haque, M. Bajor, J. Wright, and P. R. Kinget, "A multi-branch receiver with modulated mixer clocks for concurrent dual-carrier reception and rapid compressive-sampling spectrum scanning," *IEEE J. Solid-State Circuits*, vol. 56, no. 1, pp. 235–253, Jan. 2021.

[41] S. Bu and S. Pamarti, "A 0.9V dual-channel filtering-by-aliasing receiver front-end achieving +35dBm IIP_3 and <−81dBm LO leakage supporting intra- and inter-band carrier aggregation," in *IEEE Int. Solid-State Circuits Conf. (ISSCC) Dig. Tech. Papers*, San Francisco, CA, Feb. 2021, pp. 94–95.

[42] ——, "A dual-channel high-linearity filtering-by-aliasing receiver front-end supporting carrier aggregation," *IEEE J. Solid-State Circuits*, in press.

[43] J. W. Park and B. Razavi, "Channel selection at RF using Miller bandpass filters," *IEEE J. Solid-State Circuits*, vol. 49, no. 12, pp. 3063–3078, Dec. 2014.

[44] Z. Lin, P.-I. Mak, and R. P. Martins, "Analysis and modeling of a gain-boosted N-path switched-capacitor bandpass filter," *IEEE Trans. Circuits Systems I, Reg. Papers*, vol. 61, no. 9, pp. 2560–2568, Sep. 2014.

[45] H. Darabi, A. Mirzaei, and M. Mikhemar, "Highly integrated and tunable RF front ends for reconfigurable multiband transceivers: A tutorial," *IEEE Trans. Circuits Syst. I, Reg. Papers*, vol. 58, no. 9, pp. 2038–2050, Sep. 2011.

[46] A. Borna, "Interference management techniques for multi-standard wireless receivers," Ph.D. dissertation, Depart. Elect. Eng. Comput. Sci., Univ. California, Berkeley, CA, 2014.

[47] Y. Xu and P. R. Kinget, "A chopping switched-capacitor RF receiver with integrated blocker detection," *IEEE J. Solid-State Circuits*, vol. 53, no. 6, pp. 1607–1617, Jun. 2018.

[48] Analog Devices, "Quad, 14-bit, 80 MSps/105 MSps/125 MSps serial LVDS 1.8 V analog-to-digital converter," AD9253 Datasheet, Rev. C, Jan. 2018. [Online]. Available: https://www.analog.com/en/products/ad9253.html.

[49] S. R. Velazquez, T. Q. Nguyen, and S. R. Broadstone, "Design of hybrid filter banks for analog/digital conversion," *IEEE Trans. Signal Process.*, vol. 46, no. 4, pp. 956–967, Apr. 1998.

[50] S. H. Zhao and S. C. Chan, "Design and multiplierless realization of digital synthesis filters for hybrid-filter-bank A/D converters," *IEEE Trans. Circuits Syst. I, Reg. Papers*, vol. 56, no. 10, pp. 2221–2233, Oct. 2009.

[51] Analog Devices, "10 MHz to 8000 MHz bypass amplifier," ADL8111 Datasheet, Rev. 0, Apr. 2019. [Online]. Available: https://www.analog.com/en/products/adl8111.html.